Chem Soc Rev

Structural and Dynamic Studies of Substrate Binding in Porous Metal-Organic Frameworks

Journal:	*Chemical Society Reviews*
Manuscript ID	CS-REV-08-2016-000603.R1
Article Type:	Review Article
Date Submitted by the Author:	10-Sep-2016
Complete List of Authors:	Schroder, Martin; University of Manchester, School of Chemistry Easun, Timothy; Cardiff University , School of Chemistry Moreau, Florian; University of Manchester, School of Chemistry Yan, Yong; University of Manchester, School of Chemistry Yang, Sihai; University of Manchester, Chemistry

Structural and Dynamic Studies of Substrate Binding in Porous Metal-Organic Frameworks

Timothy L. Easun,[1] Florian Moreau,[2] Yong Yan,[2] Sihai Yang[2] and Martin Schröder[2,3]

1. School of Chemistry, Cardiff University, Cardiff, CF10 3XQ (UK)

2. School of Chemistry, University of Manchester, Oxford Road, Manchester M19 3PL

3. Nikolaev Institute of Inorganic Chemistry, Siberian Branch of the Russian Academy of Sciences, 3 Ac. Lavrentiev Ave., Novosibirsk, 630090, Russian Federation

E-mail: Sihai.Yang@manchester.ac.uk; M.Schroder@manchester.ac.uk

Summary

Porous metal-organic frameworks (MOFs) are the subject of considerable research interest because of their high porosity and capability of specific binding to small molecules, thus underpinning a wide range of materials function such as gas adsorption, separation, drug delivery, catalysis, and sensing. MOFs, constructed by the designed assembly of metal ions and functional organic linkers, are an emerging class of porous materials with extended porous structures containing periodic binding sites. MOFs thus provide a new platform for the study of the chemistry and reactivity of small molecules in confined pores using advanced diffraction and spectroscopic techniques. In this review, we focus on recent progress in experimental investigations on the crystallographic, dynamic and kinetic aspects of substrate binding within porous MOFs. In particular, we focus on studies on host-guest interactions involving open metal sites or pendant functional groups in the pore as the primary binding sites for guest molecules.

Biographies

Timothy L. Easun: Timothy Easun was awarded his MSci from Nottingham University and PhD from Sheffield University. Dr Easun is currently a Royal Society University Research Fellow in the School of Chemistry at Cardiff University. His research focuses on the control of nanoscale flow of molecules within porous materials using photochemistry both as probe and actuator to make nanofluidic devices.

Florian Moreau: Florian Moreau obtained his MSc from the Université de Versailles-Saint Quentin en Yvelines, France (2008) and his PhD from the Université de Rennes 1, France (2011). He is currently a postdoctoral fellow at the University of Manchester with Professor Schröder where his current work is focused on the design and synthesis of highly connected, functionalised MOFs for gas storage applications.

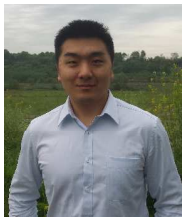

Yong Yan: Yong Yan, born in 1984, obtained his BSc from Lanzhou University in 2006 and PhD from University of Nottingham in 2011. He continued as a postdoctoral researcher with Professor Schröder focusing on structural characterisation of MOFs using various techniques such as synchrotron X-ray and neutron scattering techniques, as well as the discovery of new porous materials for various applications.

Sihai Yang: Sihai Yang received his BSc from Peking University in 2007 and PhD from University of Nottingham in 2011. He then joined as a senior research fellow/assistant professor in the School of Chemistry in University of Nottingham. He moved to University of Manchester as a Lecturer in 2015. His current research interests lie in the study of the "structure-function" relationships in porous materials.

Martin Schröder: Martin Schröder obtained his BSc from the University of Sheffield and PhD from Imperial College, London. He has held academic appointments at the University of Edinburgh and University of Nottingham. In 2015 he was appointed Vice-President and Dean of the Faculty of Engineering & Physical Sciences and Professor of Chemistry at the University of Manchester. His research lies in the area of coordination and supramolecular chemistry with specific focus on energy applications and clean technologies.

Contents

1. Introduction

Porous metal-organic frameworks (MOFs) are assembled from metal ions or clusters which are bridged by functional organic molecules. These materials often adopt three-dimensional extended microporous or mesoporous framework structures incorporating nano- and meso-sized pores, yielding large and accessible internal surface areas. Over the past decade, these hybrid materials have received considerable attention due to their potential for gas storage and separation, catalysis, optical properties, sensing, substrate recognition and drug delivery.[1,2] These important properties primarily rely on the selective recognition and binding of guest molecules by these functional materials.

Within the field of gas storage, separation and purification, there is particular emphasis on optimising the interactions between MOF hosts and the adsorbed substrate molecules, leading to the discovery of new functional materials with higher storage capacities and stronger binding energies. For this reason, visualisation of the guest-host binding interactions involved in the gas adsorption applications is crucial to the understanding of how these materials function, and to identify important potential mechanisms for the sensing and discrimination of guest molecules.

The experimental investigations reviewed herein are three-fold. (i) The determination of the locations of guest molecules within porous MOFs by static crystallographic studies, typically by *in situ* diffraction experiments as a function of gas loading, gives key insights into the preferred binding sites within pores. (ii) The direct observation of the dynamics of these adsorbed/trapped/captured guest molecules within the host together with the change of the molecular motion of the MOF materials, typically by spectroscopic experiments, reveals the nature of these binding interactions. (iii) Studies on the diffusion of guest molecules within the pores and channels of porous MOFs by pulsed field gradient (PFG) NMR or quasi-elastic neutron scattering (QENS) experiments can afford important knowledge on the kinetics of gas loading, and such information is fundamental to optimise gas adsorption processes in industry. Computational modelling, including density function theory (DFT) and molecular dynamics (MD), linked to experimental data has played an important role in visualising molecular motions and diffusion within pores. A combination of these static, dynamic and kinetic approaches offers a comprehensive understanding of the guest-host binding processes that ultimately govern these materials properties.

However, gaining such insight by experiment is highly challenging for a number of reasons. Firstly, MOF materials with excellent gas sorption properties usually crystallise with large unit cells and inevitably incorporate huge structural voids and framework disorder, resulting in weak, broad and/or heavily-overlapped diffraction peaks, thereby raising the complexity of structure solution and refinement. To overcome this, synchrotron X-ray radiation is often used instead of conventional in-house instrumentation, because diffraction patterns obtained from a synchrotron radiation source have much improved resolution and data quality.

Secondly, these materials and adsorbed gas molecules typically contain many light atoms (*e.g.*, H, D, Li, C, N, O) which have relatively small scattering lengths for X-rays and may be poorly located in X-ray diffraction experiments. Unlike X-ray experiments in which the scattering lengths are generally proportional to Z^2 of the elements (*i.e.*, heavy atoms with more electrons can scatter X-ray more effectively than light elements), neutrons interact with the nuclei of elements and the cross-section of each element is isotope-dependent and does not follow any particular rules. In general, light elements can have large cross-sections in terms of neutron scattering and therefore are more readily "seen" by neutrons (Table 1).[3] Thus, neutron diffraction offers unique possibilities for determining key features of both the structural details of MOF materials and the precise locations of gas molecules within the pore cavities. Indeed, neutron diffraction is the only experimental method that can observe D_2 (isotope of H_2) positions.

Thirdly, the nature of these host-guest interactions is often based upon weak supramolecular mechanisms (*e.g.,* hydrogen bonds, π···π interactions, van der Waals, electrostatic or dipole interactions). Such supramolecular interactions often involve hydrogen atoms and undergo dynamic processes. The dynamics of these interactions are difficult to probe directly by conventional spectroscopic experiments such as infrared (IR) or Raman spectroscopy, which are the most common methods for the study of molecular vibrations. Several examples of such studies are described in this review. Complementing optical spectroscopies, inelastic neutron scattering (INS) is a very powerful neutron spectroscopic technique to study atomic and molecular motions, including both the rotational and vibrational motions. In direct comparison to IR and Raman spectroscopy, INS has several major advantages:[3]

1. INS spectra are readily and accurately modelled. Measured INS intensities are related straightforwardly to the atomic displacement of the scattering atoms, which can often be obtained from simple classical dynamics. Any complications arising from electro-optical parameters are thus avoided. Indeed, the band

positions and intensities of most molecular systems can be accurately calculated using modern *ab initio* computational methods. This is especially valuable since these methods are a well-established part of the approach to understanding molecular structure and dynamics. Also, the manipulation of an INS spectrum, *e.g.,* subtracting a background, is straightforward.

2. INS spectra are sensitive to hydrogen atom vibrations.

The dipole (IR) and polarisability (Raman) changes required for vibrations to be observable by these techniques are dependent on electron density. IR and Raman techniques are generally, therefore, most sensitive to vibrations involving the heavier atoms because of their greater electron count. This is not the case for INS and the neutron incoherent scattering cross section of H is uniquely high, making it about ten times more visible than other atoms.

3. INS spectra are not subject to the rules of optical selection.

All vibrations are active in INS and, in principle, measureable. This stems from the mass of the neutron (ca 1 unified atomic mass unit). When scattered, a neutron transfers momentum to the atom, and INS measurements are not limited to observation at the Brillouin zone centre. The measured INS intensities are, *inter alia*, proportional to the concentration of the elements in the sample.

4. Neutrons are penetrating, while photons are not.

Neutrons penetrate deeply, of the order of millimetres, into typical samples and pass readily through the walls of containment vessels, generally aluminium or steel. INS results are thus naturally weighted to the measurement of bulk properties, rather than the gas adsorbed on MOF surfaces.

5. Wide spectral range.

INS spectrometers cover the whole molecular vibrational range of interest (16-4000 cm^{-1}). The lower energy range (below 400 cm^{-1}) is readily accessible, a region that is traditionally more difficult experimentally for infrared and Raman spectroscopies. With modern instrumentation, the quality of INS spectra approaches that of infrared and Raman spectra obtained from the same system under the same conditions.

These features make INS an ideal probe to study the MOF-gas binding dynamics, in particular for those involving hydrogen atoms. QENS, a sub-class of INS in which the energy transfer between the neutron and sample is very small (*i.e.* almost elastic collision), is another powerful neutron spectroscopic technique to study the slow motion and dynamics of gas-loaded MOFs owing to the large cross-section for light atoms,

especially for H. In particular, QENS has played an important role in probing the diffusion rate of the gas molecules along the pore structure of MOFs.

Recent studies on porous metal-organic frameworks (MOFs) for H_2 storage, selective carbon capture, and hydrocarbon separations have shown, in exceptional cases, location of guest molecules within the host *via* advanced crystallography studies (*i.e.,* both X-ray and neutron diffractions), providing invaluable structural rationale for their function and properties. Most of these successes have been achieved within host systems that display strong confinement effects on the guest molecules and/or have specific binding sites such as open metal centres. More recently the applications of INS and QENS to study gas-loaded MOFs have enabled the interrogation of the dynamics and kinetics of adsorbed gas molecules within porous MOFs, including the host-guest systems involving primarily soft supramolecular interactions. In this critical review we discuss recent progress using crystallographic, dynamic and kinetic studies on host-guest binding within a range of functional MOF materials, primarily for those containing open metal centres or pendant functional groups for specific guest binding within the pore.

Table 1. Neutron scattering cross sections of the elements typically used to construct MOFs.[3]

Element	$\sigma_{coherent}$(barn)	$\sigma_{incoherent}$(barn)	σ_{total}(barn)
H	1.7583	80.27	82.03
D	5.592	2.05	7.64
C	5.551	0.001	5.551
N	11.01	0.5	11.51
O	4.232	0.0008	4.232
Cl	11.5257	5.3	16.8
S	1.0186	0.007	1.026
P	3.307	0.005	3.312
Li	0.454	0.92	1.37
Mg	3.631	0.08	3.71
Al	1.495	0.0082	1.503
V	0.0184	5.08	5.1
Fe	11.22	0.4	11.62
Co	0.779	4.8	5.6
Ni	13.3	5.2	18.5
Cu	7.485	0.55	8.03
Zn	4.054	0.077	4.131
Zr	6.44	0.02	6.46
Ag	4.407	0.58	4.99
In	2.08	0.54	2.62
La	8.53	1.13	9.66
Ba	3.23	0.15	3.38
Bi	9.148	0.0084	9.156

$\sigma_{coherent}$: Bound coherent scattering cross section; $\sigma_{incoherent}$: Bound incoherent scattering cross section; σ_{total}: Total bound scattering cross section. 1 barn = 10^{-28} m^2.

2. Materials with open metal centres.

2.1 Cu(II)-based systems

Cu(II)-based MOFs, which show a high level of structural diversity and high porosity, have been intensively studied for energy storage (H_2 and CH_4),[4-7] separations of small molecules,[8] and heterogeneous catalysis.[9] Most importantly, the solvent molecules bound to the six-coordinated Cu(II) of the commonly observed Cu_2-paddlewheel motif (*vide infra*) can be removed in the activation process to generate coordinatively unsaturated Cu(II) sites, which play a significant role in the binding of guest molecules. One of the prototypical Cu(II)-based porous framework is $[Cu_3(BTC)_2]$ (H_3BTC = 1,3,5-benzenetricarboxylic acid),[10] a neutral framework composed of $[Cu_2(OOCR)_4]$ paddlewheels linked by BTC^{3-} units to form a cubic **tbo** type network. $[Cu_3(BTC)_2]$ has a trimodal pore structure containing three distinct cages: the largest cuboctahedron consisting of 12 $[Cu_2(OOCR)_4]$ paddlewheel units and 24 BTC^{3-} linkers with internal space of *ca*. 13 Å in diameter; the intermediate sized cage of diameter *ca*. 11 Å, comprising 8 BTC^{3-} units and 12 $[Cu_2(OOCR)_4]$ paddlewheels; and the smallest octahedron of *ca*. 5 Å in diameter formed from 4 BTC^{3-} units and 6 $[Cu_2(OOCR)_4]$ moieties.

In situ neutron powder diffraction (NPD) experiments on the D_2-loaded $[Cu_3(BTC)_2]$ at 25 K up to a saturated D_2 dosage of 6.5 D_2:Cu revealed a total of nine different D_2 adsorption sites.[11] The strongest binding sites were found at the coordinatively unsaturated Cu(II) sites with a Cu–D_2 (centroid) distance of 2.39(1) Å (Fig. 1). The adsorption of D_2 in this trimodal pore system follows a complex pore filling mechanism, with the D_2 site occupancies changing with dosage. This is attributed to the concentration-dependant optimal D_2 arrangements that result from the D_2–D_2 and framework–D_2 interactions. At lower loadings, the adsorption sites $D_2(2)$, $D_2(3)$, and $D_2(5)$ were found within the smallest cage, while $D_2(4)$ and $D_2(6)$ reside in the intermediate sized pore. At 5.5 D_2:Cu coverage, D_2 starts to populate the largest cage (Fig. 2). A dynamic rearrangement of the D_2 in the pores at loadings close to saturation reveals 4 D_2 molecules placed tetrahedrally within the smallest pore, 32 D_2 as a truncated octahedron in the intermediate sized cage, and 48 D_2 forming a rhombic dodecahedron in the largest pore.

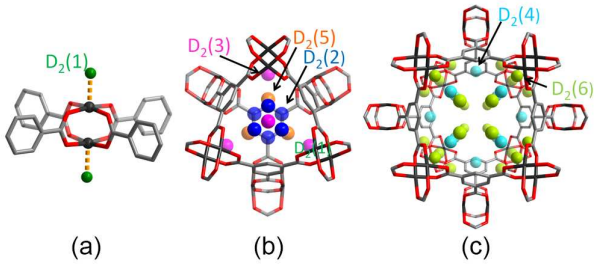

Figure 1. View of D_2 adsorption sites in $[Cu_3(BTC)_2]$: (a) the axial Cu(II) site; (b) view of the binding site within the 5 Å small pore with triangular windows, and (c) within the 11 Å pore with square windows (c). Reproduced from Ref 11.

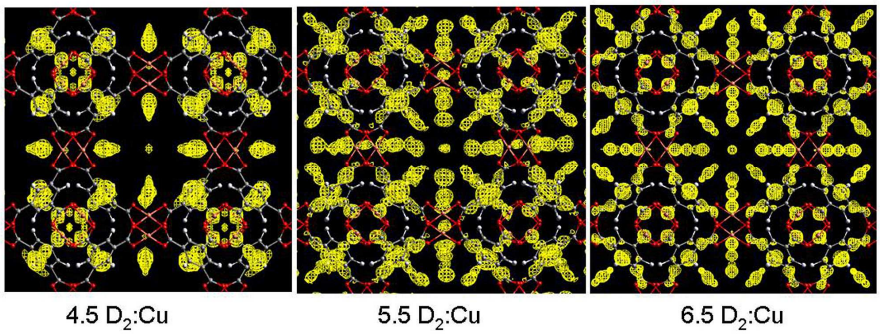

Figure 2. Fourier-difference maps shown along [001] for the unit cell featuring nuclear scattering density arising from D_2 (yellow) in $[Cu_3(BTC)_2]$ at a density of 0.7 fm $Å^{-3}$ from three different D_2 doses. Atomic colour scheme: Cu, metallic copper; O, red; C, grey; H, white. Reproduced from Ref 11.

An INS study of H_2 adsorbed in $[Cu_3(BTC)_2]$ has been carried out by Liu *et al.*[12] Three distinct spectral features from the INS spectra at H_2 loadings of less than 2.0 H_2:Cu were assigned to the same first three binding sites identified previously[11] (Figs. 3 and 4). These three binding sites are progressively populated at low coverage, consistent with the results obtained from the NPD study. It is widely accepted that MOFs incorporating ultra-micropores (below 10 Å) are optimal for H_2 binding due to enhanced overlapping potentials, consistent with the observed order of pore-filling. This has been further supported in a series of Cu(II)-tetracarboxylate MOFs in which lower H_2 uptake was observed with increasing pore size.[13-15]

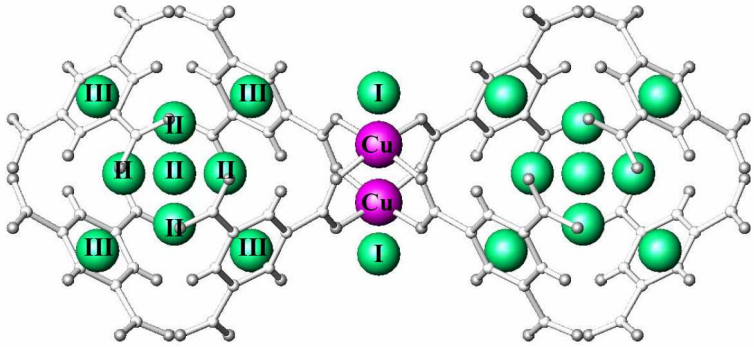

Figure 3. View of the first three H_2 adsorption sites in $[Cu_3(BTC)_2]$ labelled I, II, and III. Green spheres illustrate the positions of the adsorbed hydrogen sites. Cu(II) ions are indicated as pink balls. All other atoms and bonds are shown in pale grey. Reproduced from Ref 12.

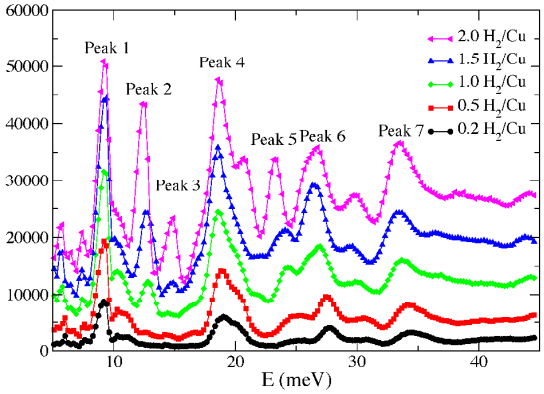

Figure 4. INS spectra of H_2-loaded $[Cu_3(BTC)_2]$ at 0.2, 0.5, 1.0, 1.5, 2.0 H_2:Cu. The background spectrum has been subtracted from the H_2 spectra. Reproduced from Ref 12.

A recent study on CH_4 storage in porous MOFs revealed that $[Cu_3(BTC)_2]$ shows record high volumetric CH_4 uptakes of 230 cc(STP) cc^{-1} at 35 bar and 270 cc(STP) cc^{-1} at 65 bar at room temperature.[16] A detailed structural analysis of $[Cu_3(BTC)_2]$ with various CD_4 loadings has been performed using NPD, and reveals four distinct CD_4 binding sites (Fig. 5).[17] The first two favoured adsorption sites are located on the open Cu(II) sites and in the centre of the triangular window formed by three $[Cu_2(OOCR)_4]$ paddlewheels and three BTC^{3-} units. The small window pocket shows an excellent complementarity with the geometry of a CH_4 molecule, thus creating an enhanced van der Waals binding interaction to CD_4. Two secondary adsorption sites are located at the centre of the smallest octahedral cage and in the corner of the intermediated sized cage.

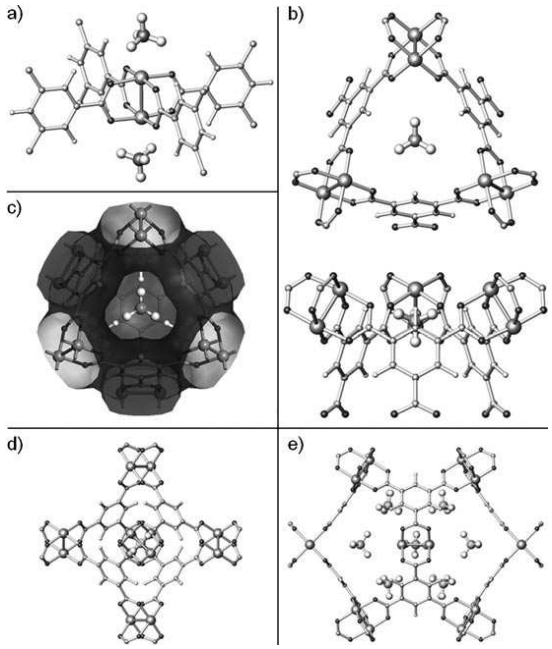

Figure 5. Experimentally determined crystal structure of $[Cu_3(BTC)_2]$ with CD_4 molecules adsorbed at (a) the open Cu sites and (b) the small cage window sites (top and side views). (c) Van der Waals surface of the small octahedral cage in $[Cu_3(BTC)_2]$ (derived by using N_2 as probe molecules) showing the size and geometry of the pore window in an excellent match with a CD_4 molecule. (d) CD_4 molecule adsorbed at the centre of the small octahedral cage, a secondary adsorption site. (e) CD_4 molecule located at the large cage corner site, also a weak adsorption site. Reproduced from Ref 17.

In addition to its excellent storage capacities for H_2 and CH_4, $[Cu_3(BTC)_2]$ shows very high acetylene storage capacity with an uptake of 201 $cm^3\,g^{-1}$ at 295 K and 1 atm. NPD studies on C_2D_2-loaded $[Cu_3(BTC)_2]$ reveals the significant contribution of open Cu(II) sites for acetylene binding (Fig. 6).[18] Structural refinement on the NPD data at 0.62 C_2D_2 per Cu loading in $[Cu_3(BTC)_2]$ indicates that C_2D_2 is adsorbed exclusively on the open Cu(II) sites with a distance between the Cu(II) ion and a C_2D_2 molecule of 2.62 Å. The C_2D_2 molecule lies parallel to the O–Cu–O axes with two half-occupied orientations. The second strongest C_2D_2 binding site was identified at a loading of 1.5 C_2D_2 per Cu, and resides at the entrance window of the smallest cage and reminiscent of the second binding site observed with CH_4 (above). First-principle total-energy calculations confirm the two preferential adsorption sites from the NPD results, and also suggests a slightly distorted geometry of the adsorbed C_2H_2 on Cu(II) sites. It was postulated that the

distorted C_2H_2 has an induced dipole moment which creates an enhanced Coulombic interaction between the C_2H_2 molecule and the open Cu(II) charge density.

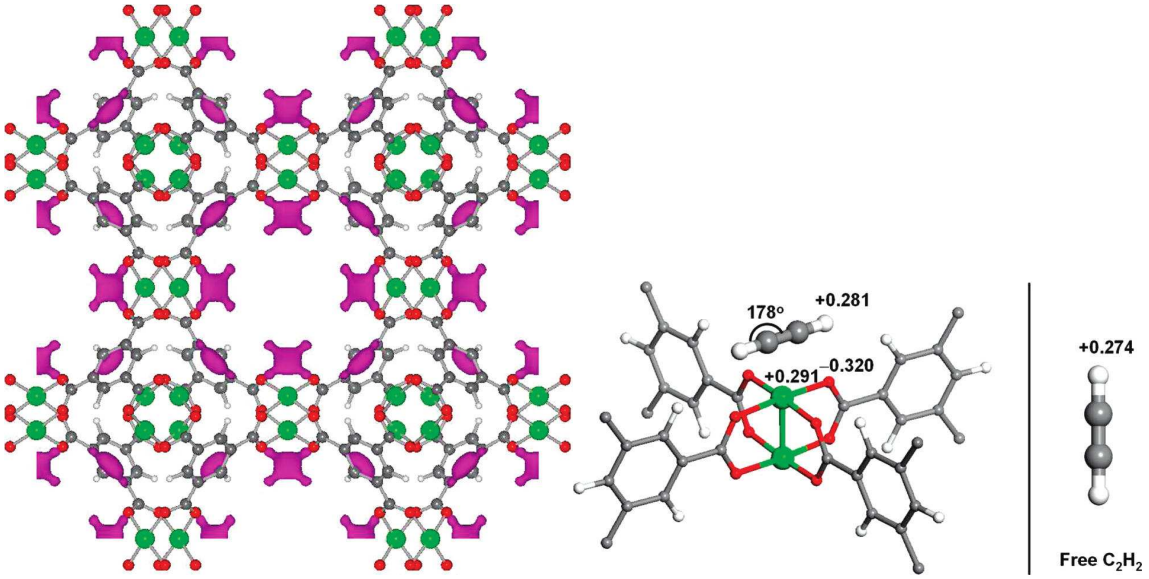

(a) (b)

Figure 6. (a) Positive difference Fourier map of 0.62 C_2D_2 per Cu loaded $[Cu_3(BTC)_2]$ calculated from NPD data. The pink regions indicate adsorbed C_2D_2 molecules bound to the first strongest adsorption sites at the open Cu(II) (Color scheme: Cu, green; O, red; C, dark grey. Atoms are not drawn to the scale). (b) Projected Löwdin charges of the C_2H_2 molecule adsorbed at the open Cu(II) sites in $[Cu_3(BTC)_2]$. The adsorbed C_2H_2 is slightly distorted with induced dipole moment, which enhances the electrostatic interaction with the open metal charges (left). For comparison, the Löwdin charge of the H atom in a free C_2H_2 gas molecule is also shown (right). Reproduced from Ref 18.

$[Cu_3(BTC)_2]$ has been investigated for its applications in the capture of the nuclear fission product I_2 gas, and the adsorption of I_2 vapour in the presence of moisture has been assessed.[19] A gas stream containing I_2 and water was used for the adsorption experiment as a model of the mixed gas streams in nuclear energy industrial processes. Synchrotron-based powder X-ray diffraction (PXRD) data on $[Cu_3(BTC)_2]$ loaded with different amounts of I_2 were collected. Due to the strong scattering nature of I_2, structural analysis clearly identified two significant I_2 adsorption sites in this porous host (Fig. 7). The wet gas stream results in binding of water to the apical sites of the Cu(II) paddlewheels such that the primary binding sites of I_2 were located within the smallest cage, close to the $[Cu_2(OOCR)_4]$ units, with an I···O interactions in the range of 3.23–3.30 Å. Another adsorption site was found in the intermediate sized pore with longer contacts between the I_2 and $[Cu_2(OOCR)_4]$ units and the BTC^{3-} rings (3.47–4.31 Å). The study identified an arrangement of adsorbed I_2

within the 11 Å pore that creates a hydrophobic-like barrier that inhibits further adsorption of water molecules inside the hydrophilic cavities in $[Cu_3(BTC)_2]$.

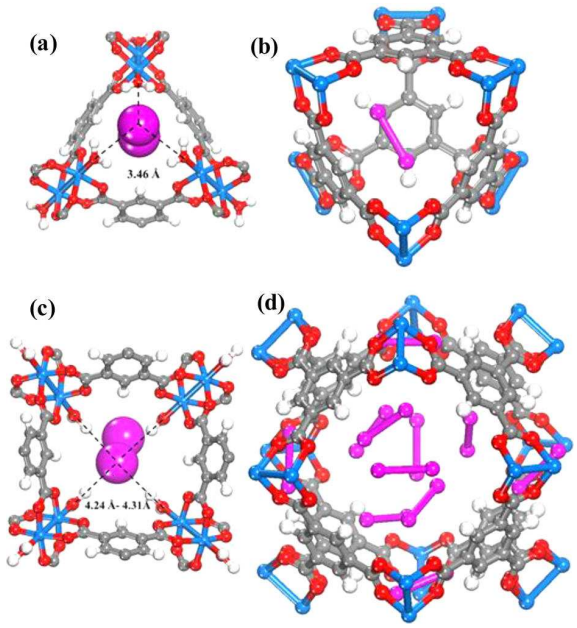

Figure 7. I_2 adsorption sites within $[Cu_3(BTC)_2]$ revealed by Rietveld refinement of the synchrotron PXRD of I_2-loaded samples. (a) I_2 residing in the triangular window; (b) one I_2 molecule within the smallest cage; (c) I_2 in the square window; (d) snapshot of the I_2 arrangement in the 11 Å cage. Atom colour scheme: fuchsia = I, blue = Cu, grey = C, red = O, and white = H. Reproduced from Ref 19.

The Cr(II) analogue, $[Cr_3(BTC)_2]$, is isostructural with $[Cu_3(BTC)_2]$, and its O_2 binding properties have been analysed.[20] $[Cr_3(BTC)_2]$ exhibits exceptional O_2/N_2 selectivity. Rietveld analysis of the NPD data of O_2-loaded $[Cr_3(BTC)_2]$ at a coverage of ~1.0 O_2/Cr revealed that the strongest O_2 binding sites are the open Cr(II) sites, with a short distance between Cr(II) and the centroid of O_2 of 1.97(5) Å (Fig. 8). The second O_2 adsorption site was sited at the triangular window of the smallest cage, an observed binding site of $[Cu_3(BTC)_2]$.

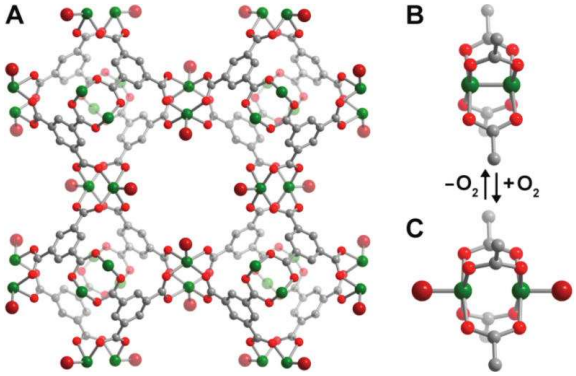

Figure 8. (a) View of structure of $[Cr_3(BTC)_2]$ with adsorbed O_2 at the open Cr(II) sites. Rietveld refinements of NPD data revealed that the Cr–Cr distance lengthens from 2.06(2) Å in the activated form (b) to 2.8 Å in (c) upon coordination of O_2. Colour scheme: Cr, green; O, red; C, grey. Reproduced from Ref 20.

A range of porous MOFs of Cu(II) with isophthalate linkers and investigated their H_2 adsorption properties.[4] Two isophthalate units can be linked linearly through a functionalised central core to generate a series of aromatic tetracarboxylate linkers with various functionalities, and these materials incorporating $[Cu_2(OOCR)_4]$ paddlewheels exhibit high H_2 storage capacities, up to an uptake of 77.8 mg g^{-1} at 77 K, 60 bar. NPD was used to determine the H_2 adsorption sites in MFM-101 (MFM = Manchester Framework Material, replacing the NOTT designation) and the structural refinement identified three distinct binding sites.[21] The first adsorption site was located at the axial position of the $[Cu_2(OOCR)_4]$ paddlewheel with a Cu–D_2 (centroid) distance of 2.50(3) Å, slightly longer than that observed in $[Cu_3(BTC)_2]$ (2.40 Å). This type of D_2–Cu interaction is not of the "Kubas" type σ-bond binding.[22] Two other adsorption sites were located at the middle of the triangular $[(Cu_2)_3(isophthalate)_3]$ window and in the cusp of three phenyl rings (sites II and III, Fig. 9), respectively, with both residing on the same 3-fold symmetry axis. Site occupancy analysis indicates that the open Cu(II) site does not show significantly higher binding affinity to D_2 than the other two identified sites.

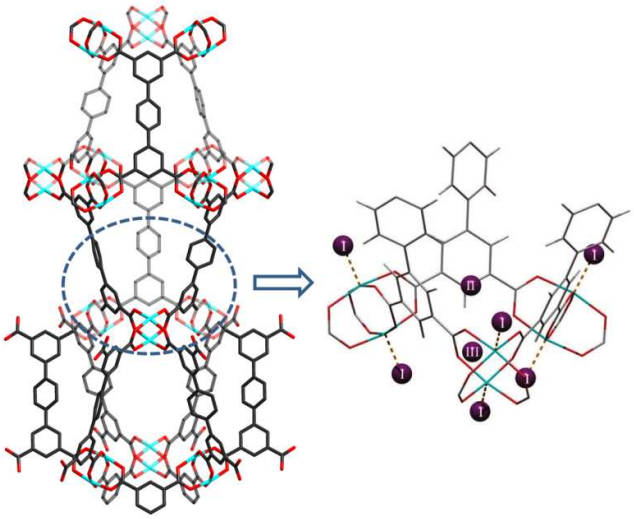

Figure 9. Structure of MFM-101 and the three identified D_2 adsorption sites in MFM-101 by NPD. Reproduced from Ref 21.

Tri-branched hexacarboxylate linkers with three isophthalate units connected through a central core in a coplanar fashion have been widely developed for the construction of highly porous (3,24)-connected networks.[23] These MOFs show exceptionally high porosity and gas sorption capacities. One archetype of this series is MFM-112, assembled from a C_3-symmetric aromatic hexacarboxylate linker and $[Cu_2(OOCR)_4]$ paddlewheels.[24] MFM-112 is constructed by three different cages: Cage A, a cuboctahedron containing of 24 isophthalate units and 12 $[Cu_2]$ paddlewheels; Cage B, a truncated tetrahedron comprising four hexagonal linker faces and four triangular windows; and Cage C, a truncated octahedron formed by eight linker faces and six square windows. MFM-112 shows simultaneously high H_2 adsorption at low and high pressures at 77 K: 23 mg g^{-1} at 1 bar and 111 mg g^{-1} at 77 bar. NPD studies revealed an interesting difference between the two Cu(II) ions of the same $[Cu_2(OOCR)_4]$ moiety in terms of their interaction with D_2 molecules.[15] The Cu(II) ions inside Cage A (CuA) show a higher binding energy towards D_2 molecules than the Cu(II) centres at the exterior of the cage (CuB) [CuA–D_2(centroid) 2.23(1) Å *vs* CuB–D_2(centroid) 2.41(1) Å] (Fig. 10). This study provides the first direct structural evidence demonstrating that a specific geometrical arrangement of open Cu(II) sites within the $[Cu_{24}(isophthalate)_{24}]$ cuboctahedral cage strengthens the interactions between D_2 molecules and the coordinatively unsaturated metal sites. Three other adsorption sites were identified at higher loadings, with two residing in the triangular opening and one located within Cage B close to the 3-fold axis of the window.

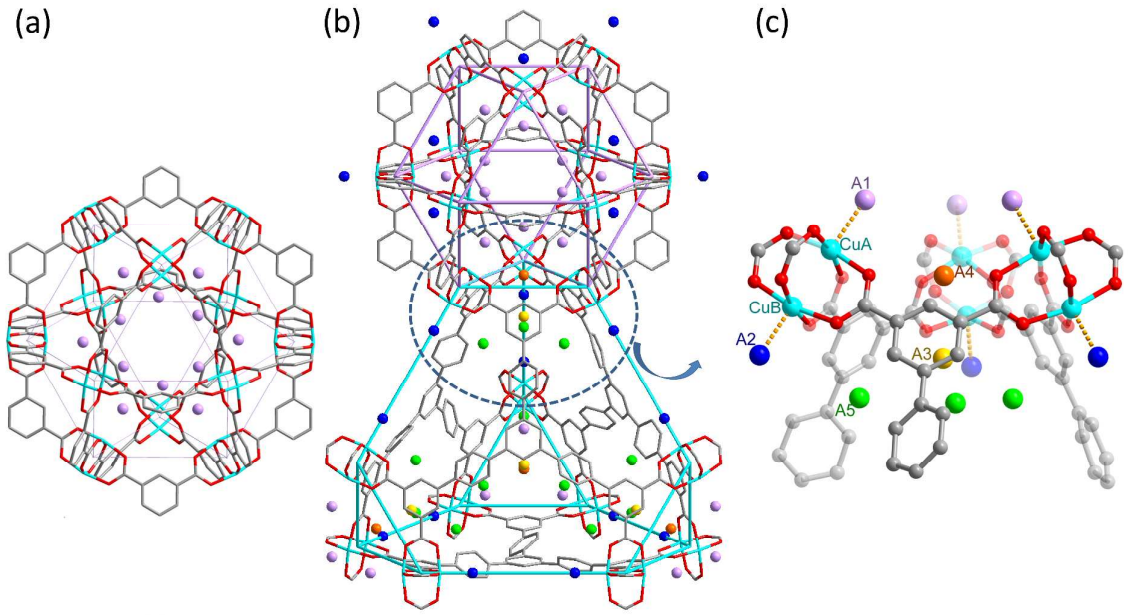

Figure 10. Views of D_2 positions in the desolvated framework MFM-112. (a) D_2 positions in the cuboctahedral cage at a loading of 0.5 D_2/Cu; (b) D_2 positions in cage A and cage B at a loading of 2.0 D_2/Cu; (c) view of five D_2 positions (A1, A2, A3, A4, and A5) at a loading of 2.0 D_2/Cu (grey, carbon; red, oxygen; turquoise, copper). The D_2 positions are represented by colored spheres: A1, lavender; A2, blue; A3, yellow; A4, orange; A5, green. Reproduced from Ref 15.

A tetrazolate linker has been used synthesize the robust sodalite-type framework $HCu[(Cu_4Cl)_3(BTT)_8]$•3.5HCl (Cu-BTT, BTT^{3-} = 1,3,5-benzenetristetrazolate).[25] The NPD study on the D_2-loaded sample demonstrated that D_2 molecules directly bind to unsaturated Cu(II) ions, revealing a Cu–D_2 (centroid) distance of 2.47 Å (Fig. 11). The observed Cu–D_2 distance is slightly elongated compared to the Mn–D_2 distance of [2.21 Å] and the Fe–D_2 distance [2.17(5) Å] found in the structural analogues Mn-BTT[26] and Fe-BTT,[27] respectively, probably due to the Jahn-Teller effect of the Cu(II) ions. Three additional D_2 binding sites were identified in Cu-BTT. Site II resides in the pocket of four tetrazolate units with distance of 3.46 Å from the framework Cl^- ion. Site III and IV, occupied at higher loadings, are located within van der Waals contact of two tetrazolate rings (site III) or benzene rings (site IV).

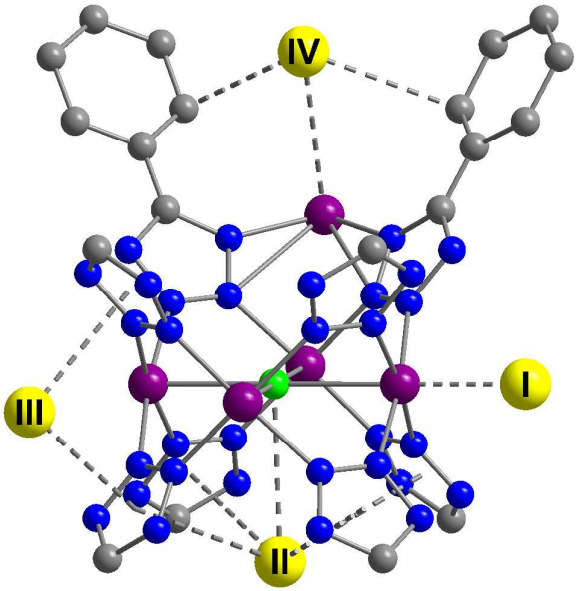

Figure 11. D_2 adsorption sites in Cu-BTT, as revealed by NPD. Purple, green, blue, and grey spheres represent Cu, Cl, N, and C atoms, respectively; Hydrogen atoms are omitted for clarity. Yellow spheres show the centroids of adsorbed D_2 molecules. Reproduced from Ref 25.

One of the small gas molecules that has attracted recent and growing attention is CO, a key chemical feedstock. One of the primary issues in utilising the massive quantities of CO produced as a bi-product of industrial processes, or as syngas, is the separation of CO from other gases (*e.g.* N_2, or H_2 in the syngas case). Long *et al*. have recently described further developments in this area in which they have demonstrated that the binding energy of CO with the open metal sites of MOF-74-M (M = Mg, Mn, Fe, Co, Ni, Zn) follows the Irving–Williams order of stability.[28] A further notable example of CO binding with promising separation capability in a dynamic MOF material is described in this section.

In 2014, Kitagawa *et al*. described a remarkable dynamic MOF, [Cu(aip)] (aip^{2-} = azidoisophthalate), that exhibits excellent separation of CO from N_2 by an unusual mechanism in which the interaction of CO with the framework causes a macroscopic structural change.[29] This comes about because the isolated $[Cu_2(OOCR)_4]$ paddlewheels within the as-synthesised material respond to removal of solvent by twisting to form infinite chains of paddlewheels coordinated axially *via* one of the carboxylate oxygens of the nearest paddlewheel, reducing the solvent-accessible volume from 38% to 25% of the unit cell. The adsorption of N_2 and CO by the desolvated material show markedly different behaviour: the N_2 uptake is unremarkable but the adsorption isotherm of CO shows both stepped and strongly hysteretic behaviour (Fig. 12).

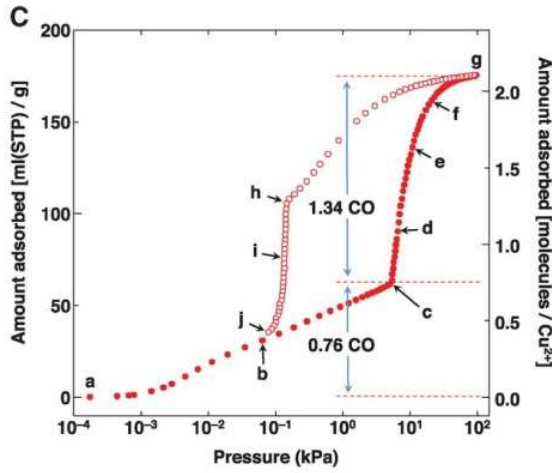

Figure 12. CO sorption isotherm in [Cu(aip)] at 120 K. Adsorption is shown in solid circles and desorption in open circles. Reproduced from Ref. 29.

In situ PXRD and IR studies demonstrated that above a threshold pressure of ~1 bar, the framework undergoes a significant phase change to a more open form that closely resembles the as-synthesised material, with CO bound to the axial positions of the $[Cu_2(OOCR)_4]$ paddlewheels, and located in the newly re-opened channels of the material (Fig. 13). This was confirmed by Rietveld refinement of the synchrotron PXRD data for the CO-loaded material. Notably, on testing CO and N_2 uptake from a range of mixtures of the two gases, it was concluded that even in the open form, N_2 is not efficiently absorbed. This was rationalised by the presence of three weakly coordinated CO molecules surrounding the channel that sterically block access to the N_2 molecules. This study, therefore, provides a detailed analysis and explanation at the molecular level of the observed highly selective adsorption of CO at 120 K.

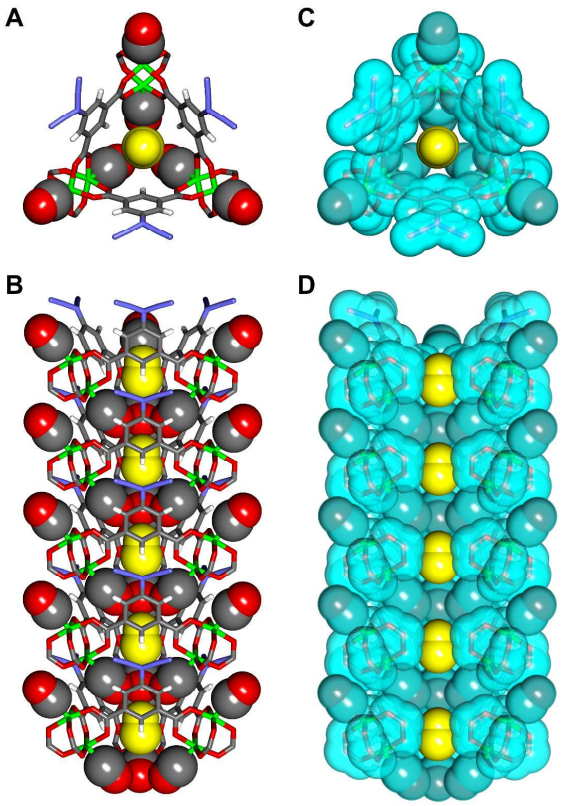

Figure 13. Single crystal X-ray structures of CO-loaded [Cu(aip)]. (a) Top and (b) side views of CO adsorbed within channel. (c) Top and (d) side views of CO-adsorbed channel with van der Waals surfaces depicted in light blue. Atoms are coloured as follows: Cu, green; C, grey; N, blue; O, red; H, white. Coordinated (grey and red) and non-coordinated (yellow) CO molecules are shown in a CPK model. In (d), part of the aryl moieties has been omitted for clarity. Reproduced from Ref. 29.

In addition to the numerous other Cu(II)-based MOFs, we note that a number of key studies on the location and dynamics of guest molecules have also been reported on Zn(II)-based MOFs, in some cases as analogues of Cu(II) frameworks (*e.g.,* with the BTC^{3-} linker).[30-32] The majority of these experiments have already been extensively reviewed in the literature.

2.2 The MOF-74/CPO-27, [M_2(dobdc)] (dobdc^{4-} = 2,5-dioxidobenzene-1,4-dicarboxylate) series

The MOF-74/CPO-27 series of MOFs having the stoichiometry [M_2(dobdc)] (M = Mg, Mn, Fe, Co, Ni, Cu, Zn; dobdc^{4-} = 2,5-dioxido-1,4-benzenedicarboxylate) were first reported in 2005 by Yaghi *et al*[33,34] (MOF-74-Zn) and by Fjellvåg *et al*[35,36] (CPO-27-Co and CPO-27-Ni) and have become one of the most extensively studied systems. The as-synthesised MOF comprises of $[M_2(C_8H_2O_6)(solv)_2]_\infty$ moieties that form a 3D

honeycomb structure containing 1D hexagonal pore channels bounded by dobdc^{4-} ligands which bridge M(II) ions (Fig. 14).[37] All the ligand oxygen atoms are involved in coordination to the M(II) centres and the resulting MO_5 units commonly have the sixth coordination site occupied by a solvent (water or DMF) molecule which points into the channels. The M–O bond *trans* to coordinated solvent is typically elongated, as is the M–O bond to the solvent, affording a distorted octahedral coordination geometry. One of the carboxylates coordinates via both oxygen atoms, while the other carboxylate bridges two metal atoms, as do the hydroxy oxygens. These M(II) octahedra are linked by alternating adjacent and opposite edge-sharing resulting in a helical arrangement of metal ions down the *c*-axis, parallel to the channels.

2.2.1. Structural studies of host–guest binding

These materials show high stability even in their desolvated forms upon removal of coordinated and uncoordinated solvent. The desolvated MOF contains *ca*. 60% of void space and a high density of vacant metal sites that are readily accessible for guest binding. The M–O bond which was *trans* to the solvent molecule typically shortens significantly on desolvation, and the M(II) retains a square-pyramidal coordination of ligand oxygen donors (Fig. 14).

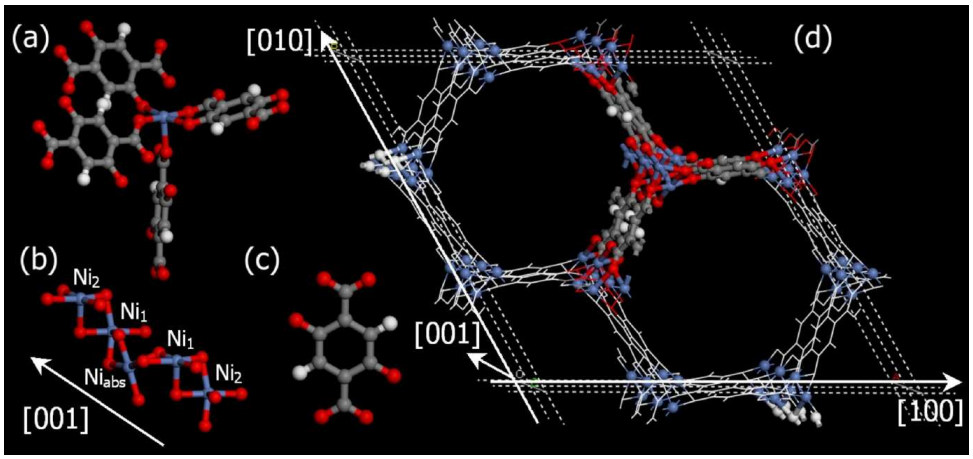

Figure 14. Views of the crystal structure of dehydrated MOF-74-Ni. (a) The coordination sphere at Ni(II) showing the square pyramidal structure; (b) chains of Ni(II) centres running along the *c* axis; (c) dobdc^{4-}; (d) the overall honeycomb structure. The C atoms are shown in grey, H in white, O in red, and Ni in blue. Reproduced from Ref 37.

A number of studies have investigated the binding of small molecules to the vacant metal sites in MOF-74 and a systematic review of techniques, molecules and approaches to this family of MOFs was

published by Valenzano *et al.* in 2012.[37] Since 2006, water and CO binding have been thoroughly investigated, but by far the most studied small molecules are H_2 and CO_2, particularly in the Mg, Ni and Zn-based materials. In recent years hydrocarbon binding has become an area of intense investigation, with reports of binding and/or separation experiments with all the MOF-74 series. Here we focus on the discussion on the most recent examples of guest binding in MOF-74 materials.

The binding of NO to MOF-74 was first described by Bordiga *et al.* in 2008.[38] In a study which employed structural (EXAFS, XRD), vibrational (IR, Raman) and electronic (UV/vis, XANES, emission) techniques they investigated the formation of the 1:1 adduct of NO with open metal sites in MOF-74-Ni. Adduct formation was found to cause a large perturbation of the vibrational and electronic properties of the framework compared to the dehydrated state, and the bound NO was slowly displaced by water, leading to a potential application for this material as an NO delivery agent in biological tissues.

The separation of O_2 and N_2 is a major industrial process that is currently undertaken using energy-intensive cryogenic distillation processes.[39] The use of zeolites which selectively adsorb N_2 over O_2 in medical devices is one approach, but this is limited by poor selectivity.[39] The use of MOF-74-Fe as an O_2 selective adsorbent was reported in 2011 and at 298 K the material has an O_2 capacity of 9.3 wt% corresponding to one oxygen molecule per two Fe(II) centres.[40] This capacity doubles at 211 K, with both Mössbauer and infrared spectra consistent with partial charge transfer from Fe(II) to O_2 at low temperatures. At room temperature the spectra show complete charge transfer to form Fe(III) and O_2^{2-}. This interpretation was confirmed by NPD data which revealed a symmetric side-on binding mode for O_2 at low temperature and a 'slipped' side-on binding mode in the room temperature structure. In contrast N_2 was found to adopt an end-on coordination mode to the M(II) cenre (Fig. 15). Experimentally, the selectivity factor for adsorption of O_2 over N_2 at 298 K was calculated to be 7.5 in MOF-74-Fe, but while this is among the highest reported for MOF materials,[41-47] the binding of O_2 at this temperature was irreversible and attempts to remove it *via* heating under vacuum resulted only in decomposition of the framework lattice. In contrast, reversible O_2 binding with retention of the framework structure was achieved at lower temperatures (201-226 K) and hence breakthrough O_2/N_2 measurements were simulated at 211 and 226 K, with the results suggesting that MOF-74-Fe could make an excellent O_2 selective adsorbent in a modified vacuum-swing adsorption process.

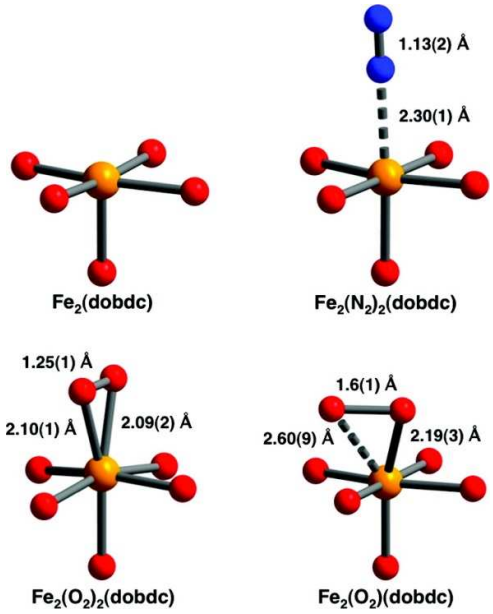

Figure 15. Views of the coordination spheres for the Fe(II) centres in MOF-74-Fe and the O_2- and N_2-adducts. Orange, blue, and red spheres represent Fe, N, and O atoms, respectively. The structures depicted are for samples under vacuum (upper left), dosed with N_2 at 100 K (upper right), dosed with O_2 at 100 K (lower left), and dosed with O_2 at 298 K (lower right). All diffraction data were collected below 10 K. Reproduced from Ref 40.

Binding of N_2O in MOFs have not been widely studied. The oxidation of Fe(II) in MOF-74-Fe to Fe(III) and or Fe(IV) species by N_2O has been reported, with the latter Fe(IV) complex catalysing oxygenation of ethane to ethanol.[48] At room temperature, MOF-74-Fe displays reversible adsorption of N_2O, and NPD on an N_2O-loaded sample reveals a mixture of 60% of η^1-O bound and 40% of η^1-N bound species, with Fe(II)-N_2O distances of 2.42(3) and 2.39(3) Å, respectively (Fig. 16). The oxidation process only occurs at higher temperatures, and passing a stream of N_2O through a fix-bed of MOF-74-Fe at 60 ^oC converts [Fe_2(dobdc)] to [$Fe_2(OH)_2$(dobdc)], with PXRD confirming the presence of a terminal hydroxide bound to Fe(III) in the latter species. Because this oxidation reaction employs a two-electron oxidant, it is likely that the an intermediate Fe(IV)-oxo species is produced; however, the Fe(IV) species could not be identified or isolated from the reaction. It is this Fe(IV)-oxo species that is believed to catalyse C-H activation and oxidizes ethane to ethanol (Fig. 16). Although the catalytic yield is too low (1%) for practical applications, the study demonstrates that the system is catalytic if competing substrates are excluded.

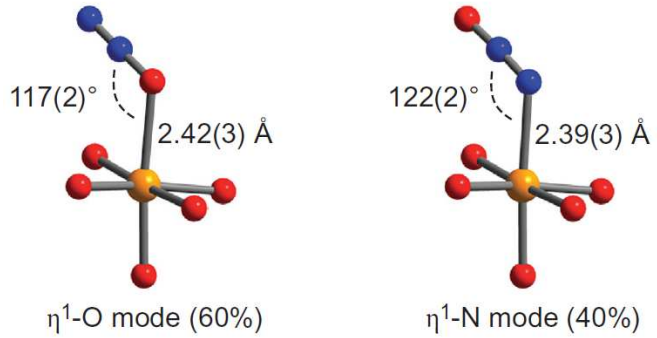

Figure 16. View of structures for N_2O bound to MOF-74-Fe obtained from NPD data collected at 10 K. Orange, grey, dark blue and red spheres represent Fe, C, N and O, respectively; H atoms are omitted for clarity. Reproduced from Ref. 48.

The binding and selective separation of hydrocarbons including ethane/ethylene/acetylene and propylene/propane is an area in which the use of MOFs has grown rapidly in the last few years[49-51] and a comprehensive review by Chen *et al* was published in 2012.[52] Reports of hydrocarbon binding and separations utilising MOF-74 include IR,[53,54] EXAFS,[53] computational,[37,49, 55-58] breakthrough[59-61] and NPD studies.[59, 60] The possibility of hydrocarbon separations in MOF-74 was proposed in 2011 in a study by Deng *et al*, in which they explored the feasibility of using MOF-74-Mg to separate ethane, ethylene, propane and propylene by measuring their individual adsorption equilibria and kinetics supported by simulations.[56] The binding of light hydrocarbons in MOF-74-Fe was addressed[59] by *in situ* NPD experiments in which desolvated MOF-74-Fe was dosed with the pure deuterated gas (*i.e.,* acetylene, ethylene, ethane, propane, and propylene) at 300 K and then cooled to 4 K for data collection. In all cases only one adsorption site was identified, at the open metal site of the material, shown for each hydrocarbon in Fig. 17. The study revealed binding between MOF-74-Fe and unsaturated hydrocarbons *via* the specific π-interactions which underpin the excellent separation between alkanes and alkenes, and the much poorer separation between alkynes and alkenes. Continuing research in this area has focussed primarily on (i) better understanding the binding dynamics of adsorbed hydrocarbons in MOF-74-M,[49,57,58,60] and (ii) undertaking practical breakthrough experiments to separate a range of hydrocarbon mixtures.[60, 61]

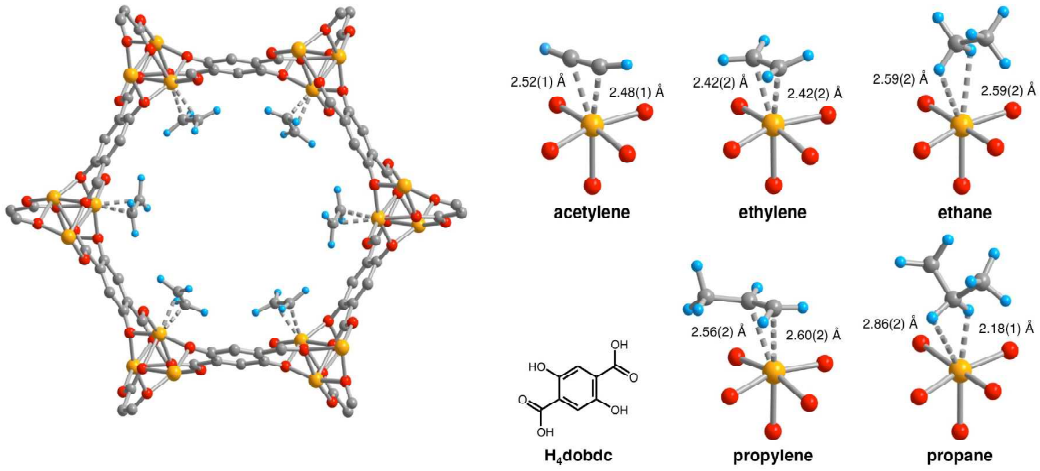

Figure 17. Left: A portion of the solid-state structure of MOF-74-Fe·$2C_2D_4$ as determined by NPD; orange, red, grey, and blue spheres represent Fe, O, C, and D atoms, respectively. Right: Views of H_4(dobdc) and the first coordination spheres for the Fe(II) centers in the solid-state structures obtained upon dosing MOF-74-Fe with acetylene, ethylene, ethane, propylene, and propane. Reproduced from Ref 59.

2.2.2. Dynamic studies of host–guest binding

The above examples have been primarily based on using static techniques (*e.g.*, PXRD, NPD) to understand or infer what are clearly dynamic processes in gas breakthrough experiments under flow conditions, often by trapping species at low temperatures. This approach has yielded results with small guest molecules described above, and has been widely applied to the studies discussed below on H_2, CO_2, CO, CH_4, H_2O and hydrocarbons, for which more detailed investigations of the structural dynamics of substrate binding have been reported.

2.2.2.1 Hydrogen

Several studies have investigated the vibrational properties of adsorbed H_2 in MOF-74 materials by IR spectroscopy.[62-67] The internal stretch modes of free *ortho*-H_2 (4155 cm^{-1}) and *para*-H_2 (4161 cm^{-1}) are IR inactive, but binding of H–H causes a perturbation that induces a dipole making them IR active. The magnitude of the shift of the IR stretch can be often correlated to the binding energy while the integrated area of the IR bands corresponds to the loading of H_2 within the framework.[63,68,69] However, Chabal *et al.* demonstrated that in MOFs containing fully saturated metal centres the H–H stretch is dominated by the

environment (ligands, metal, structure/geometry).[70] In 2010, their variable temperature IR (VTIR) spectroscopic and computational study examined MOF-74-M (M = Mg, Co, Ni, Zn) to probe the effect of the unsaturated metal site on the vibrational modes of H_2.[65] The IR spectra recorded at a low loading of H_2 (*i.e.* H_2 adsorbed at the metal site) appear to show a shift of ~30 cm^{-1} to lower energy over a wide temperature range (20 – 300 K), a finding which initially appears to disagree with previous studies that reported a shift of ~70 cm^{-1} on H_2 adsorption.[63, 64, 67] A shift of ~70 cm^{-1} to lower energy was observed by Chabal *et al*. but only on increasing the loading such that the second oxygen site was occupied. This behaviour was ascribed to H_2–H_2 'pairing' interaction between the occupied sites 1 and 2. This perspective was further supported in the observations of Ahn[71] and Rowsell[72] that there is an unusual behaviour in the binding energies of H_2 in MOF-74, as indicated by the H_2 isotherms measured at 77 K and low loading, which was tentatively assigned to H_2–H_2 interactions. Further studies of the IR spectra of MOF-74-Zn at 40 K at a range of H_2 loadings,[67] confirmed the first binding site to be the open metal centre, with an IR shift of ~70 cm^{-1}. Once the second binding site started to be occupied (at a loading of ~0.85 H_2 per Zn), another IR band with a shift of ~30 cm^{-1} began to appear, in line with the traditional assignment of these features. They observed a small but measureable shift (~2 cm^{-1}) of the initially formed bands on appearance of the second set of bands which they tentatively ascribed to an H_2–H_2 'pairing' interaction by comparison with the ~6 cm^{-1} red shift of the H_2 stretch in the free solid state.

However, strong evidence against the H_2 pair formation has been observed by INS experiments, which suggest the filling of MOF-74 with D_2 was sequential without the formation of pairs.[71] In 2011, Rowsell *et al*. published a comprehensive study in which they reported a series of VTIR experiments on MOF-74-M (M = Mg, Mn, Co, Ni, Zn) spanning the temperature range 35-298 K.[66] IR spectra were collected at loadings of 0.1 to 3.0 H_2 per metal and strongly red shifted IR bands corresponding to isolated H_2 molecules bound to the metal sites were observed, with a correlation between the isosteric heats of adsorption and the magnitude of the red shift. Further confirmation of the originally proposed stepwise filling mechanism observed by INS[71] was afforded by these VTIR experiments using HD and D_2. Subsequent VTIR work by Bordiga *et al*. on MOF-74-M (M = Mg, Mn, Co, Ni, Zn) has confirmed stepwise filling of H_2 and have elegantly demonstrated the ability of the VTIR technique to afford reliable energetic (ΔH^0) and entropic (ΔS^0) values which can be compared with isosteric heats of adsorption.[73] MOF-74-Ni has both the

highest adsorption enthalpy for H_2 binding (15 kJ mol^{-1}) across the series and correspondingly the highest perturbation of H_2 vibrational frequency.

A neutron scattering study of mixtures of D_2 and *para*-H_2 in MOF-74-Fe was used to directly investigate the possibility of pair formation.[74] The NPD study confirmed sequential site binding of D_2 (Fig. 18). The INS spectra of H_2-loaded MOF-74-M (M = Fe) at low loadings (<0.5 H_2 per metal) are entirely consistent with INS spectra recorded for MOF-74-M (M = Mg, Co, Ni and Zn),[71] but show the largest splitting of the $J = 1$ rotational state reported for this series. It was noted that there appears to be no correlation between the binding strength and the peak position in the INS spectra. This study further confirmed the absence of formation of strong H_2 pairs in this system.

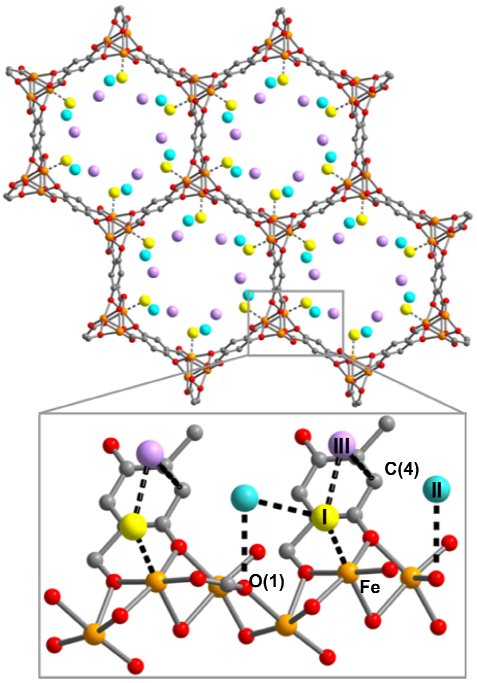

Figure 18. View of MOF-74-Fe loaded with 2.25 D_2 per Fe^{2+} along the [001] direction. Orange, grey, red spheres represent Fe, C, and O atoms, respectively. The box contains a close up view of the framework wall, showing closest D_2–D_2 and D_2–framework interactions (drawn as dotted lines) along the channel. Three D_2 sites, determined by NPD, are labelled as I, II, and III in order of binding strength. Reproduced from Ref 74.

Quasi-elastic neutron scattering (QENS) has been used to probe the diffusion of H_2 through MOF-74-Mg.[75] At a low loading of 0.3 H_2 per Mg, the QENS spectrum indicated no diffusion of H_2 on the

picosecond timescale. On increasing the H_2 loading, the spectrum progressively broadens. This broadening was fitted to three components corresponding to static H_2, H_2 diffusing along the pore surface *via* the adsorption sites, and bulk-like H_2 diffusion through the pores. The component of diffusion along the adsorption sites was indicative of liquid-like jump-diffusion without distinct directionality. The diffusion coefficient was of a similar magnitude to H_2 diffusing on a carbon surface but an order of magnitude lower than the one-dimensional diffusion of H_2 reported in MIL-53(Cr) and MIL-47(V) under similar conditions.[76]

A variation on the synthesis of MOF-74-M has been developed by employing the regioisomer 4,6-dioxido-1,3-benzenedicarboxylate (m-dobdc^{4-}) in place of the linker 2,4-dioxido-1,3-benzenedicarboxylate (dobdc^{4-}). A family of structural isomers of the MOF-74-M (M = Mg, Mn, Fe, Co and Ni) were prepared[77] and these are structurally analogous to MOF-74-M, sharing the same topology and high density of open metal sites, but with different local geometry that subtly alters the electronic properties of the binding sites. By using both X-ray and neutron diffraction techniques combined with INS and IR spectroscopic analyses, three binding sites were identified for H_2 within [Co_2(m-dobdc)] in a similar arrangement to that of MOF-74 (Fig. 19), but with slightly increased binding enthalpies by 0.4–1.5 kJ mol^{-1} in comparison to MOF-74-M.

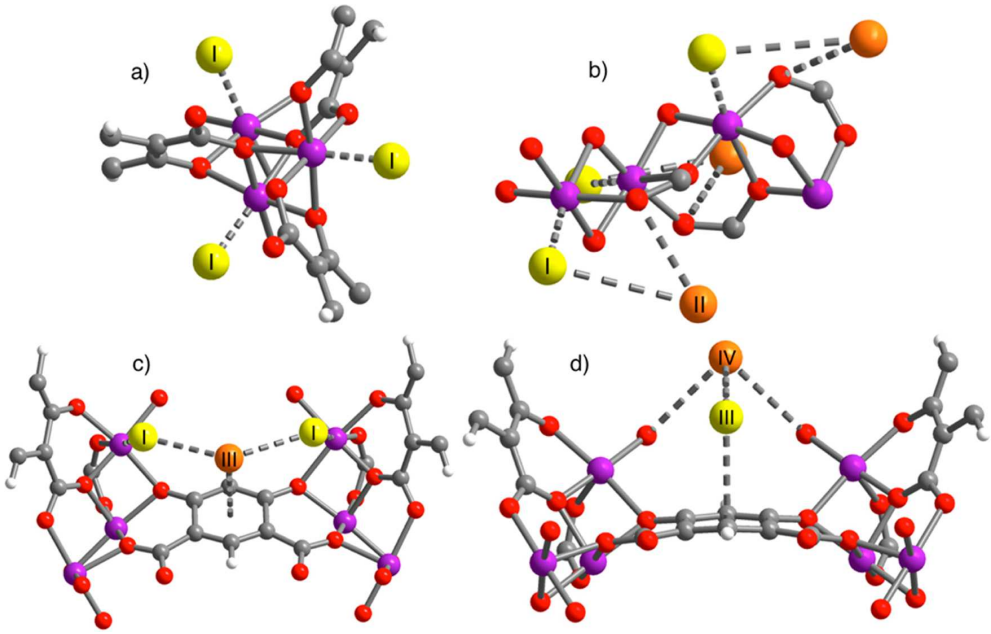

Figure 19. Views of crystal structures at 10 K of [Co_2(m-dobdc)] showing (a) the primary binding site (site I) on the open metal site; (b) binding site II interacting with D_2 at site I; (c) binding site III on the aromatic ring in the linker; and (d) binding site IV, interacting with the D_2 in site III. Purple, grey, red, and white spheres represent Co, C, O, and H atoms, respectively. Yellow and orange spheres represent D_2 molecules. Reproduced from Ref 77.

2.2.2.2 Carbon dioxide

The most extensively studied small gas adsorbed by MOF-74-M is CO_2, first reported by Yaghi *et al*. in 2005, comparing the CO_2 uptake of several MOFs at ambient temperature and up to 42 bar.[33] Of the MOF-74-M (M = Mg, Ni, Zn) series, MOF-74-Mg shows the highest CO_2 uptake (23.6 wt% at 0.1 atm, 35.2 wt% at 1 atm, both at 296 K). This was ascribed at the time to the increased ionic character of the Mg–O bond increasing the adsorption enthalpy at the first binding site.[78]

Since these first reports, studies exploiting vibrational spectroscopies[53,79-81] EXAFS,[79] *in silico* calculations,[49,79,81-86] neutron experiments,[82,87,88] NMR,[89-91] and gas adsorption[88, 92-100] have examined in depth the interaction of CO_2, CO, CH_4 and H_2O with the MOF-74 frameworks. These studies have ranged from fundamental binding interaction to dynamic gas separation experiments. Several significant reviews have subsequently covered the many adsorption studies, including the review by Valenzano *et al*. of small molecule binding to MOF-74 in 2011[37] and a review in 2012 by Long *et al*. specifically discussing CO_2 uptake in MOFs.[101] Therefore, this section details a limited number of selected examples of recent studies which specifically address the issues of guest binding dynamics.

Fig. 20 shows the calculated geometries of MOF-74-Mg adsorption complexes formed with CO, N_2 and CO_2, reported by Bordiga *et al*. in 2010.[81] CO and N_2 form nearly linear Mg(II)···CO and Mg(II)···N_2 complexes, respectively, but CO_2 binds at an angle with a Mg···O–CO angle of 129° and with a relatively short Mg–O distance (2.310 Å). This angular orientation is ascribed to a lateral electrostatic interaction between the CO_2 molecule and the carboxylate oxygen of the framework ligand, which also contributes to the marked increase in the adsorption enthalpy of CO_2 in the framework (-47 kJ mol^{-1}) compared with N_2 (-21 kJ mol^{-1}) or CO (-29 kJ mol^{-1}), calculated from VTIR measurements.

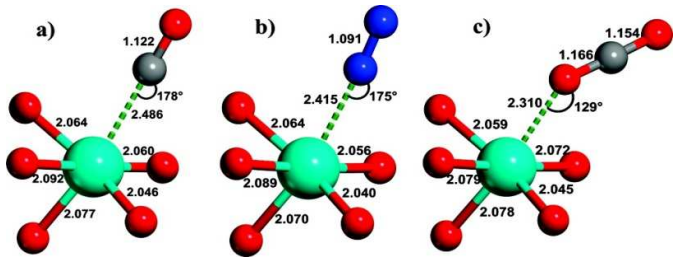

Figure 20. Views of the geometry of (a) CO, (b) N_2, and (c) CO_2 complexes of MOF-74-Mg; magnesium, oxygen, carbon, and nitrogen atoms are cyan, red, grey, and blue, respectively. These have been obtained by *ab initio* periodic DFT-D calculations. Distances in angstroms (±0.002) and angles in degrees (±1). Reproduced from Ref 81.

X-ray and neutron diffraction studies by Blom[102] and Yildirim[82] have confirmed surprisingly large distortions of the O-C-O bond angle from linear (180°) to 162° (in MOF-74-Ni) and 160.5° (in MOF-74-Mg), respectively. The latter study ascribed this phenomenon to the bound O-centre being essentially fixed in position with respect to the framework while the rest of the molecule has high orientational disorder leading to an apparent bond bending. The primary CO_2 to metal interaction was therefore still regarded as physisorptive.[82] In 2011, a second adsorption site for CO_2 in MOF-74-Mg was identified using variable temperature NPD measurements (Fig. 21).[87] This study also speculated that further filling of the MOF with CO_2 would occur *via* formation of a second layer within the pores. In both binding sites identified in this NPD study, a O–C–O bond angle of 170° was modelled from the 20 K data, less distorted than observed in previous studies.[82, 102]

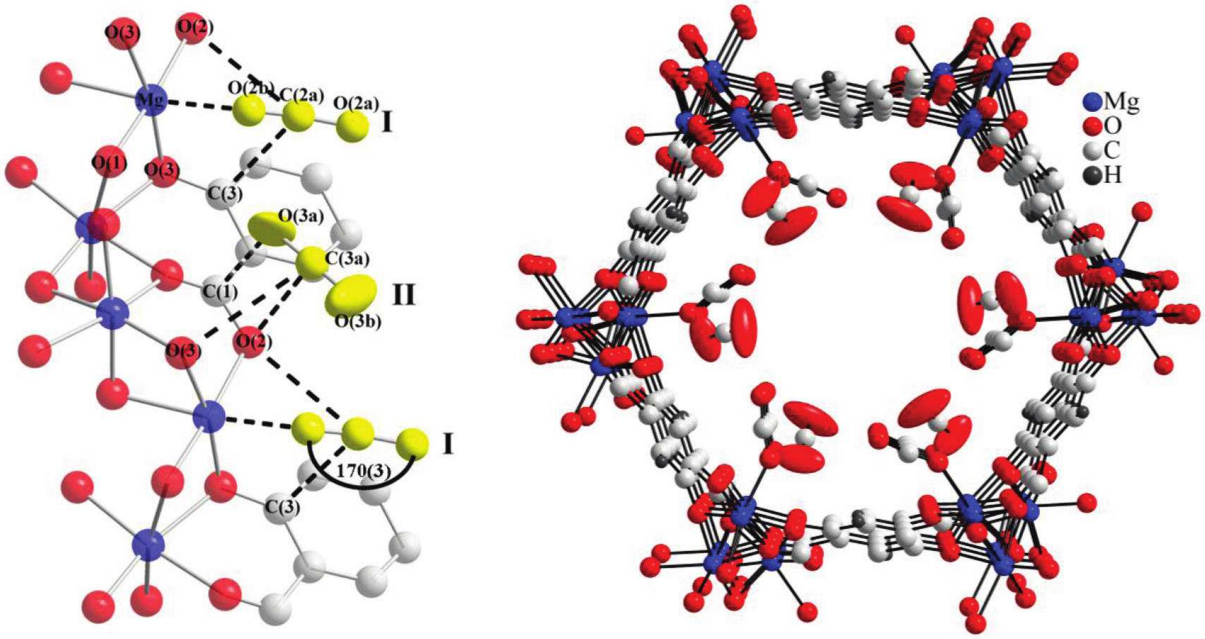

Figure 21. Partial structure of MOF-74-Mg loaded with 1.75 CO_2 (yellow) per Mg showing the nearest neighbor interactions found between the CO_2 sites (I and II) and the framework (left). The structure of MOF-74-Mg loaded with 1.75 CO_2 per Mg (viewed along the crystallographic c axis) showing two crystallographically distinct CO_2 adsorption

sites (right). The second CO_2 site was refined anisotropically with the thermal ellipsoids drawn at 50% probability. Reproduced from Ref 88.

The use of NMR spectroscopy to probe the dynamics, rotation and diffusion of CO_2 within MOF-74 has been illustrated *via* several studies.[90,91] For example, ^{13}C NMR line shape and spin-lattice relaxation were used to investigate the motional dynamics of adsorbed CO_2 in MOF-74-Mg.[91] Uniaxial rotation of ^{13}C-enriched CO_2 at the metal-bound site (Fig. 22) was invoked in order to model the variable temperature NMR spectra recorded between 12 and 400 K. The rotational axis was assumed to lie along the Mg–O(CO_2) vector, with the simulated CO_2 angle of rotation varying between 56° and 69° from this axis, in line with the observations derived from PXRD and NPD studies of a significant deviation of M–O–C angle from 180°. Significant slowing of molecular rotation was observed at temperatures below 150 K, with rotation essentially ceasing below 100 K. Interestingly, Arrhenius plots of the ^{13}C spin-lattice (T_1) relaxation data appear to show two different activation processes operating at different temperatures with the higher energy process dominating at higher temperatures. The onset temperature of the higher activation energy process for 0.3 CO_2/Mg (10.0 *vs* 4.0 kJmol^{-1}) coincides with the onset of gaseous CO_2 release (300 K), while that for 0.5 CO_2/Mg (6.0 *vs* 3.5 kJmol^{-1}) appears to correlate with an NMR line shape change attributed to the change from a single angle rotation of the CO_2 to a rotation with 'slight angle variations'. The lower activation energy for rotation in the higher loading experiment hints at a reduction in Mg(II)–CO_2 binding strength as loading increases.[91]

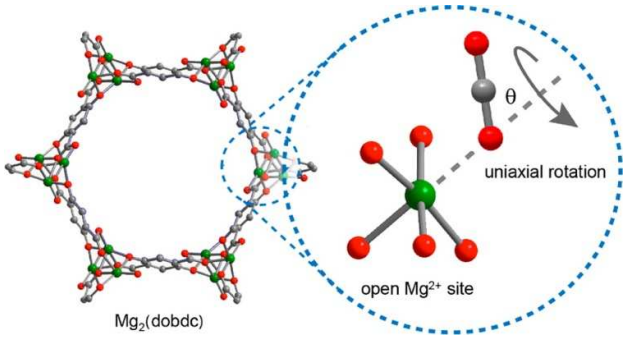

Figure 22. Schematic illustration of CO_2 uniaxial rotation at the open Mg(II) site in MOF-74-Mg. Grey, red, and green spheres represent C, O, and Mg atoms, respectively; H atoms are omitted for clarity. Note that the rotation axis is arbitrarily drawn in the picture. Reproduced from Ref 91.

A number of issues left unresolved by the above study[91] were subsequently addressed.[92] These problems include the lack of detail as to why two different activation processes should be occurring in CO_2-loaded MOF-74-Mg, along with the invocation of a symmetrical uniaxial rotation when the chemical environment is not perfectly symmetric. To address this, the free-energy landscape of CO_2 molecules in MOF-74-Mg was investigated from 100 K to 375 K using canonical Monte Carlo (MC) simulations,[104] at loadings of infinite dilution, 0.3 CO_2/Mg and 0.5 CO_2/Mg. In this MC simulation, two types of motion (i) a 'fluctuation' of the CO_2 molecule near the minimum energy bound configuration and (ii) a hopping motion of the CO_2 molecule between binding sites were identified (Fig. 23). Comparisons of the MC simulations and NMR data reveal that the former process dominates at lower temperatures (<150 K) and the latter at higher temperatures (>200 K). Importantly, the symmetry of the crystal environment means that the hopping motion of CO_2 molecules from site to adjacent site gives an identical NMR profile to that predicted by a uniaxial rotation of 80° about the Mg–O(CO_2) vector. Both the calculated and experimental equivalent rotational angles decrease with increasing temperature, an outcome of a thermally activated increase in site-to-site motion along the channels. This demonstrates the complexity of CO_2 diffusion dynamics with the hopping motion described herein corresponding well to the first diffusion mechanism proposed by Thonhauser *et al*.[83] for H_2, CO_2 and H_2O, as outlined in Fig. 23.

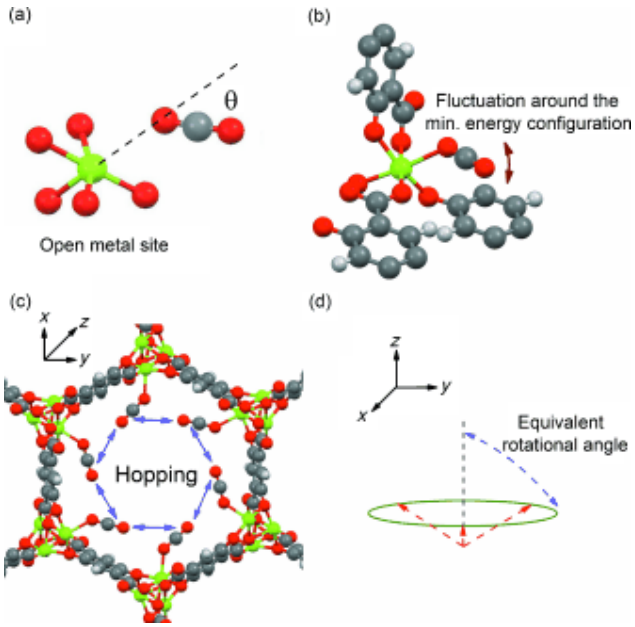

Figure 23. Schematic view of binding and dynamics of CO_2 in MOF-74-Mg. a) Orientation of CO_2 (C grey, O red) at the minimum-energy location near a metal site (Mg green); b) localized CO_2 fluctuation motion in which the oxygen atom of the CO_2 remains bound to the same metal site, and c) non-localised hopping motion. d) From an NMR point of view, the hopping of a CO_2 molecule between different metal sites in the *x*,*y* plane (see c) is equivalent to a rotation around an axis parallel to the *z*-axis with an angle referred as the "equivalent rotational angle". The CO_2 molecules (in c) are assumed to be located at their minimum-energy configuration, and are represented by the dashed red lines. Reproduced from Ref. 92.

There are many studies investigating the high selectivity of MOF-74 (and its derivatives) for CO_2 by examining mixed gas separation experiments.[86,93,94,97,99-102,105] Alkylamines have been bound to the metal centres of an extended MOF-74-Mg analogue to enhance selectivity for CO_2.[97] Flue gases from coal-fired power plants are typically released at ~1 bar at temperatures from 40 – 60 °C and contain a mixture of N_2 (70−75%), CO_2 (15−16%), H_2O (5−7%), and O_2 (3−4%).[106,107] Given the limitations of gas diffusion imposed by the relatively narrow channels of MOF-74-M (~11 Å) and the target to incorporate amine functionality,[108] the dobdc^{4-} linker was replaced by the longer dobpdc^{4-} (4,4′-dioxido-3,3′-biphenyldicarboxylate).[97] The overall topology of the subsequent MOF (Fig. 24) remains unchanged but the pores are considerably larger (~18.4 Å) than that of MOF-74. Subsequent functionalisation of the vacant metal site with N,N′-dimethylethylenediamine (mmen) affords [mmen-Mg_2(dobpdc)].[97]

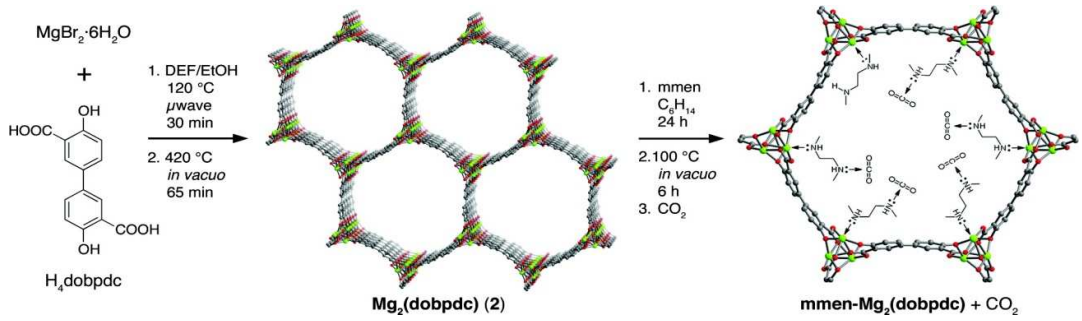

Figure 24. Synthesis of mmen-Mg_2(dobpdc) (mmen = *N*,*N*′-dimethylethylenediamine; dobpdc^{4-} = 4,4′-dioxido-3,3′-biphenyldicarboxylate). Microwave reaction of $MgBr_2 \cdot 6H_2O$ and H_4dobpdc (left) affords [Mg_2(dobpdc)] following evacuation of the as-synthesized solid at high temperatures (middle). The framework structure depicted is that obtained from single crystal X-ray analysis of the isostructural Zn(II) compound DEF-**1**. Green, red, and grey spheres represent

Mg, O, and C atoms respectively; H atoms are omitted for clarity. Addition of an excess of mmen to the activated framework yields [mmen-Mg_2(dobpdc)] (right). Reproduced from Ref 97.

Activated [mmen-Mg_2(dobpdc)] takes up 2.0 mmol g^{-1} (8.1 wt %) of CO_2 at 0.39 mbar and 25 °C and 3.14 mmol g^{-1} (12.1 wt %) at 0.15 bar and 40 °C, the latter being relevant to flue gas conditions. The purity of the CO_2 removed from simulated flue gases was estimated to be ~98% and the performance as an adsorbent under these conditions was comparable to amine-grafted silicas and aqueous amine solutions. Interestingly, the [mmen-Mg_2(dobpdc)] shows unusual stepwise adsorption of CO_2 at low pressure, and this step shifts to higher pressures at higher temperatures.[97] The mechanism of stepwise CO_2 adsorption in the isostructural and more crystalline Mn(II) analogue [mmen-Mn_2(dobpdc)] has been studied by combined spectroscopic and diffraction methods.[109] Diffraction data were collected at 100 K before and after exposure of a sample to 5 mbar of CO_2. Structural determination revealed that the mmen molecules were bound through one N-donor to the Mn(II) centre, Mn–N = 2.29(6) Å, with the other N-centre exposed on the surface of the wall of the pore (Fig. 25). On exposure to CO_2, CO_2 inserts into the M–N bond forming a carbamate with an O-centre bound to Mn(II), Mn-O = 2.10(2) Å (Fig. 25). The second O atom of the carbamate had a close interaction of 2.69(1) Å with the N-centre of a neighboring mmen, resulting in chains of ammonium carbamate running along the channel of the framework. This well-ordered chain structure was maintained at 295 K, as determined from a full Rietveld refinement against PXRD data collected at 295 K. Thus, the adsorption of CO_2 by [mmen-M_2(dobpdc)] at ambient temperatures is associated with a structural transition to form an extended chain structure held together by ion pairing between the metal-bound carbamate units and the outstretched ammonium group of a neighboring mmen molecule (Fig. 26). These studies demonstrated an excellent example of utilising the advanced diffraction technique to gain molecular understanding on the unusual properties in MOFs, in this case stepwise CO_2 adsorption.

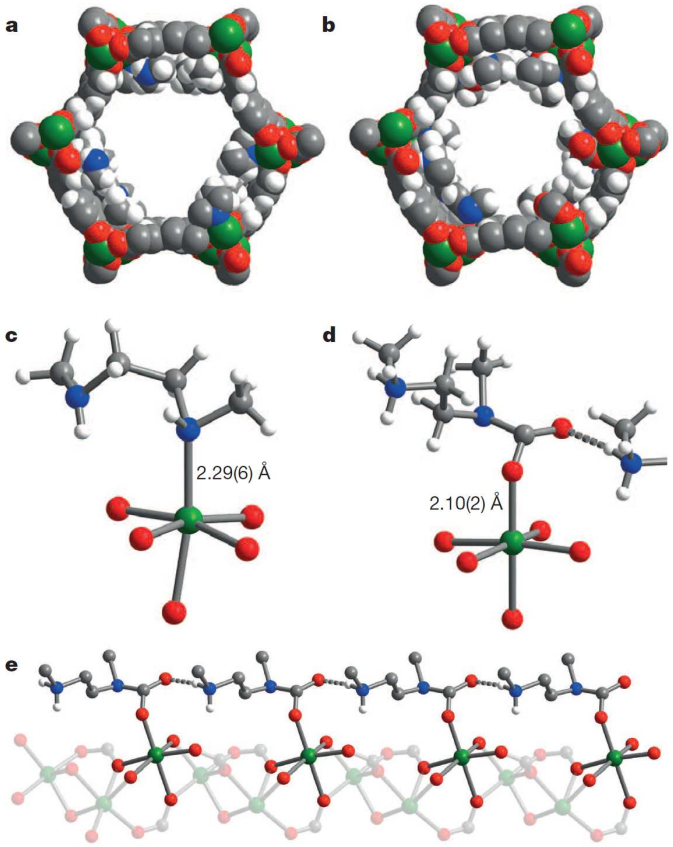

Figure 25. PXRD structures of [mmen-Mn_2(dobpdc)]. Space-filling models of the solid-state structures of (a) [mmen-Mn_2(dobpdc)] and (b) CO_2-loaded [mmen-Mn_2(dobpdc)] at 100 K. Portions of the crystal structures for [mmen-Mn_2(dobpdc)] (c) before and (d) after CO_2 adsorption. (e) A portion of the structure of CO_2-loaded [mmen-Mn_2(dobpdc)] showing the formation of an ammonium carbamate chain along the pore surface. Green, grey, red, blue and white spheres represent Mn, C, O, N and H atoms, respectively; some H atoms are omitted for clarity. Reproduced from Ref 109.

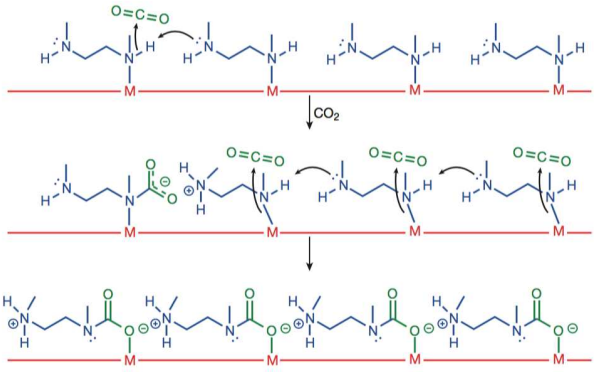

Figure 26. The proposed mechanism for CO_2 adsorption in [mmen-M_2(dobpdc)]. Reproduced from Ref 109.

3. Materials without open metal centres

3.1 The MIL-53 and MIL-47 series

The MIL-53 (MIL = Matériaux Institut Lavoisier) series of materials are built from chains of *trans* μ_2-OH corner-sharing octahedral M(III) centres (M = Cr, Al, Fe, Sc) $[MO_4(OH)_2]$ which are interconnected through ditopic terephthalate linkers, thus generating 1D lozenge-shaped pores.[110-113] The major characteristic of these materials is their ability to "breathe", *i.e.* to expand or contract drastically their crystalline structure adapting to the nature and amount of adsorbed guest molecules (Fig. 27).

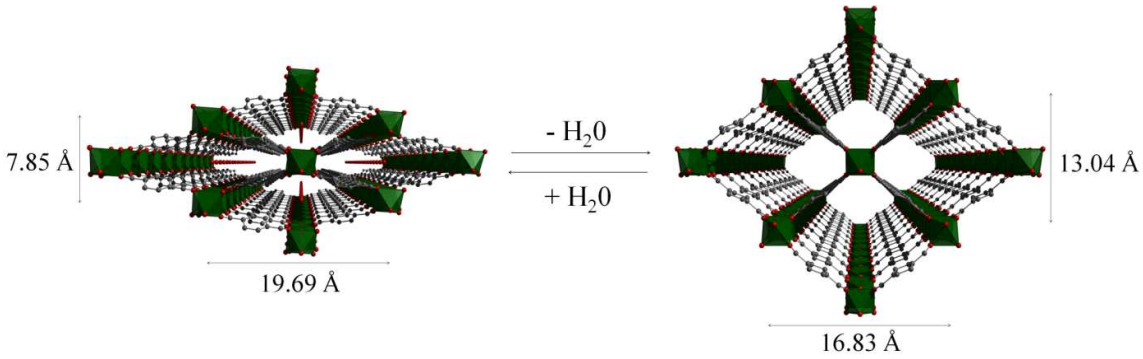

Figure 27. Views of the structure of MIL-53(Cr) upon dehydration and rehydration. Reproduced from Ref 112.

The structural flexibility of these MOFs in response to guest-host interactions has encouraged the investigation of adsorption mechanisms for various guests of interest by *in situ* characterisation techniques. Moreover, in the isostructural V(IV) material, MIL-47,[114] the μ_2-OH are replaced by μ_2-O groups and this MOF is much more rigid, which offers interesting opportunities for comparison. The adsorption isotherm of CO_2 in MIL-53(Cr) up to 30 bar at room temperature shows a two-step behaviour (Fig. 28a). After an initial rapid uptake of 3 mmol g^{-1} below 1 bar, a plateau is observed, and then a second uptake to 9 mmol g^{-1} occurs for pressures higher than 5 bar.[115] This unusual behaviour was studied by by means of high resolution *in situ* PXRD coupled with IR spectroscopy and DFT calculations.[116] It was confirmed that the two-step adsorption of CO_2 corresponds to a breathing phenomenon (Fig. 28b): starting from the activated open form MIL-53HT (HT = high temperature), the initial adsorption of CO_2 causes a shrinkage of the structure leading to a new low pressure (LP) MIL-53LP phase, the structure of which has been refined from PXRD data at 195 K under 1 bar of CO_2. In MIL-53LP, the CO_2 molecules could be located and their occupancy refined to 0.54, in good agreement with the amount of CO_2 adsorbed at the first plateau. The adsorbed CO_2 molecules were found to

interact with two μ_2-OH groups from the two closest opposite chains of the pores (Fig. 29) and are aligned along the pore direction with intermolecular distances of 3.4 Å, indicating CO_2–CO_2 interactions. With increasing pressures of CO_2, the second gas uptake corresponds to a full opening of the structure, leading to the MIL-53HP (HP = High Pressure) phase in which the gas molecules are disordered.

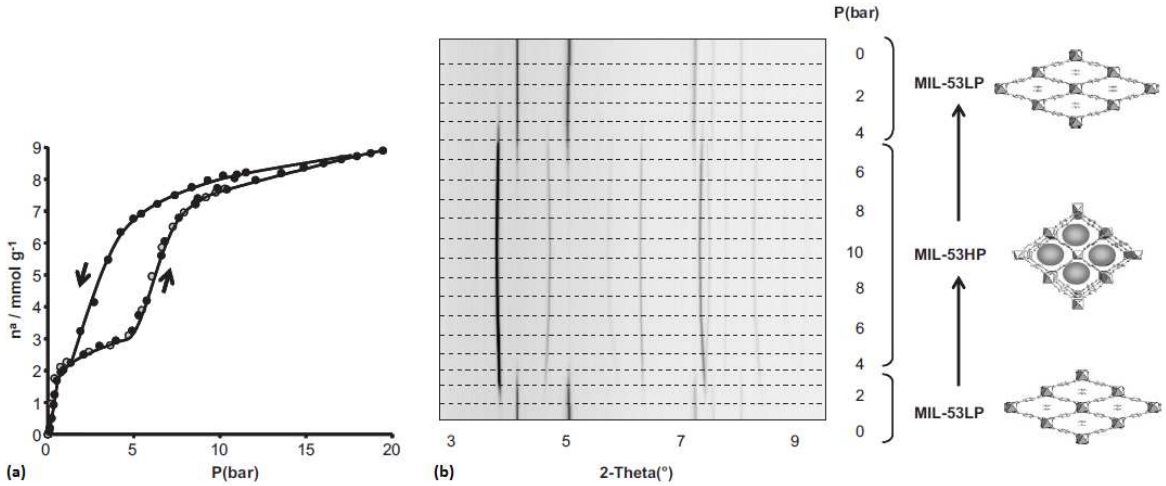

Figure 28. (a) Adsorption–desorption isotherms of MIL-53(Cr) at 304 K; (b) PXRD patterns of MIL-53(Cr) under various pressures of CO_2 at 293 K. Reproduced from Ref 116.

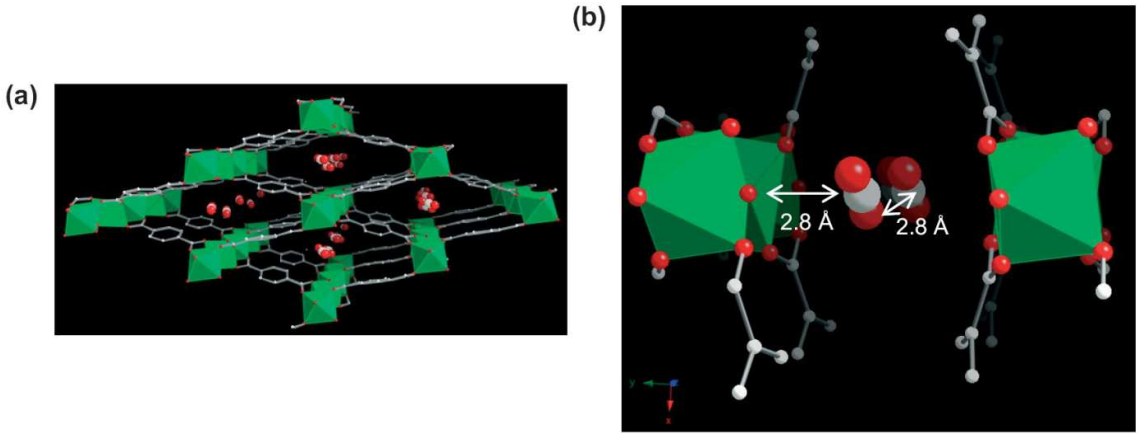

Figure 29. (a) View of the refined structure of MIL-53LP along the c-axis (P_{CO2} = 1 bar , T = 195 K); (b) closer view of the local interactions between the CO_2 molecules within a channel of MIL-53 (P_{CO2} = 1 bar, T = 195 K). Reproduced from Ref 116.

Diffusion of CO_2 molecules and their interactions with the MIL-53(Cr) framework during adsorption have been investigated by a combination of QENS and MD.[117] At low CO_2 loadings, in the closed MIL-53LP phase, the minimum free energy regions calculated for the MOF correspond to the OH groups of the octahedra chains. This explains the slow diffusion of CO_2 because of its strong interaction with the hydroxy groups and is consistent with the *in situ* PXRD study. It was demonstrated that with increasing pressures, the transport diffusivity of CO_2 is two orders of magnitude faster in the HP form than in the LP form, but surprisingly, the diffusion mechanism remains strictly one dimensional, suggesting that the CO_2 molecules, which still interact strongly with OH groups, restrict the motions of additional adsorbates perpendicularly to the channels. Interestingly, a similar study has been reported by Salles *et al.* on the diffusion of CO_2 in the rigid MIL-47 system.[118] Although the authors could not elucidate unambiguously the microscopic diffusion mechanism of CO_2 from the QENS experiment in this case, their analysis of the MD trajectories suggests a 3D mechanism for CO_2 diffusion in MIL-47. This difference has been attributed to the absence of the hydroxy groups as preferential adsorption sites in the pores of MIL-47 in contrast with the case of MIL-53(Cr).

In both MIL-53(Cr) and MIL-47, adsorption of CH_4 occurs in a single step without framework breathing.[115] A dynamic QENS/MD study on the diffusion of CH_4 in these materials reveals a 1D diffusion mechanism of the adsorbate in the fully open pores in both cases.[119] The significantly higher diffusivity of CH_4 in MIL-47 than in MIL-53(Cr) and the higher activation energy for the latter are again related to the μ_2-OH groups which act as attractive sites and steric barriers. In both systems, the diffusivity of adsorbates is higher for CH_4 than for CO_2, consistent with higher activation energies calculated for CO_2.

Recently, QENS/MD studies of the diffusion of CO_2/CH_4 mixtures in the MIL-53(Cr) and MIL-47 have sought to evaluate the impact of the CO_2 concentration on the diffusivity of CH_4.[120] In both cases, the diffusivity for CH_4 was found to decrease with increasing CO_2 loading, although CO_2 has little to no influence on the diffusivity for CH_4 as a function of the total gas loading. MD trajectories of the gases show that in both materials, CO_2 and CH_4 follow a 1D type diffusion mechanism. CH_4 is distributed in the central zone of the pore while CO_2 molecules mainly diffuse in the vicinity of the polar μ_2-OH groups for MIL-53(Cr) and close to the pore wall for MIL-47.

A similar methodology has been used to describe the dynamic properties of H_2 in MIL-53(Cr) and MIL-47 at 77 K.[76] In the case of H_2, no framework breathing phenomenon was observed and the pores stay

fully open throughout the experiment. QENS experiments linked to MD simulations fitted a 1D diffusion mechanism in the case of MIL-53(Cr), revealing that the μ_2-OH group act as steric barriers rather than specific binding sites governing the diffusion process. A 3D model was established for H_2-loading in MIL-47 since there is no specific steric barrier for adsorbed H_2 molecules (Fig. 30). The most striking phenomenon is the supermobility of adsorbed H_2 in both materials as evidenced by a sudden increase of the diffusivity at low loadings, not previously observed in nanoporous materials.

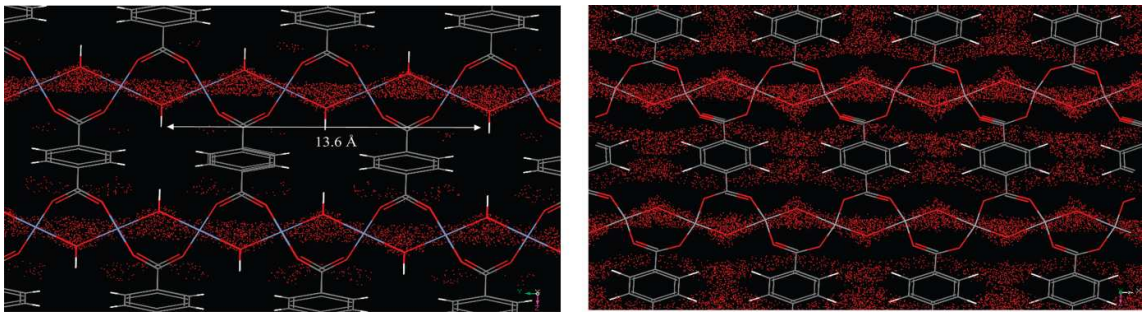

Figure 30. Views of the microscopic diffusion mechanism of H_2 from the 2D probability density plot in MIL-53-Cr (left) and MIL-47(V) (right). Reproduced from Ref 76.

In situ NPD was used to characterise the H_2 adsorption sites in MIL-53(Cr) at 10 K at various loadings.[121] With increasing pressures, four different adsorption sites are sequentially occupied (Fig. 31), the first site D1 being located in the acute corner of the lozenge-shaped pore (Fig. 32). This site is closer to the C-C bond of the carboxylates (3.3 Å) and to the H from the opposite benzene ring (2.5 Å) than to the O from the μ_2-OH group (4.3 Å), further confirming their steric role of the latter in the adsorption mechanism. The second and third adsorption sites are found in the obtuse corner of the pore, and the only specific interactions are with the carboxylate functions for D2 and with benzene rings of the ligands for D3. The D4 site, closer to the centre of the pore, only involves interactions between adsorbate molecules. The adsorption mechanism of H_2 in MIL-53(Cr) is thus governed by the steric effects of binding guest species to the μ_2-OH groups that determine the position of the initial and hence subsequent binding sites, leading to a 1D diffusion pathway for the guest molecules.

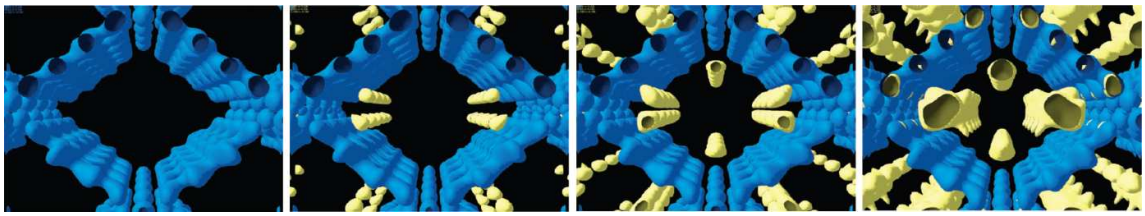

Figure 31. Fourier maps obtained from the neutron diffraction data. From left to right : the empty MIL-53(Cr) and three subsequent loadings with D_2 (0.4, 1.4, 3.2 D_2 equivalent wt%). Reproduced from Ref 121.

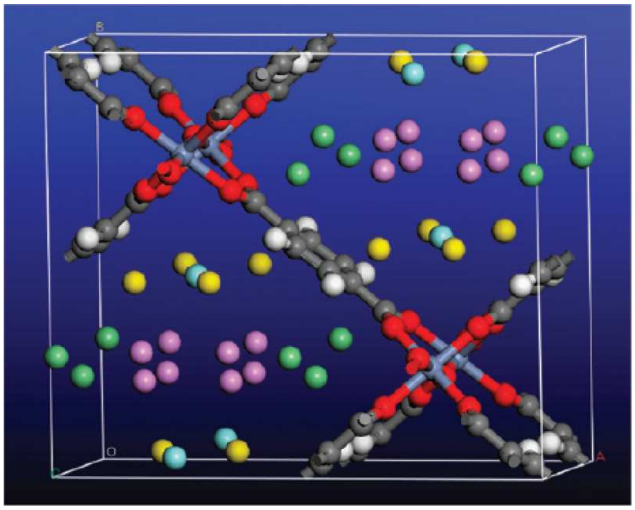

Figure 32. View of the refined structure of D_2 loaded MIL-53(Cr) in saturation conditions showing the positions of the adsorption sites D1 (green), D2 (blue), D3 (yellow) and D4 (purple). Reproduced from Ref 121.

3.2 MOF-5, $[Zn_4O(BDC)_3]$ (BDC^{2-} = benzene-1,4-dicarboxylate)

$[Zn_4O(BDC)_3]$ (BDC^{2-} = 1,4-benzenedicarboxylate; terephthlate), known also as MOF-5, is constituted of octahedral $\{Zn_4O\}$ clusters linked through linear dicarboxylate linkers.[122] The $[Zn_4O(O_2CR_2)_6]$ cluster is a tetramer of ZnO_4 tetrahedra sharing a central μ_4-O corner and connected through six bidentate carboxylates from the ligands. An initial attempt to determine the adsorption sites of H_2 molecules was reported by Rosi *et al.* by INS experiments at 10 K for various loadings.[30] Two binding sites were assigned: to the Zn(II) cluster and to the benzene ring of the ligand. The first primary adsorption site was assigned[32,123] to a position equi-distant to three carboxylates from the cluster above a face of the inorganic cluster, and the second adsorption site to an edge of the cluster, followed by sites around the organic linker. These assignments resulted from

analysis of INS experiments for a series of MOFs built around from the same $[Zn_4O(O_2CR)_6]$ clusters and different organic linkers, as well as results from *in situ* X-ray diffraction studies of Ar- and N_2-loaded single crystals of MOF-5.[32, 123]

Single crystal neutron diffraction was also used to determine the adsorption sites for H_2 in MOF-5.[124] The diffraction experiment was carried out on a single crystal which had been loaded at room temperature with H_2 gas at a pressure of 1 atm. Two primary adsorption sites were located from the neutron diffraction data collected at 5 K (Fig. 33). The first fully occupied site (α-site) is situated at 3.61(5) Å from a Zn(II) centre, 3.75(6) Å from the μ_4-O atom, above an empty face of the $[Zn_4O(O_2CR)_6]$ cluster, which is agreement to the above INS study. The second site (β-site) was found above an external face of a ZnO_4 tetrahedra, equi-distant [3.45(5) Å] from O-centre in carboxylate functions with a Zn...H distance of 3.64(6) Å, which differs slightly from the previous conclusion from the INS study.

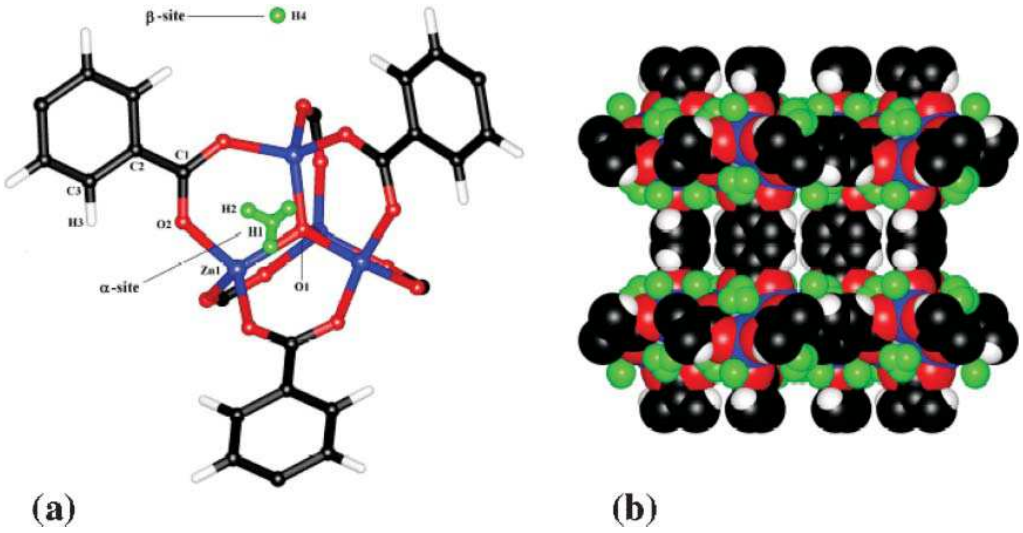

Figure 33. (a) The location of the adsorption sites for H_2 at 5 K relative to the framework atoms. The α-site is 100% occupied at 50 K, 30 K and 5 K. The β-site is 98% occupied at 5 K; (b) space-filling diagram of one of the framework cavities at 5 K. Reproduced from Ref. 124.

3.3 Zeolitic Imidazolate Framework ZIF-8

Zeolitic imidazolate frameworks (ZIFs) are porous materials assembled by tetrahedrally M(II) (M = typically Zn, Co) ions and imidazolate linkers to give zeolite-like structure.[125] ZIFs show exceptional chemical stability and are versatile structures *via* incorporation of various functionalised organic linkers, and have

been widely explored for applications in gas sorption,[126] small molecule separation,[127] and catalysis.[128] The H_2 adsorption properties of the archetypal ZIF-8[129] has been investigated in detail using NPD.[130] ZIF-8 is comprised of tetrahedral ZnN_4 units bridged by 2-methylimidazolate (MeIM) to give a sodalite zeolite-type structure. The framework can be viewed as body-centred cubic packing of truncated octahedral cages, each with internal diameter of 11 Å, in which four Zn(II) ions and four MeIM rings form a 4 Å square aperture and six ZnN_4 clusters and six MeIM rings generate a hexagonal face. The NPD data were collected at different D_2 loadings at 3.5 K, and six distinct D_2 binding sites were identified and sequentially occupied with increasing loadings (Fig. 34). The strongest adsorption sites are directly associated with the organic moieties, with site D1 residing on top of the MeIM ring close to the C=C bond in the MeIM unit, and site D2 located at the centre of the hexagonal face. The third site (D3) is also located is at the centre of the hexagonal opening but on the other side of the aperture. The fourth site (D4) was found in the face centre of the D_2 nanocage formed by the first three binding sites. With further loading of 28 D_2 per 6 Zn at 3.5 K, two additional sites D5 and D6 sited close to the centre of the 11 Å cage were progressively occupied.

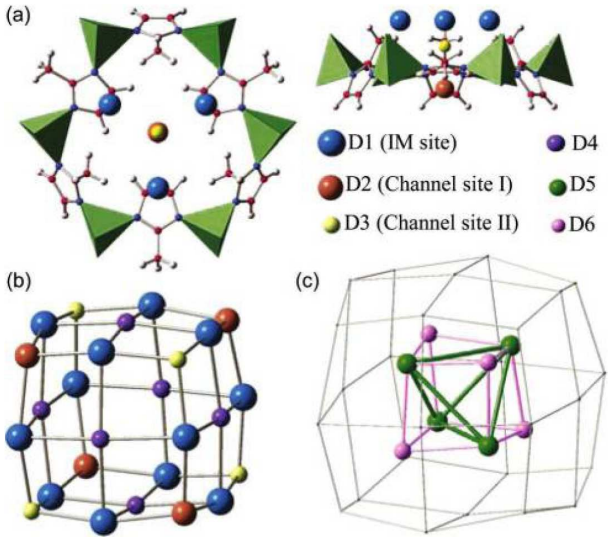

Figure 34. The adsorption sites for D_2 obtained by Fourier difference analysis of the NPD data: (a) top and side views of the first three adsorption sites near the hexagonal face; (b) pseudocubic nanocage formed by D1, D2, and D3 sites; (c) tetrahedron-like nanocage formed by D5 and D6 sites. Reproduced from Ref 130.

3.4 Selective CO_2 binding in amine-functionalised MOFs

It is widely accepted that MOFs containing pendant amine functional group can have specific binding to CO_2 molecules, thus improving the selectivity and uptake capacity of CO_2 in the host. However, experimental evidence on the direct visualisation of $NH_2\cdots CO_2$ binding in MOFs has only been reported in exceptional cases.[131] For example, Shimizu *et al*. have reported the location of CO_2 molecules in $[Zn_2(Atz)_2(ox)]_\infty$ (Atz^{2-} = 3-amino-1,2,4-triazole; ox^{2-} = oxalate) *via in situ* single crystal diffraction and confirmed the strong interaction of amines with CO_2 with a heat of adsorption of *ca*. 40 kJ mol^{-1}.[131, 132] Two binding sites for CO_2 were located: site I is close to the free amine group and forms a strong dipole interaction and site II is in the middle of the pore forming "T-shape" interaction with the CO_2 residing on site I (Fig. 35).

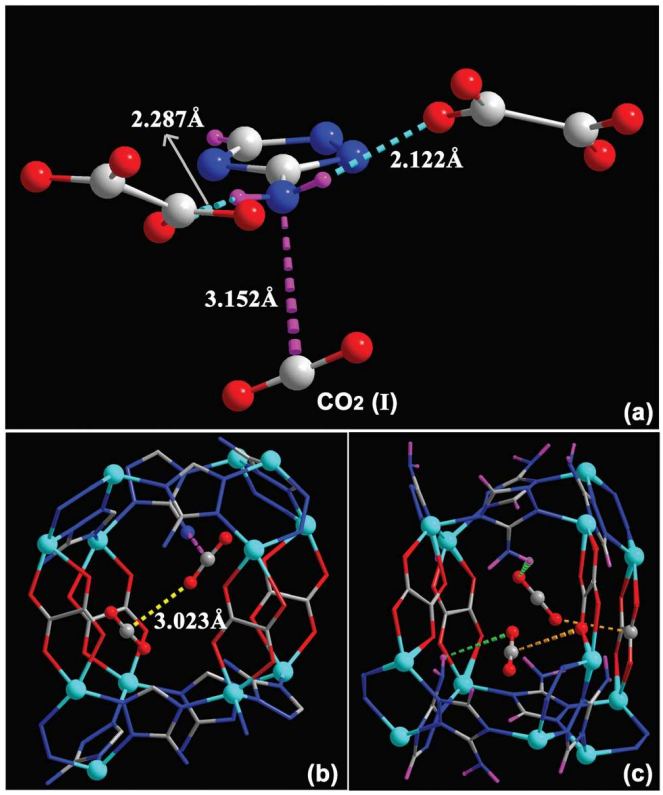

Figure 35. (a) View of X-ray structure of CO_2-loaded $[Zn_2(Atz)_2(ox)]\cdot(CO_2)_{1.3}$ at 173 K. The H atoms of the amine group (located crystallographically) hydrogen bond to oxalate O-centres, directing the N lone pair toward the C(+) atom of the CO_2 molecule. Hydrogen bond distances shown are for H-acceptor interactions. (b) View of the crystallographically independent CO_2 molecules trapped in a pore *via* cooperative interaction between CO_2-I and CO_2-II molecules. The $CO_2\cdots NH_2$ interaction is represented as a dotted purple bond, and the $CO_2\cdots CO_2$ interaction is indicated as a dotted yellow bond. (c) The $CO_2\cdots$oxalate interactions are shown in orange, and the $CO_2\cdots NH_2$ hydrogen bond interactions are shown in green. For clarity, H atoms are shown in purple. Reproduced from Ref 131.

$[Zn_2(Atz)_2(ox)]_\infty$ was compared to the phosphonate analogue, $[Zn_3(Atz)_3(PO_4)]_\infty$, with the hypothesis that the latter might give better CO_2 capture properties.[133] Fewer trianionic phosphonate groups per metal are required to provide charge-balance than dianionic oxalates, and larger amine-lined pores were anticipated and indeed observed. However, CO_2 uptake did not exceed that of $[Zn_2(Atz)_2(ox)]_\infty$ and the adsorbed CO_2 molecules could not be readily located in $[Zn_3(Atz)_3(PO_4)]$ by diffraction experiments. The porous 3D networks in both cases are made up of cationic Zn-Atz layers pillared by the anions (Fig. 36). Only the triazole nitrogens of the aminotriazole ligand are coordinated to Zn(II), with the amine N-centres remaining uncoordinated. The structure of $[Zn_3(Atz)_3(PO_4)]_\infty$ does indeed have larger pores, but the ZnAtz layers of the structure adopt a buckled or staggered conformation which results in the amines not pointing directly into the pores. Classical GCMC and MD simulations and periodic DFT calculations were used to model the CO_2 adsorption isotherms, heats of adsorption and locations of CO_2 molecules (Fig. 37) in both MOFs. The isotherms were modelled with excellent agreement in both cases, with the exception of a slight overestimate of the CO_2 adsorption of $[Zn_3(Atz)_3(PO_4)]_\infty$ at low pressure.

The GCMC and DFT calculations located CO_2 molecules in two regions in $[Zn_3(Atz)_3(PO_4)]_\infty$, denoted as α and β in Fig. 37. It is noteworthy that the electrostatic interactions of CO_2 in the α_1 binding site with the amine groups were calculated to be weakly attractive for two adjacent amines but repulsive for the third; in the oxalate framework all these interactions were found to be attractive. Interestingly, occupation of the $\alpha_1/\alpha_2/\beta$ triad of binding sites in $[Zn_3(Atz)_3(PO_4)]_\infty$ by three CO_2 molecules was calculated to have an average binding energy of 31.3 kJ mol^{-1} per CO_2 molecule, a full 7.4 kJ mol^{-1} higher than the mean average of the individual binding energies of the sites in an empty framework (30.6, 26.9 and 29.0 kJ mol^{-1} respectively). However, immediately adjacent α_1 and α_2 sites are mutually exclusive (red and blue sites in Fig. 37c) and so a dynamic 'slipping' of CO_2 between these positions was proposed as a mechanism to benefit from favourable site-site cooperative binding effects. Therefore, *ab initio* MD simulations on four CO_2 molecules in a single unit cell were performed to investigate the mobility of CO_2. The results are shown in Fig. 37d: two of the four calculated regions resulting from a 35 ps MD simulation are depicted and broadly the same regions are identified as by the GCMC simulations. Slipping of the CO_2 molecules between α and β sites was observed in this short simulation and snapshots show the triad formation arises when this occurs.

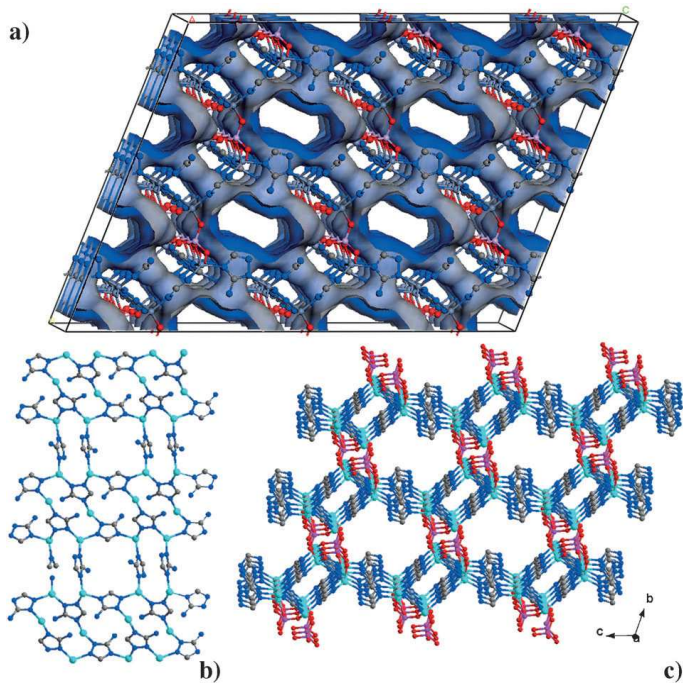

Figure 36. Structure of $[Zn_3(Atz)_3(PO_4)]_\infty$ (solvent molecules omitted for clarity). (a) Connolly surface representation showing the three-dimensional structure of the Zn–Atz layers pillared by phosphate groups. (b) Ball-and-stick representations showing the zinc–aminotriazolate layer, and (c) the structure showing the layering of the Atz^{2-} ligands. C grey, N dark blue, O red, P purple, Zn pale blue. Reproduced from Ref 133.

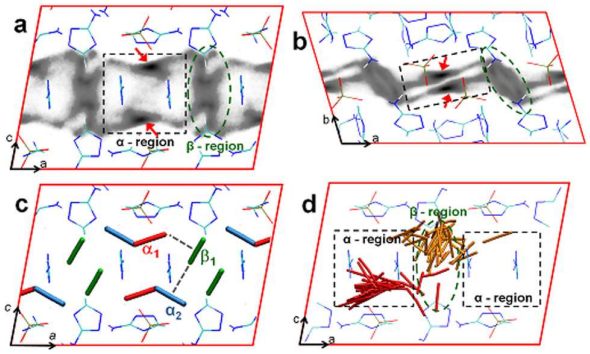

Figure 37. Centre-of-mass probability-density plots of CO_2 molecules in $[Zn_3(Atz)_3(PO_4)]_\infty$ at 273 K and 850 mbar pressure. Black dashed boxes: α region; green: β region. Shown are probability densities that are (a) projected onto the *ac* plane, and (b) projected onto the *ab* plane. (c) Selected CO_2 binding-site geometries optimized at the DFT level. Symmetry-equivalent CO_2 molecules are represented in the same color. (d) Trace of two CO_2 molecules (red and orange) during a 35 ps ab initio MD simulation of $[Zn_3(Atz)_3(PO_4)]_\infty$ at 273 K with a loading of four CO_2 molecules per unit cell (the other two CO_2 molecules are not shown). Thirty snapshots, separated by 1.2 ps, are depicted. For (a)–(d), a 2×1×1 representation of the unit cell is shown that is shifted by 0.5 in the *a* direction in (d). Reproduced from Ref 133.

In conclusion, this study neatly demonstrates that simulation of parameters for the individual binding site of CO_2 in a framework needs to be combined with experimental and computational analysis of the molecular dynamics of the guest and the more subtle intermolecular interactions between CO_2 molecules in different binding sites. It also demonstrates that excessive clustering of amine groups actually hinders CO_2 binding rather than enhancing it.

4. Gas binding in a family of hydroxy-decorated MOFs, MFM-300(M) (M = Al, Ga, In)

4.1 Selective gas binding in MFM-300(Al)

Selective capture and removal of harmful flue gases (*e.g.,* CO_2, SO_2) is a major challenge for power stations and coal-fired industry. Materials functionalised with amine-groups dominate this area, primarily because of their potential to form carbamates *via* $H_2N(\delta^-)\cdots C(\delta^+)O_2$ interactions, thereby trapping CO_2 covalently.[134, 135] The use of these materials, however, is energy-intensive, with significant environmental impact. The development of alternative materials without incorporating toxic amine-groups can potentially reduce the energy and environmental penalties. Recently, a non-amine-containing material MFM-300(Al) (MFM = Manchester Framework Material, replacing the previous NOTT designation) in which hydroxy groups within pores bind CO_2 and SO_2.[136] *In situ* synchrotron PXRD and INS studies, combined with modelling have demonstrated the power in revealing the preferred binding sites and dynamics for adsorbed gas molecules.

MFM-300(Al) comprises of infinite chains of $[AlO_4(OH)_2]$ moieties bridged by biphenyl-3,3',5,5'-tetracarboxylate ligands to affords a porous extended framework structure with square-shaped 1D channels with hydroxy groups protruding into them (Fig. 38a). The diameter of the channel window, taking into account the van der Waals radii of the surface atoms, is approximately 6.5 Å. Desolvated MFM-300(Al) has a pore volume of 0.38 cc g^{-1} and a BET surface area of 1370 m^2 g^{-1} and so the general porosity of MFM-300(Al) is moderate within the family of MOF complexes.[136,137] Desolvated MFM-300(Al) shows highly selective uptake for CO_2 (7.0 mmol g^{-1}) and SO_2 (8.1 mmol g^{-1}) at 273 K and 1.0 bar, among the highest values observed so far under these conditions. While under the same conditions the isotherms for CH_4, CO, N_2, H_2, O_2, and Ar show only surface adsorption by MFM-300(Al), with very low uptake of gas, and thus giving ultra-high selectivities for CO_2 and SO_2, indicating the potential of MFM-300(Al) for the selective capture of these harmful gases.

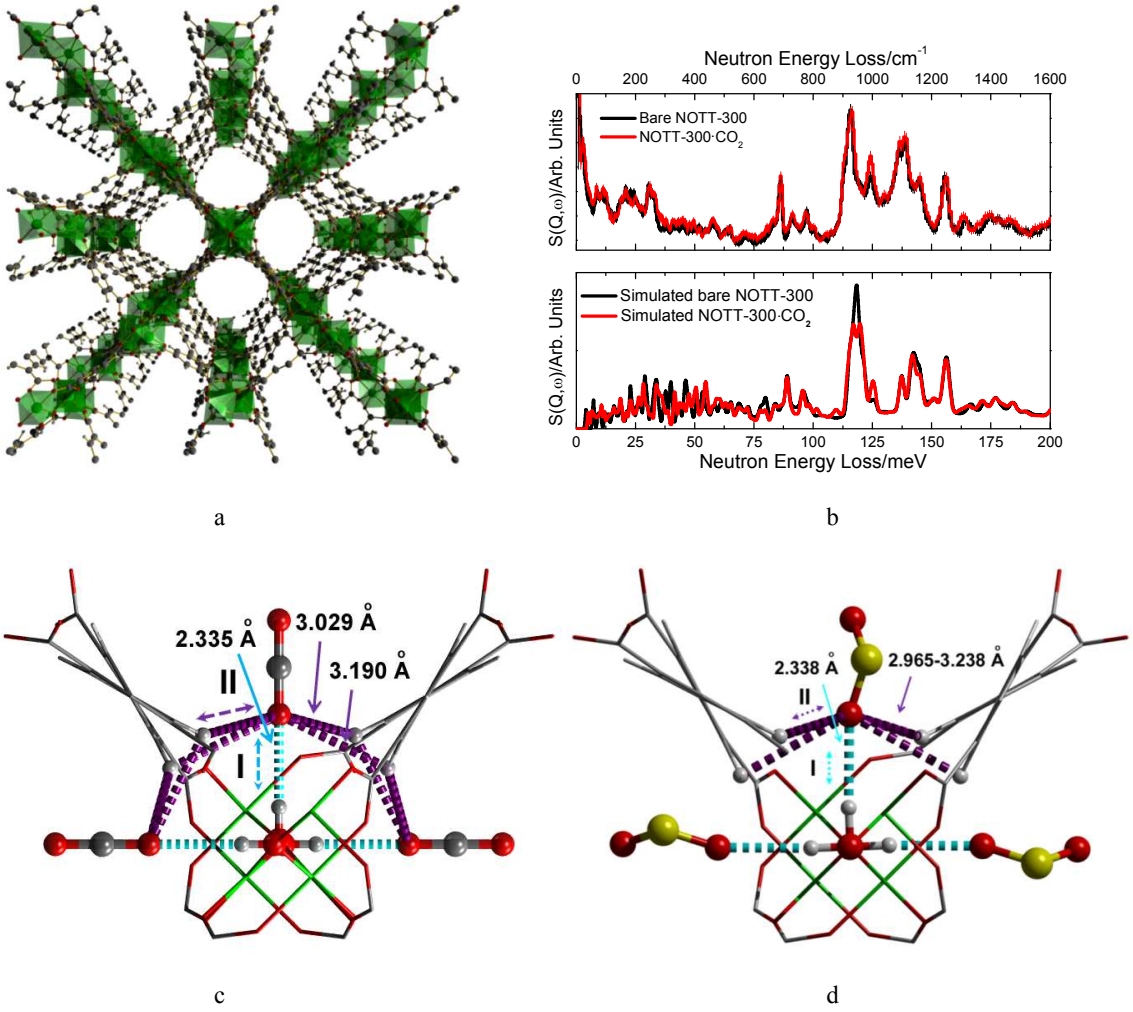

Figure 38. (a) View of the crystal structure for MFM-300(Al); (b) comparison of the experimental (top) and DFT simulated (bottom) INS spectra for bare and CO_2-loaded MFM-300(Al). Detailed view of the role of the -OH and -CH groups in binding (c) CO_2 and (d) SO_2 molecules in a "pocket-like" cavity of MFM-300(Al) (Al: green; carbon: grey; oxygen: red; hydrogen: white). Reproduced from Ref 136.

Static studies using NPD have been previously been employed to locate CO_2 in porous MOFs,[82,88] but although INS has been used widely to investigate the H_2 binding interactions within various MOF, this technique cannot directly detect the CO_2 binding interaction within a porous system because the scattering cross-sections for carbon and oxygen are too small to obtain reasonable signal (Table 1). A combination of INS and DFT can however indirectly visualise binding of CO_2 molecules within MFM-300(Al) by investigating the change in the dynamics of the hydrogen atoms in the local structure, including those of the hydroxy groups and benzene rings of the ligand. Two major changes on the INS spectra were observed upon

CO_2 loading into MFM-300(Al), indicating the presence of two distinct types of interactions involved in binding CO_2 in the pore (Fig. 38b). DFT calculations based on INS results confirm that the adsorbed CO_2 molecules interact end-on to the hydroxy groups *via* the formation of a moderate-to-weak hydrogen bond (O···H = 2.335 Å). In addition, each adsorbed CO_2 molecule is surrounded by four aromatic C-H groups, forming weak cooperative supramolecular interactions between O(δ-) of CO_2 and H(δ+) from -CH [O···H = 3.029, 3.190 Å] (Fig. 38c). This calculation is in excellent agreement with the experimental INS data and confirms the presence of both moderate-to-weak hydrogen bonds and supramolecular interactions.

The preferred binding sites for CO_2 molecules within MFM-300(Al) have also been determined by static *in situ* PXRD analysis which also confirms end-on binding of CO_2 to both the hydroxy group and the surrounding C-H groups. This PXRD analysis is in excellent agreement with the INS/DFT model. Additionally, a second CO_2(II) site has been identified from this PXRD analysis, and this interacts principally with the first CO_2 *via* dipole interaction, similar to that observed in solid CO_2.

The corresponding INS/DFT and PXRD studies on SO_2-loaded MFM-300(Al) lead to similar observations revealing the presence of three different types of binding interactions: moderate-to-weak hydrogen bonds to hydroxy group (CO_2···HO-), supramolecular interactions to aromatic hydrogen atoms (CO_2···HC-) and intermolecular dipole interactions between adsorbed SO_2 molecules. The binding mechanism in this case is very similar to that observed in CO_2-loaded MFM-300(Al), albeit SO_2 has a bend structure with <O=S=O angle of ~110 degree (Fig. 38d). Significantly, *in situ* PXRD of SO_2-loaded sample confirms retention of the structure of MFM-300(Al) upon inclusion and subsequent removal of SO_2, thereby confirming the high stability of MFM-300(Al) in the presence of corrosive SO_2. This is highly unusual for porous MOF materials that often react irreversibly with SO_2.

Notwithstanding the high uptake of CO_2 and SO_2 observed for MFM-300(Al), it shows surprisingly low uptake for H_2 (0.22 wt% at saturation at 77 K). This is almost ten-fold lower than the expected H_2 uptake of 2.7 wt% based upon the pore volume and BET surface area of MFM-300(Al). As discussed above for the series of Cu(II)-tetracarboxylate MOFs in which lower H_2 uptake was observed with increasing pore size,[13-15] computational modelling widely predicts that MOFs incorporating ultra-micropores (below 10 Å) are optimal for H_2 binding due to enhanced overlapping potentials. The exceptionally low H_2 uptake for MFM-300(Al) is thus highly unusual. INS has been used to study the H_2 binding interaction owing to its large incoherent cross-section (Table 1) and therefore high detection sensitivity. INS spectra of H_2-loaded MFM-

300(Al) display a broad hump centred at ~20 meV with only one small energy transfer peak at 8.8 meV (Fig. 39).[138] This result suggests that the majority of adsorbed H_2 in the pore has a recoil motion at 5 K (below its melting point), reminiscent of the behaviour of liquid H_2. This observation is distinct from previous studies on adsorbed H_2 displaying binding to open metal sites, which induce clear host-guest interactions to H_2. Thus, the INS spectra suggests that adsorbed H_2 molecules have very weak interactions with the MFM-300(Al) host and, therefore, can rotate freely in the channel to give recoil rotational motion. This study represents a unique example of surprisingly low H_2 uptake within an ultra-microporous (~6 Å) MOF material, and complements the wide range of studies on systems showing higher uptake capacities and binding interactions, several of which are highlighted in this review.

a b

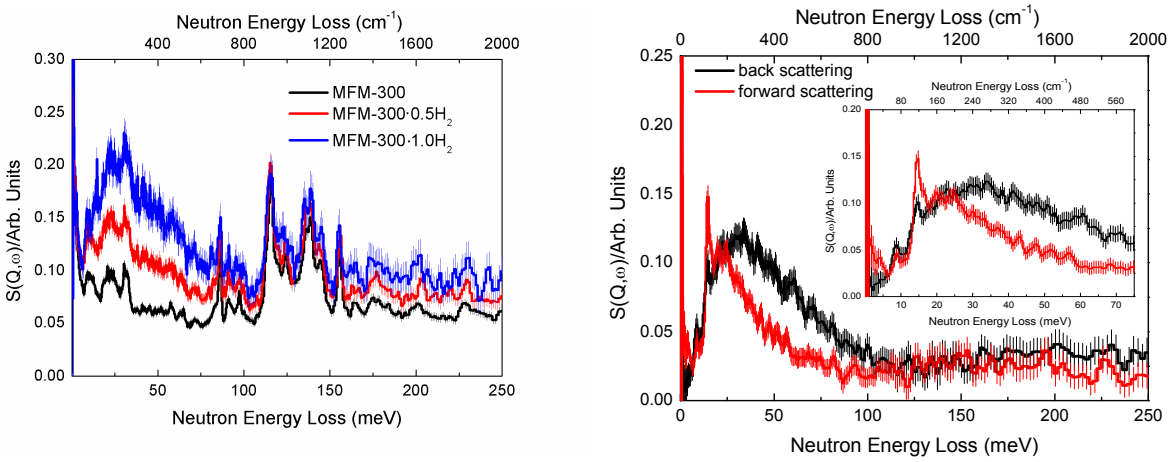

Figure 39. (a) Comparison of INS spectra for bare MFM-300(Al), MFM-300(Al)·0.5 H_2 and MFM-300(Al)·1.0 H_2. (b) Difference INS spectra between MFM-300(Al) and MFM-300(Al)·1.0 H_2. A detailed view of the low energy transfers is shown as inset figure. Reproduced from Ref 138.

The excellent performance of MFM-300(Al) in the capture of CO_2 and SO_2 motivated a study on the separation of small molecule hydrocarbons.[139] At 293 K, the total adsorption uptakes for C_2H_2, C_2H_4, C_2H_6, and CH_4 in MFM-300(Al) were measured as 6.34, 4.28, 0.85, 0.29 mmol g^{-1}, respectively at 1.0 bar. Analysis of the pure-component isotherms at 293 K *via* ideal adsorbed solution theory (IAST)[140] was carried out to estimate selectivity between these hydrocarbons. For equimolar mixtures at 1.0 bar, the C_2H_2/C_2H_4 selectivity of 2.30 for MFM-300(Al) by IAST is higher than that oserved for [Fe_2(dobdc)] (1.87),[59] but is lower than for M'MOF-3a (5.23),[141] although the latter system exhibits a relatively low total capacity owing

to the narrow pore. The selectivity for C_2H_4/C_2H_6 in MFM-300(Al) was calculated to be 48.7. Significantly, this value is higher than that observed for the current state-of-the-art ethylene/ethane separating materials.[50,59,142-144] The C_2H_2/CH_4, C_2H_4/CH_4, and C_2H_6/CH_4 selectivities in MFM-300(Al) were estimated by IAST analysis as >1000, ~380, and 5, respectively. The above IAST selectivity data were also validated *via* the measurement of dual-component adsorption isotherms for equimolar mixtures of C_2H_2/C_2H_4, C_2H_4/C_2H_6, C_2H_2/CH_4, and C_2H_4/CH_4 at 293 K under flow mode, indicating the preferred binding of unsaturated hydrocarbons to MFM-300(Al) host.

The binding sites for C_2H_2, C_2H_4, and C_2H_6 were studied by *in situ* synchrotron PXRD and NPD experiments. Two independent binding sites (I and II) were observed in each case: the unsaturated C_2-molecules at Site I exhibit a side-on interaction to the HO-Al group *via* formation of weak hydrogen bonds that are supplemented by additional supramolecular contacts to the aromatic hydrogen atoms and π···π interactions to the phenyl rings; C_2-molecules at Site II are located in the middle of the pore and interact primarily with the molecules at Site I *via* intermolecular dipole interactions. The bond distances obtained from independent analysis of synchrotron X-ray diffraction, neutron diffraction, and DFT calculations are compared in Fig. 40 with very good agreement observed between the three methods. In addition to the static crystallography study, a combined INS and DFT study was undertaken to visualise the binding dynamics for adsorbed C_2H_2, C_2H_4, and C_2H_6 molecules in MFM-300(Al). The study revealed a novel the Al-OH to π(C≡C) hydrogen-bond interaction, which has not been observed previously, and thus represents a new type of supramolecular contact in host-guest systems. This study reveals the involvement of simultaneous and cooperative hydrogen-bonding, π···π interactions and inter-molecular dipole interactions in the binding of acetylene and ethylene to give up to twelve individual weak supramolecular interactions aligned within the host to form an optimal geometry for intelligent selective binding of hydrocarbons.

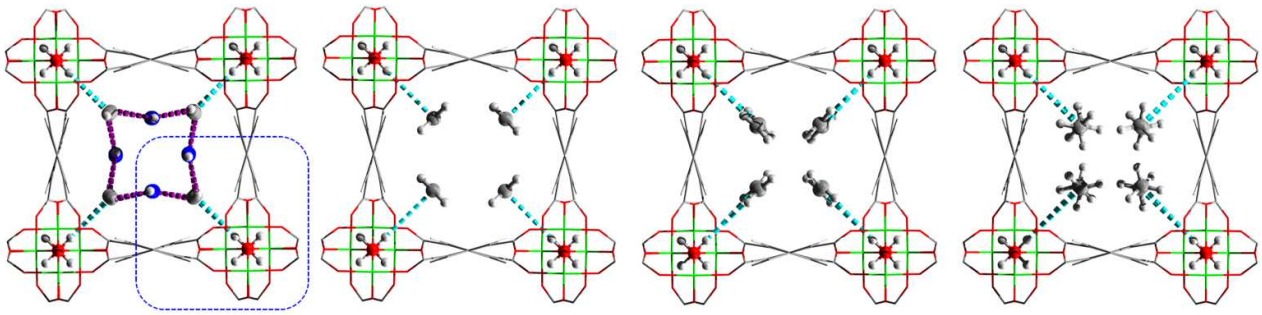

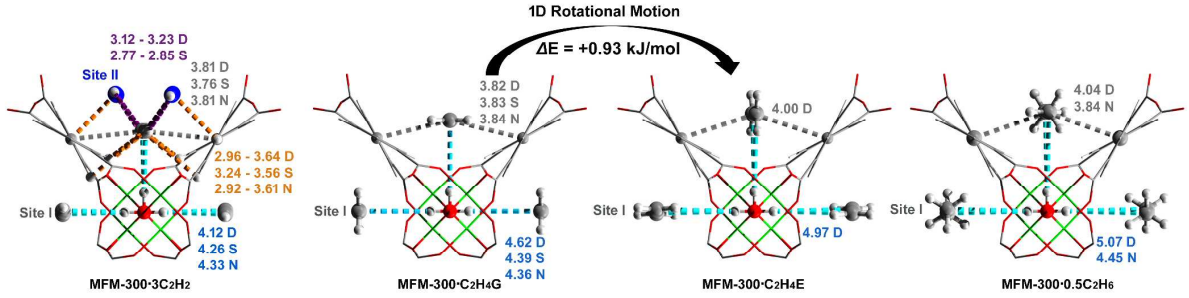

a b c d

Figure 40. Views of the structural models for (a) MFM-300(Al)·$3C_2H_2$, (b) MFM-300(Al)·C_2H_4G, (c) MFM-300(Al)·C_2H_4E and (d) MFM-300(Al)·C_2H_6 (Al: green; carbon: grey; oxygen: red; hydrogen: white). These models were generated from DFT optimisations based upon the structural models obtained from synchrotron and neutron powder diffraction experiments. The details of the host-guest binding as shown in the blue square are enlarged and shown in the bottom row for each of the corresponding model. Hydrocarbon molecules in the channel and the host functional groups involved in cooperative binding are highlighted by the use of ball-and-stick mode. The π···HO hydrogen-bonds, π···π, and C···H supramolecular interactions, and inter-molecular dipole interactions are highlighted in cyan, grey, orange, and purple, respectively. The carbon atoms of second site of C_2H_2 are highlighted in blue. Sites I and II represent two preferred binding sites within the pore: molecules at Site I interacts with the Al-OH groups and those at Site II bind primarily with molecules at Site I via dipole interactions. The energy barrier for 1D rotational motion between MFM-300(Al)·C_2H_4G and MFM-300(Al)·C_2H_4E was estimated to be 0.93 kJ mol^{-1}. The bond distances obtained from DFT calculations, synchrotron PXRD and NPD are labelled as D, S and N, respectively, and are shown in Å. Due to the uncertainty of the hydrogen atom location, the π···HO hydrogen-bonds are described *via* the distance between the O-centre and the centroid of the C_2 bond of hydrocarbon molecules. Reproduced from Ref 139.

The separation of C_2H_2 and C_2H_4 is a technologically important goal, but is highly challenging due to their similar molecular sizes, volatilities, and electronic structures based upon unsaturated carbon-carbon bonds. This leads to very similar binding interactions for these substrates to open metal sites, with low preferential adsorption.[50,59,142] The dynamics of MFM-300(Al) loaded with an equimolar mixture of C_2H_2/C_2H_4 were analysed to determine the relative binding of these two guests, and confirmed that in this binding competition, C_2H_2 has a stronger interaction to the host than C_2H_4 and directly supports the optimal selectivity and uptake capacity observed in the isotherm experiments. This INS study represents the first dynamic study of competing C_2-hydrocarbons binding in a functional host material.

This work represents a classic example of applying *in situ* INS, NPD, PXRD and DFT techniques to analyse dynamic and structural properties of gas-loaded MOF materials to reveal that a combination of multiple weak supramolecular binding interactions is sufficient enough to bind CO_2, SO_2, C_2H_2, C_2H_4, and C_2H_6 molecules with both high selectivity and capacity. This offers the potential for application of new "easy-on/easy-off" capture systems for selective gas binding and separations that carry fewer economic and environmental penalties.

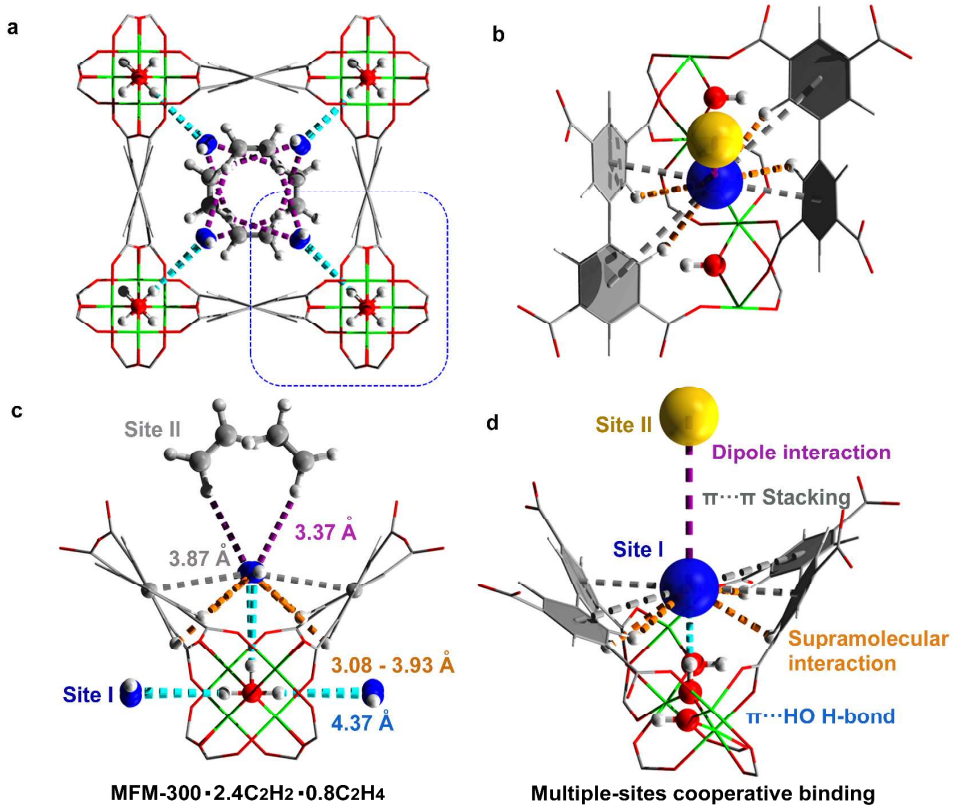

Figure 41. Views of the calculated structural models for C_2H_2-C_2H_4 mixture-loaded MFM-300(Al) (MFM-300(Al)·2.4C_2H_2·0.8C_2H_4) (Al: green; carbon: grey; oxygen: red; hydrogen: white). (a) and (c) Views of the structure of MFM-300(Al)·2.4C_2H_2·0.8C_2H_4 obtained from DFT calculations based upon INS spectra. The details of the host-guest binding as shown in the blue square are enlarged and shown in (c). The bond distances were obtained from DFT optimisation. The adsorbed C_2H_2 and C_2H_4 molecules in the pore are highlighted by the use of ball-and-stick mode. The carbon atoms of C_2H_2 are highlighted in blue. (b) and (d) Schematic views of the role of the –OH, -CH and phenyl ring groups in binding C_2H_2 and C_2H_4 molecules in a "pocket-like" cavity. Sites I and II represent two preferred binding sites within the pore, and are shown by blue and yellow balls, respectively. The π···HO hydrogen-bonds, π···π and C···H supramolecular interactions, and inter-molecular dipole interactions are highlighted in cyan, grey, orange, and purple, respectively. Reproduced from Ref 139.

4.2 Selective CO_2 binding in MFM-300(Ga_2) and MFM-300($Ga_{1.87}Fe_{0.13}$)

MOFs are usually synthesised using a single type of metal ion, and those containing mixtures of different metal ions are of great interest and represent a methodology to enhance and tune materials properties. MFM-300(Ga_2) is isostructural[145] with the Al(III) analogue MFM-300(Al)[136] with pores decorated with -OH groups bridging Ga(III) centres. The isostructural Fe-doped material [$Ga_{1.87}Fe_{0.13}(OH)_2(L)$], MFM-300($Ga_{1.87}Fe_{0.13}$) can be prepared under similar conditions to MFM-300(Ga_2) *via* reaction of a homogeneous mixture of $Fe(NO_3)_3$ and $Ga(NO_3)_3$ with biphenyl-3,3',5,5'-tetracarboxylic acid.[145] Thus, Fe-doping can be used to monitor the effects of the heteroatom center within a parent Ga(III) framework without the requirement of synthesising the isostructural Fe(III) analogue MFM-300(Fe_2). MFM-300(Ga_2) shows the highest CO_2 uptake (2.86 mmol g^{-1} at 273K at 1 bar) for a Ga-based MOF. Fe-doping of MFM-300(Ga_2) affords positive effects on gas adsorption capacities, particularly for CO_2 adsorption, whereby MFM-300($Ga_{1.87}Fe_{0.13}$) shows a 49% enhancement of CO_2 adsorption capacity in comparison to the homo-metallic parent material. The single crystal X-ray structures of MFM-300(Ga_2)-solv, MFM-300(Ga_2), MFM-300(Ga_2).2.35CO_2, MFM-300($Ga_{1.87}Fe_{0.13}$)-solv, MFM-300($Ga_{1.87}Fe_{0.13}$), and MFM-300($Ga_{1.87}Fe_{0.13}$).2.0CO_2 have been determined at 195 K (Figs. 42,43).[145]

Upon loading of CO_2 into the hosts, significant residual electron density was found in the pore by difference Fourier map analysis, and was sequentially assigned as two independent CO_2 molecules populating at sites I (O_{1s}=C_{1s}=O_{2s}) and II (O_{3s}=C_{2s}=O_{4s}). In MFM-300(Ga_2), the occupancy for these CO_2 molecules at sites I and II refined to values of 0.43(3) and 0.74(3), respectively, yielding the overall formula [$Ga_2(OH)_2(C_{16}H_6O_8)$]·2.35CO_2 for the CO_2-loaded material. The CO_2 at site I is ordered and binds to the –OH group in an end-on fashion *via* a moderate hydrogen bonding interaction [H···O_{1s} = 1.883(10) Å; <O-H···O_{1s} = 180°]. Interestingly, this hydrogen bond distance is much shorter than that observed in MFM-300(Al_2)·3.2CO_2 system [H···O = 2.376(13) Å; <O-H···O = 180°] studied by *in situ* PXRD at 273 K,[136] indicating the formation of a stronger hydrogen bonding interaction in MFM-300(Ga)·2.35CO_2. Given that MFM-300(Ga_2) and MFM-300(Al_2) have the same framework structure and pore surface chemistry, this difference in hydrogen bond length is most likely due to the different metal centre (Al or Ga) affecting the relative acidity of the M-OH (M = Al, Ga) group. The CO_2 at site II is disordered over two equally-occupied positions. In contrast to CO_2^I, CO_2^{II} does not interact directly with framework atoms instead forming two

weak electrostatic dipole interactions with CO_2^I, between the electropositive C and electronegative O centres [$C_{1s}\cdots O_{3s}$= 3.85(4) Å; $C_{2s}\cdots O_{2s}$= 4.39(4) Å]. Significantly, this pattern of intermolecular interactions is distinct from the traditional "T-shape" dipole interaction observed in solid CO_2, in $[Zn_2(Atz)_2(ox)].1.3CO_2$ (Atz^{2-} = 3-amino-1,2,4-triazole; ox^{2-} = oxalate)[131] and in MFM-300(Al_2).3.2CO_2.[136]

In contrast, the occupancies of the CO_2 molecules at sites I and II in MFM-300($Ga_{1.87}Fe_{0.13}$) both refined to values of 0.50 (1), yielding a formula of $[Ga_{1.87}Fe_{0.13}(OH)_2(C_{16}H_6O_8)].2.0CO_2$ for the CO_2-loaded material. The CO_2 at site I is ordered and binds to the -OH group in an end-on fashion *via* a weak hydrogen bonding interaction [$H\cdots O_{1s}$ = 2.259(12) Å, <O-H$\cdots O_{1s}$ = 180°]. Interestingly, this hydrogen bond distance is longer than that observed in the MFM-300(Ga_2).2.35CO_2 system [$H\cdots O_{1s}$ = 1.883(10) Å] indicating the formation of a weaker hydrogen bonding interaction in MFM-300($Ga_{1.87}Fe_{0.13}$).2.0CO_2. This is consistent with the observed heat of adsorption which also decreases. The CO_2 at site II is disordered over two equally-occupied positions. However, CO_2^{II} adopts a different orientation to that observed in MFM-300(Ga_2).2.35CO_2, forming a typical "T-shape" dipole interaction with CO_2^I between the electropositive C centre and electronegative O centre [$C_{1s}\cdots O_{3s}$ = 3.207(6) Å, occurring twice]. Thus, the small percentage of Fe-doping into this solid solution has significant effect on the CO_2 binding details, including the formation of both adsorbate-adsorbent hydrogen bond and adsorbate-adsorbate intermolecular dipole interactions.

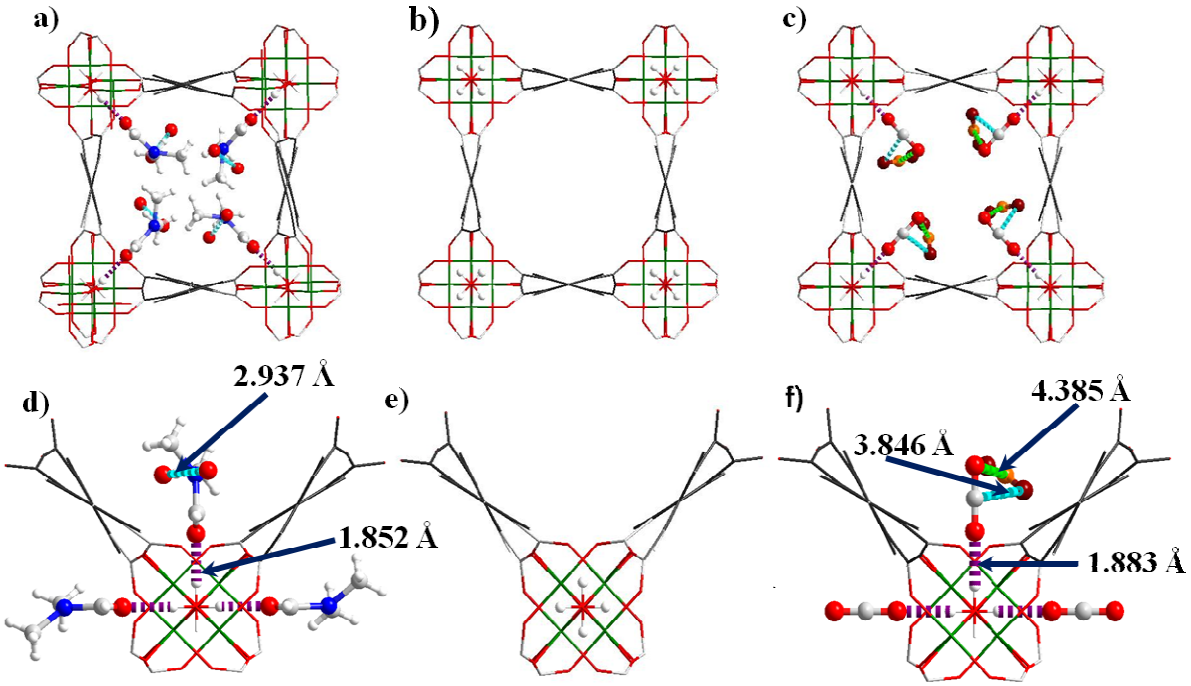

Figure 42. Views of single crystal structures of (a) and (d) MFM-300(Ga_2)-solv; (b) and (e) MFM-300(Ga_2) activated at 393 K and vacuum 10^{-4} mbar for 4 h; (c) and (f) MFM-300(Ga_2).2.35CO_2, loaded with CO_2 at 1 bar at 195 K for 2h. The guest molecules (DMF, water, CO_2) in the channels are highlighted using a ball-and-stick style (Ga: green; C: grey; O:red; H: white; N: blue). The carbon atom of CO_2^{II} is highlighted in orange. The hydrogen bonding interaction between the guest molecule and free –OH group is highlighted in purple. The electrostatic dipole interactions between CO_2 molecules are highlighted in cyan ($O_{3s}\cdots C_{1s}$) and green ($O_{2s}\cdots C_{2s}$). Reproduced from Ref 145.

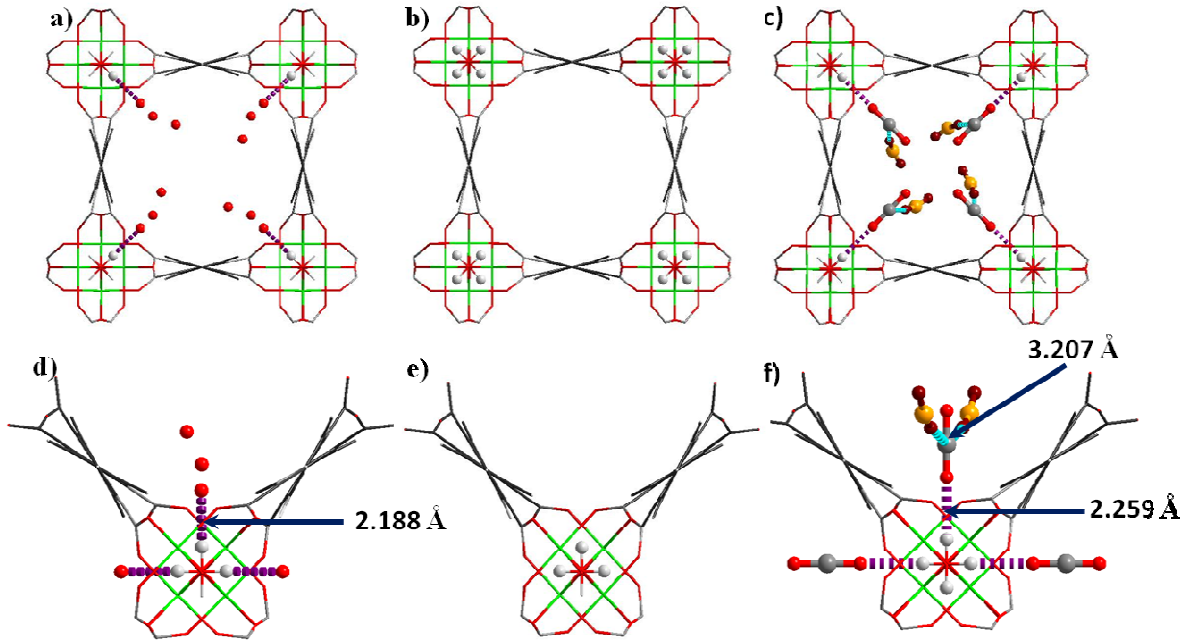

Figure 43. Views of single crystal structures of (a) and (d) MFM-300($Ga_{1.87}Fe_{0.13}$)-solv; (b) and (e) MFM-300($Ga_{1.87}Fe_{0.13}$), activated at 393 K and vacuum 10^{-4} mbar for 4h; (c) and (f) MFM-300($Ga_{1.87}Fe_{0.13}$).2.0CO_2, loaded with CO_2 at 1 bar at 195 K for 2h. The guest molecules (DMF, water, CO_2) in the channels are highlighted as ball-and-stick models (Ga: green; C: grey; O: red; H: white; N: blue). The carbon atom of CO_2^{II} is highlighted in orange. The hydrogen bonding interaction between the guest molecule and free -OH group is highlighted in purple. The electrostatic dipole interactions between CO_2 molecules are highlighted in cyan ($O_{3s}\cdots C_{1s}$) and green ($O_{2s}\cdots C_{2s}$). Reproduced from Ref 145.

4.3 CH_4 and D_2 binding in MFM-300(In)

The microporous hydroxy-decorated material, MFM-300(In) displays a high volumetric uptake of 202 v/v at 298 K and 35 bar for CH_4 and 488 v/v at 77 K and 20 bar for H_2.[146] Direct observation and quantification of

adsorbed H_2 and CH_4 molecules within MFM-300(In) have been achieved using a combination of NPD and INS techniques coupled with computational investigations. These complementary results suggest that the adsorbed CH_4 molecules form specific interactions with metal-bound hydroxy groups within the pore, supplemented by intermolecular dipole interactions between adsorbed CH_4 molecules and the phenyl-ring lined walls of the pore (Fig. 44). These cooperative supramolecular interactions allow packing of CH_4 to very high density upon saturation (0.37 g cm^{-3}) reminiscent of liquid CH_4 (0.42 g cm^{-3} at 111 K) and 71 % of that of the solid (0.52 g cm^{-3} at 20.4 K). Interestingly, the $H_4C^{guest}\cdots H\text{-}O^{host}$ interaction represents the first example of such molecular contact in MOFs, and contrasts with the structures observed in CH_4/water clathrate materials in which the CH_4 molecule is orientationally disordered and not observed to interact with the H···OH cage-forming linkage (Fig. 45).[147] Similar binding has also been observed in H_2-loaded MFM-300(In).

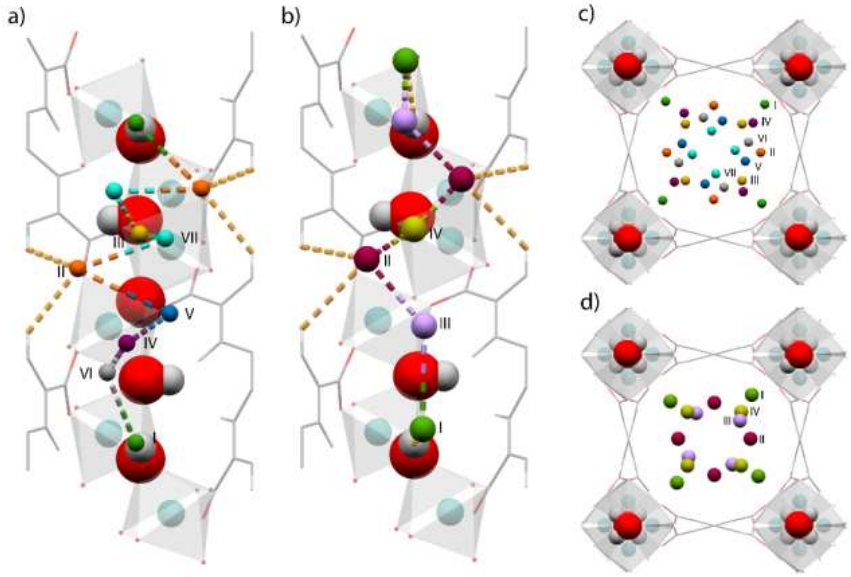

Figure 44. View of the crystal structure of H_2/CH_4 loaded MFM-300(In) showing; (a) and (b) views of the corner-sharing extended $[InO_4(OH)_2]$ chain highlighting interactions between the framework structure with D_2 and CD_4 molecules, respectively; (c) and (d) views of the *c*-crystallographic axis showing the positions of the adsorbed D_2 and CD_4 molecules respectively. D_2 molecules in (a) and (c) are coloured according to the scheme: Site I, green; Site II, orange; Site III, yellow; Site IV, purple; Site V, blue; Site VI, grey; Site VII, light blue. CD_4 molecules in (b) and (d) are coloured according to the following scheme: Site I, green; Site II, orange; Site III, yellow; Site IV, purple; Site V, blue; Site VI, grey; Site VII, light blue. Reproduced from Ref 146.

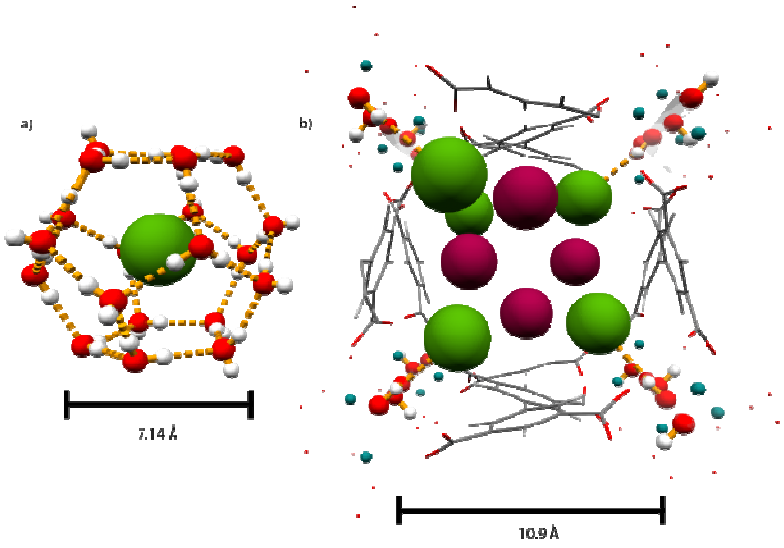

Figure 45. Views of (a) the cage structure and $H_3C\text{-}H^{guest}\cdots O^{host}$ interaction of CH_4 in a clathrate; (b) the channel and $H_4C^{guest}\cdots H\text{-}O^{host}$ interaction of CH_4 in MFM-300(In). Distances do not take into account Van der Waals radii; the equivalent distances taking this into account are 4.12 Å and 7.5 Å for the CH_4-water clathrate and MFM-300(In), respectively. Reproduced from Ref 146.

5. Studies of H_2 binding in anionic MOFs with extra-framework cations.

The worldwide research on hydrogen storage in MOFs over the past decade has produced several MOF systems with exceptionally high gravimetric uptake of H_2 with a record of ~16 wt% total uptake capacity observed in NU-100[148] and MOF-200[149] (albeit at high pressure and low temperature, typically 77 K). However, these high uptakes drop dramatically with increasing temperature as a result of the weak binding interaction between H_2 molecules and MOF hosts, and thus no MOF system is able to act as suitable H_2 stores for on-board application to date. Increasing the interaction between H_2 molecules and the host framework, and hence the associated isosteric heat of adsorption, represents a major challenge if these systems are to find practical use at more ambient temperatures.

One particularly promising approach to significantly enhancing the H_2-MOF interaction is to load active alkali and alkaline earth metal centres M (*e.g.*, Li, Na, Mg) into MOF structures and to exploit the potential of strong binding of molecular H_2 at free metal sites. This has been supported by recent computational and theoretical studies on the modelling of H_2 adsorbed into M-doped MOF hosts.[150-156] However, doping of active M(0) into a MOF material is intrinsically problematic by experiment due to the

high reactivity of M(0) with the cationic metal clusters and organic ligands that constitute the MOF structures. Thus, doping with $M^{+/2+}$ ions appears to be a more controllable and feasible route to interrogate and understand H_2 binding in a doped MOF host. Porous anionic MOFs can provide an excellent platform to introduce $M^{+/2+}$ ions within a framework structure *via* balancing the overall charge of the framework.

Zeolite-like MOFs (ZMOFs) are anionic and as such extra framework cations (*i.e.*, $M^{+/2+}$ ions) can readily be introduced. One representative example from this ZMOF family, *rho*-ZMOF, was reported to exhibit facile ion-exchange capability in a similar way as zeolites.[157] The original In(III)-imidazoledicarboxylate *rho*-ZMOF has a formula of $[In_{48}(HImDC)_{96}]^{48-}$ and can incorporate 48 mono-cations or 24 double cations within the cage. Three different cations (dimethylammonium: DMA^+, Li^+, Mg^{2+}) were introduced into the cage to give iso-structural samples of DMA-*rho*-ZMOF, Li-*rho*-ZMOF and Mg-*rho*-ZMOF.[157] The rotational transitions of adsorbed H_2 molecules in these three materials were studied by INS to compare the effect of extra-cation on the H_2 binding.

The adsorption isotherms for H_2 in Li-*rho*-ZMOF and Mg-*rho*-ZMOF below 20 mbar display a steeper rise in uptake than the parent DMA-*rho*-ZMOF, indicating the presence of stronger H_2 binding interactions in the Li/Mg-exchanged MOFs. This has also been supported by calculation of isosteric heats of adsorption of 8.0, 9.1, and 9.0 kJ mol^{-1} for DMA-*rho*-ZMOF, Li-*rho*-ZMOF and Mg-*rho*-ZMOF, respectively. Synchrotron single crystal diffraction on Mg-*rho*-ZMOF has successfully determined the position and coordination of the Mg^{2+} ion which is bound to six water molecules to give a hexaaqua complex $[Mg(OH_2)_6]^{2+}$ which forms hydrogen bonds to carboxylate oxygen centres of the framework (Fig. 46). Unfortunately, TGA data shows that it is not possible to remove the coordinated water molecules on the Mg^{2+} site before the MOF host starts to decompose. The position of Li^+ ion was not located due to the disorder of the cationic site. However, it is reasonable to estimate that Li^+ in Li-*rho*-ZMOF is also fully coordinated to four water molecules to give a tetraaqua complex $[Li(OH_2)_4]^+$ which form hydrogen bonds to the MOF host. Therefore, neither Mg^{2+} nor Li^+ site is directly accessible to the adsorbed H_2 molecules from a crystallographic view.

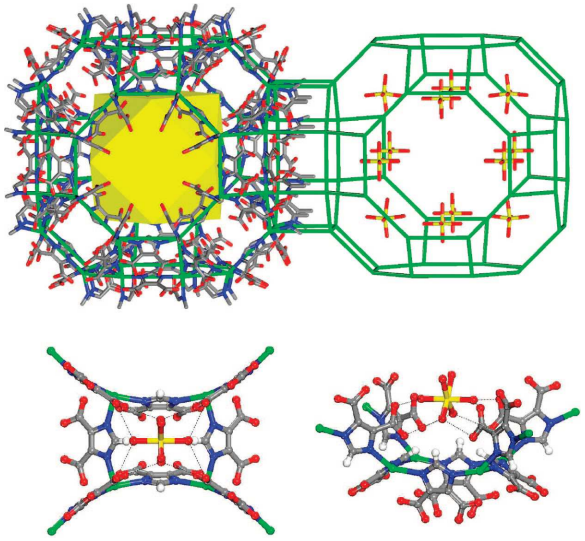

Figure 46. Top: View of the single-crystal structure of Mg-*rho*-ZMOF showing the cubohemioctahedral cages (green) containing 12 $[Mg(OH_2)_6]^{2+}$ cations. All H atoms have been omitted for clarity. Bottom: View of the $[Mg(OH_2)_6]^{2+}$ complex situated near the four-membered rings of each cage, interacting with the MOF through hydrogen bonds (shown as black dotted lines; oxygen to oxygen distance is ~2.9 Å) with four of the aqua ligands. Reproduced from Ref 157.

INS spectra for H_2-loaded DMA-*rho*-ZMOF, Li-*rho*-ZMOF and Mg-*rho*-ZMOF are similar. At low loading, each has four reasonably well-defined binding sites for H_2 with very small energy barrier for H_2 rotation on each site. In comparison to a similar study carried out on Li^+-exchanged zeolite FAU-LiX which presents two strong energy transfer peaks at ~1 and 7.5 meV,[158] Li-*rho*-ZMOF does not show such low energy transfer peaks, indicating the lack of strong binding to the Li^+ site. This is consistent with the formation of $[Li(OH_2)_4]^+$ in the pore with Li^+ cation not directly accessible. A similar conclusion has been drawn for H_2-loaded Mg-*rho*-ZMOF. A direct comparison of the INS spectra for H_2-loaded Li-*rho*-ZMOF and the parent DMA-*rho*-ZMOF shows that in the former there is an additional increase in intensity in the region between ~6 and 10 meV. This can be assigned to be the interaction between H_2 molecules and the Li^+-water complex, though the contribution is not significant. Based upon these results, the relatively small observed enhancement of H_2 adsorption properties most likely originates from the increased electrostatic field in the cavity due to the extra framework cations rather than due to any direct binding interaction between these sites to H_2.

One alternative approach to synthesise anionic MOFs is based upon the linking of tetrahedral nodes derived from In(III) centres bound to isophthalate tetracarboxylates to form 4-connected (4-c) structures. The

discrepancy between the charge on In(III) and the negative organic linker L^{4-} leads to the formation of anionic complexes $[In(L)]^-$ in which the net charge has to be balanced by counter-cation(s). A series of anionic MOFs (MFM-200, 204, 206, 208; MFM = Manchester Framework Material, replacing the NOTT designation) were designed and synthesised *via* this route.[159-162] In the as-synthesised sample, organic cations (DMA^+ or dihydropiperazinium^{2+}) act as the counter cations and partially block the pore entrance owing to their bulky nature. These organic counter-cations within the as-synthesized materials are exchangeable to smaller Li^+ cations while still maintaining the porosity of the framework structure. In this way, a number of corresponding Li^+-loaded iso-structural MOFs (MFM-201,205,207,209) were generated to provide the platform to study the H_2 binding interaction to the framework cation Li^+ sites.[159-162] One of significant improvements of this system is the successful location of the position of Li^+ ion within the channels of MFM-201, 207, and 209.

The H_2 binding interaction in MFM-209 was studied with INS and is discussed here.[159] MFM-209-solv is doubly interpenetrated and has three different types of channels (*A*, *B* and *C*) due to the overlapping of the two networks. The three channels have different sizes and surface chemistry (Fig. 47a,b).[162] X-ray crystallography confirms that the Li^+ cation sits in the smallest channel *C*, tetrahedrally coordinated to four O-centres, two from carboxylate groups and two from coordinated H_2O molecules. Thus, the $[In(O_2CR)_4]$ moiety is able to anchor Li^+ *via* two chelate carboxylate groups, leaving potentially accessible and exposed Li^+ sites after desolvation. Indeed, an *in situ* IR experiment has confirmed the removal of these two coordinated water molecules on Li^+ sites at around 150 °C, giving open Li^+ sites in the activated MOF. This observation is also consistent with the ^{7}Li-NMR experiment which suggests in the desolvated MOF the coordination environment of Li^+ ion has lower symmetry.[162] Desolvated MFM-209 shows an enhancement of H_2 uptake capacity of 31% in comparison to the parent MOF that contains organic counter-cations. This increase in uptake capacity is also accompanied by an increase of 38% in isosteric heat of H_2 adsorption. Significantly, MFM-209 displays a very high heat of adsorption of 12 kJ mol^{-1}, which is higher than most reported MOF materials (4-7 kJ mol^{-1} typically).

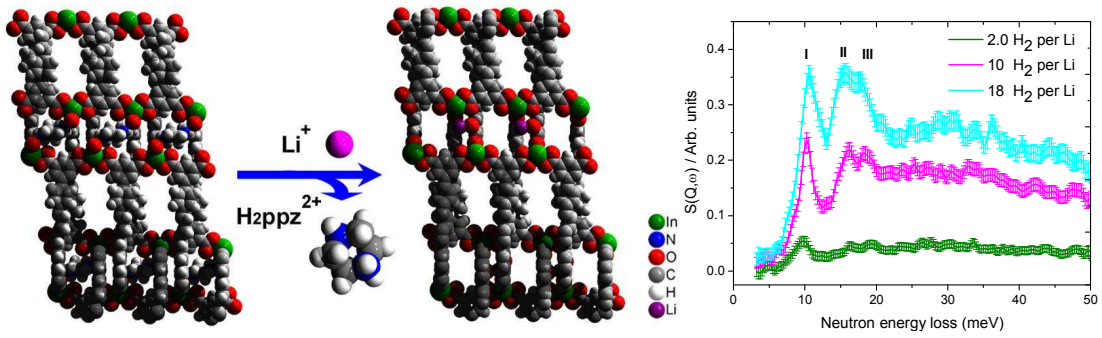

a b c

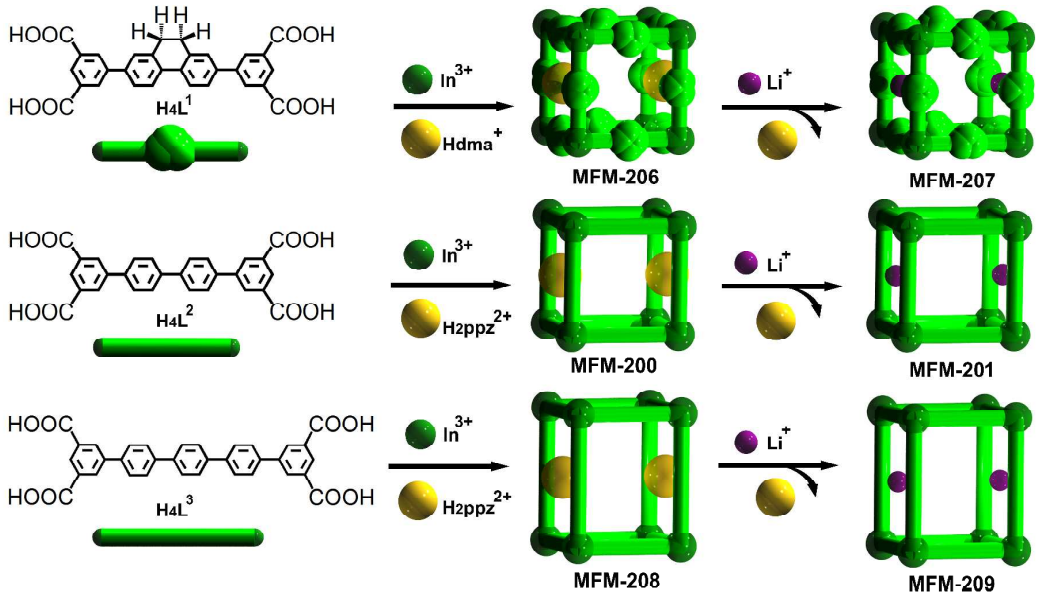

d

Figure 47. Space-filling views of the framework structures of (a) MFM-208 and (b) MFM-209 containing different cations within channels. (c) INS difference spectra for the various H_2/Li loadings in MFM-209. (d) View of the self-assembly and cation-exchange processes within anionic MFM-200, 201, 206, 207, 208 and 209. Reproduced from Refs 159, 162.

To provide insight into the increase of heat of adsorption, INS was used to interrogate the presence of potential binding between adsorbed H_2 and the open Li^+ site in MFM-209.[159] The INS spectra for H_2-loaded MFM-209 show a significant increase in intensity due to the recoil of H_2. The difference INS spectra of H_2-loaded and bare MFM-209 displays three distinct energy transfer peaks at 10, 16 and 19 meV (Fig. 47c). With increasing H_2 loadings, these peaks increase linearly in intensity until saturation indicating that for all loadings, the adsorbed H_2 molecules are interacting with the same sites within the framework of

MFM-209 and these sites do not reach saturation at low pressure. The peaks in the INS spectra correspond to the rotational J = 0 to J = 1 transition of the H_2 molecule, J(1←0). In principle, three lines are present due to the contribution from the initial state (where m = 0) and the final state (where m = 1, 0, +1). The lowest energy transfer peak at 10 meV in the spectra suggests the adsorbed H_2 molecules in MFM-209 interact with $[In(O_2CR)_4]$ centres, rather than via direct binding to open Li^+ sites. This is because, in the latter case, the INS peak will stop increasing when the site reaches saturation for adsorbed H_2 molecules. Thus, the enhancement of the enthalpy of adsorption of H_2 upon loading Li^+ cations must originate from a change in the charge distribution in the $[In(O_2CR)_4]$ moiety by incorporation of Li^+ ions. This deduction is also consistent with the observation that Li^+ doping enhances the adsorption enthalpy at all H_2 loadings, rather than only at low H_2 loadings. The nature of the extra-framework cations introduced from cation-exchange reactions here is not strictly comparable with those of M(0)-doping[150-156] since the latter also involves reduction of the framework host. It, therefore, still remains a practical challenge to introduce more active M(0) sites into MOFs to improve the H_2 binding at more ambient conditions.

6. Trapping of unusual guests and reactive intermediates in porous hosts

In 2002, Fujita *et al.* reported the synthesis of the doubly interpenetrated 3D coordination polymer $[(ZnI_2)_3(TPT)_2]\cdot 6(C_6H_5NO_2)$ [TPT = 2,4,6-tris(4-pyridyl)triazine].[163] Upon removal of the enclathrated solvent molecules under vacuum, a compression of the two nets occurs with the material retaining its crystallinity. This process is not only reversible, but the guest molecules can also be exchanged for a variety of solvents in a single-crystal to single-crystal manner. In the case of benzene, the guest molecules were reported to be ordered in the pores, although no specific interactions with the frameworks could be identified. Large aromatic molecules such as triphenylene (Fig. 48), anthracene and perylene have also been inserted in the pores of $[(ZnI_2)_3(TPT)_2]$ which remains crystalline while the guests are ordered due to π-π interactions with the electron deficient ligand.[164]

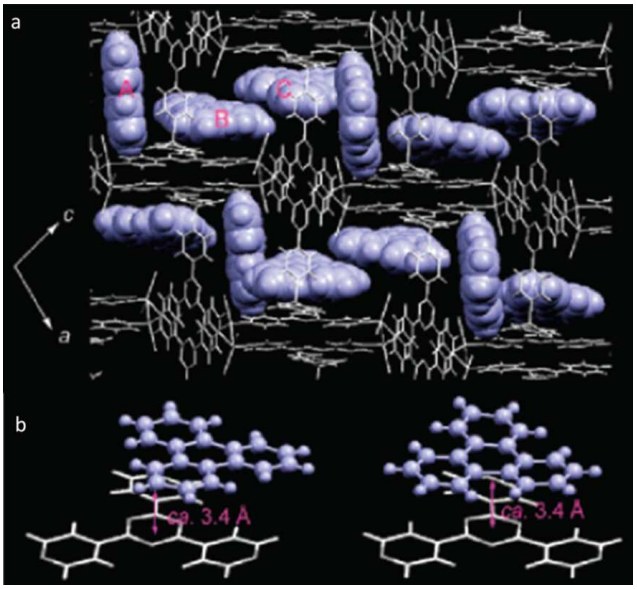

Figure 48. Views of (a) crystal structure of $[(ZnI_2)_3(TPT)_2]$ accommodating triphenylene molecules, and (b) π-π interaction between TPT ligand and triphenylene guest. Reproduced from Ref. 164.

Further investigations on the insertion of functionalized triphenylenes[165] led to the observation, by X-ray crystallography, of a transient hemiaminal in a porous coordination network, a demonstration of the kinetic-trapping of a normally short-lived reaction intermediate.[166] The $[[(ZnI_2)_3(\mathbf{2})_2(\mathbf{3})].x(\mathbf{G})]_n$ network (**2** = TPT = 2,4,6-tris(4-pyridyl)triazine; **3** = 1-aminotriphenylene; **G** = ethyl acetate, x ~ 4) contains two types of pores of different shapes (A and B) with the amino groups of **3** facing directly into type-A pores (Fig. 49). A single crystal of $[[(ZnI_2)_3(\mathbf{2})_2(\mathbf{3})].x(\mathbf{G})]_n$ was cooled to 215 K on a diffractometer and immersed for 10 minutes in a cooled flow of an ethyl acetate solution of acetaldehyde applied *via* a capillary. The crystal was then further cooled to 90 K to stop the reaction and the structure collected to reveal a combination of unreacted amine (64 %) and the transient hemiaminal (36%). Notably, the percentage conversion is consistent with the disordering of the amine over three sites (a-c) in the unreacted crystal (distributed a: 44%, b: 33% and c: 23%), with reaction occurring at only site b. The lack of reaction at a and c sites was attributed to steric hindrance. The hemiaminal intermediate was kinetically trapped at 90 K, but warming to 270 K and standing for 30 minutes led to completion of the condensation reaction. Collecting a final structure at 90 K confirmed complete conversion of the hemiaminal to the imine product.

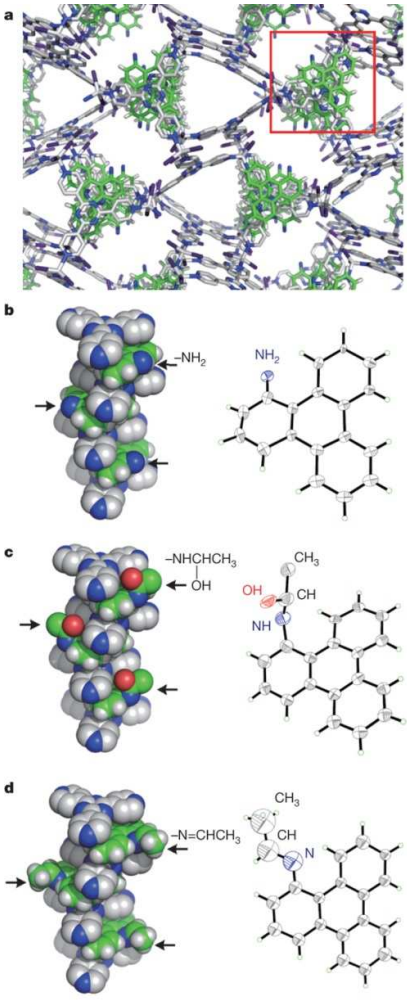

Figure 49. (a) Network structure of **1** (**G** = ethyl acetate, x = 4). In the boxed region, aromatic amine **3** stacks in an alternating donor–acceptor fashion with triazine ligand **2**. The pore is filled with solvent molecules (ethyl acetate), which are omitted for clarity; (b) Left: view of the columnar stack of aromatic amine guest **3** and the triazine ligand; right: thermal-ellipsoid diagram of embedded guest **3**; (c) The transient hemiaminal intermediate formed *in situ* by treating a crystal of **1** with acetaldehyde at 215 K for 10 min. Left: view of the columnar stack of hemiaminal **4** and the triazine ligand **2**; right: embedded hemiaminal **4** (*R**-isomer, 18% occupancy (18% *S**-isomer not shown; *R** and *S** denote relative configurations)); (d) The final product (imine **5**) obtained by warming hemiaminal **4** at 270 K for 30 min. Left: view of the columnar stack of imine **5** and triazine ligand **2**; right: embedded imine **5**. All thermal-ellipsoid diagrams are drawn at 30% probability. Colours: carbon, light grey in **2**, green in **3**, **4** and **5**; nitrogen, blue; oxygen, red; hydrogen, white. Hydrogen atoms of **2** are omitted for clarity. Arrows in **b**, **c** and **d** indicate the positions of $–NH_2$, $–NHCH(OH)CH_3$ and $–N = CHCH_3$ groups, respectively. Reproduced from Ref. 166.

The exchange properties of $[(ZnI_2)_3(TPT)_2]$ are not limited to large, simple aromatic molecules. The strong binding ability of this coordination framework were used to develop a methodology for direct crystallographic characterisation of trace amounts of a large variety of molecules, including absolute configuration of chiral compounds such as santonin (Fig. 50) by loading them in the pores of a single crystal of the coordination polymer.[167-170] While this approach has some significant challenges, both in reproducibility and in substrate scope, a few other examples that exploit the concept have been reported.[171, 172]

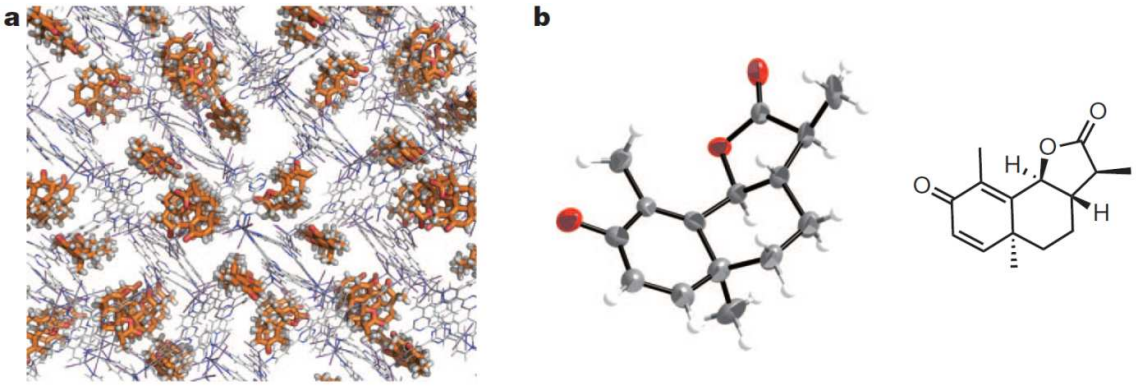

Figure 50. (a) Network structure of the clathrate comprising santonin and $[(ZnI_2)_3(TPT)_2]$; (b) ORTEP drawing (50% probability) of santonin trapped in the pore and chemical structure of santonin. Reproduced from Refs 167.

7. Adsorbate superlattice formation in MOFs revealed by SAXS

The applicability of a laboratory-designed small-angle X-ray scattering (SAXS) set-up for studying the adsorption behavior of guest molecules in the mesoporous IRMOF-74 series has been reported.[173] Specifically, high resolution *in situ* SAXS data on Ar adsorption in IRMOF-74-V-hex enabled the accurate mapping of Ar distribution in the pore structure at different pressures (Fig. 51). The adsorption of Ar was defined by five different adsorption stages during the entire studied pressure range (0–100 kPa). The adsorbate electron-distribution maps from SAXS analysis revealed that Ar interacts with the open metal sites at stages 1 and 2 (low pressure region < 27 kPa). When the pressure was increased to stage 3 (27–33 kPa), Ar molecules start to fill the pores, leading to a steep increase in gas uptake. The corresponding $hk = 10$ reflection intensity decreased sharply during this stage, while a new broad peak at $q = 0.10$ Å^{-1} emerged. The

emergence of this broad peak unambiguously represents the aggregation point in the initiation of formation of extra adsorption domains, whereby adsorbate atoms gather in certain pore regions in higher numbers than the average. As confirmed by the appearance of superlattice reflections in the SAXS patterns, these adsorption domains form the adsorbate superlattice at stage 4 (33–50 kPa). Upon further increases in pressure (stage 5, >50 kPa), the extra adsorption domains and superlattice reflections disappear, and the electron density in the centre region of the pores gradually increases, indicating argon fills among the pores in a uniform manner. This study indicates that adsorbate–adsorbate interactions within and across adjacent pores play a major role in gas uptake and release in porous MOFs.

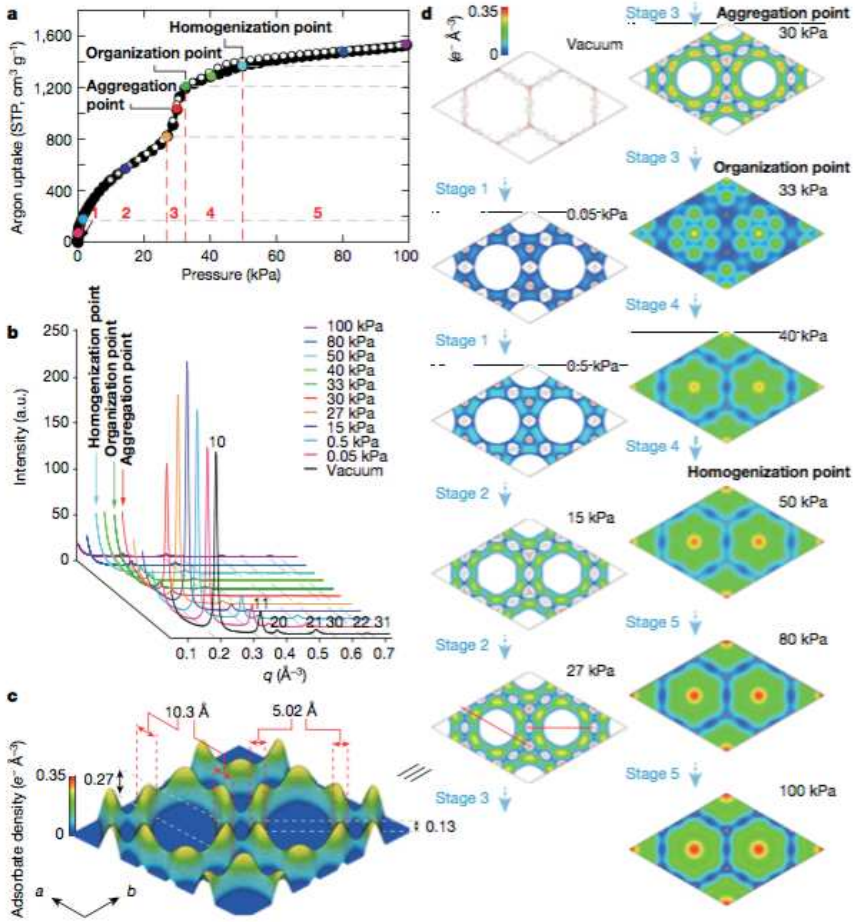

Figure 51. Mapping of the distribution of Ar in IRMOF-74-V-hex. (a) Ar uptake by IRMOF-74-V-hex at different pressures. The isotherm shows five stages (1 to 5), with distinct slopes. Three points (red, dark green and light blue) are highlighted for the start, end/start and end of two events unobserved in type IV isotherms. (b) SAXS scattering profiles measured along the entire adsorption process at 11 different gas pressures, covering the different stages of Ar

adsorption. The patterns are overlaid in linear scale with colours corresponding to the points in the isotherm. (c) Three-dimensional contour map of the electron-density profile of Ar at 27 kPa. The mesopores are covered by Ar at this point. (d) Projected Ar distribution in two dimensions from the three-dimensional contour maps. Each two-dimensional map reveals the distribution of Ar within the MOF structure at a certain pressure. The red lines at 27 kPa indicate the Ar profile projection in two directions (metal site to metal site, and wall to wall). Reproduced from Ref. 173.

8. Conclusions

Significant advances have been made in the field of porous MOFs, particularly in the field of high capacity gas storage and selective recognition, binding and separation of molecular substrates. Understanding the molecular mechanism by which these MOFs bind gas molecules from both crystallographic and dynamic perspectives provides key insight into the design and discovery of materials with improved properties. This article has reviewed recent advances and significant achievements on the successful characterisation of guest-loaded MOF materials *via* synchrotron PXRD, single crystal diffraction, NPD, INS, QENS, SAXS, IR, and NMR techniques. The combination of these experimental approaches, particularly with both diffraction and spectroscopic methods, has yielded important rationalisation of materials property and function in terms of the mechanism of substrate binding at a molecular level. The role of open metal centres and pendant functional groups in the pore of MOFs has been discussed with the former providing specific binding to guest molecules, often with high selectivity. However, materials incorporating such sites usually suffer from stability and reversibility issues, while the binding of guest molecules *via* a combination of moderate-to-weak supramolecular based interactions via ligand functionalization affords less energy penalties with improved materials stability. The studies described herein on the elucidation of binding sites and host-guest interactions with porous MOFs enables and assists the design and optimisation of future “smart materials” in which high adsorption capacity, selectivity and stability may be achieved simultaneously.

9. Acknowledgements

We thank Universities of Manchester and Nottingham, EPSRC and ERC for funding. Our work involving synchrotron and neutron scattering techniques were supported by STFC ISIS facility, Diamond light source, ERSF, ILL, ALS and ORNL. MS acknowledges receipt of a Russian Megagrant from the Russian Ministry of Education and Science.

10. References

1. H. C. Zhou, J. R. Long and O. M. Yaghi, *Chem. Rev.*, 2012, **112**, 673-674.
2. J. R. Long and O. M. Yaghi, *Chem. Soc. Rev.*, 2009, **38**, 1201-1507.
3. P. C. H. Mitchell, S. F. Parker, A. J. Ramirez-Cuesta and J. Tomkinson, *Vibrational spectroscopy with neutrons with applications in chemistry, biology, material sciences and catalysis*, World Scientific, Singapore, 2005.
4. Y. Yan, S. Yang, A. J. Blake and M. Schröder, *Acc. Chem. Res.*, 2014, **47**, 296-307.
5. M. P. Suh, H. J. Park, T. K. Prasad and D.-W. Lim, *Chem. Rev.*, 2012, **112**, 782-835.
6. T. A. Makal, J.-R. Li, W. Lu and H.-C. Zhou, *Chem. Soc. Rev.*, 2012, **41**, 7761-7779.
7. J. A. Mason, M. Veenstra and J. R. Long, *Chem. Sci.*, 2014, **5**, 32-51.
8. J.-R. Li, J. Sculley and H.-C. Zhou, *Chem. Rev.*, 2012, **112**, 869-932.
9. J. Lee, O. K. Farha, J. Roberts, K. A. Scheidt, S. T. Nguyen and J. T. Hupp, *Chem. Soc. Rev.*, 2009, **38**, 1450-1459.
10. S. S. Y. Chui, S. M. F. Lo, J. P. H. Charmant, A. G. Orpen and I. D. Williams, *Science*, 1999, **283**, 1148-1150.
11. V. K. Peterson, C. M. Brown, Y. Liu and C. J. Kepert, *J. Phys. Chem. C*, 2011, **115**, 8851-8857.
12. Y. Liu, C. M. Brown, D. A. Neumann, V. K. Peterson and C. J. Kepert, *J. Alloys Compd.*, 2007, **446−447**, 385-388.
13. X. Lin, N. R. Champness and M. Schröder, in *Functional Metal-Organic Frameworks: Gas Storage, Separation and Catalysis, Topics in Current Chemistry*, ed. M. Schröder, 2010, vol. 293, pp. 35-76.
14. X. Lin, J. Jia, X. Zhao, K. M. Thomas, A. J. Blake, G. S. Walker, N. R. Champness, P. Hubberstey and M. Schröder, *Angew. Chem. Int. Ed.*, 2006, **45**, 7358-7364.
15. Y. Yan, I. Telepeni, S. Yang, X. Lin, W. Kockelmann, A. Dailly, A. J. Blake, W. Lewis, G. S. Walker, D. R. Allan, S. A. Barnett, N. R. Champness and M. Schröder, *J. Am. Chem. Soc.*, 2010, **132**, 4092-4094.
16. Y. Peng, V. Krungleviciute, I. Eryazici, J. T. Hupp, O. K. Farha and T. Yildirim, *J. Am. Chem. Soc.*, 2013, **135**, 11887-11894.
17. H. Wu, J. M. Simmons, Y. Liu, C. M. Brown, X. S. Wang, S. Ma, V. K. Peterson, P. D. Southon, C. J. Kepert, H. C. Zhou, T. Yildirim and W. Zhou, *Chem. -Eur. J.*, 2010, **16**, 5205-5214.
18. S. C. Xiang, W. Zhou, J. M. Gallegos, Y. Liu and B. L. Chen, *J. Am. Chem. Soc.*, 2009, **131**, 12415-12419.
19. D. F. Sava, K. W. Chapman, M. A. Rodriguez, J. A. Greathouse, P. S. Crozier, H. Zhao, P. J. Chupas and T. M. Nenoff, *Chem. Mater.*, 2013, **25**, 2591-2596.
20. L. J. Murray, M. Dincã, J. Yano, S. Chavan, S. Bordiga, C. M. Brown and J. R. Long, *J. Am. Chem. Soc.*, 2010, **132**, 7856-7857.
21. X. Lin, I. Telepeni, A. J. Blake, A. Dailly, C. M. Brown, J. M. Simmons, M. Zoppi, G. S. Walker, K. M. Thomas, T. J. Mays, P. Hubberstey, N. R. Champness and M. Schröder, *J. Am. Chem. Soc.*, 2009, **131**, 2159-2171.
22. J. Kubas Gregory, *Acc. Chem. Res.*, 1988, **21**, 120-128.
23. Y. Yan, A. J. Blake, W. Lewis, S. A. Barnett, A. Dailly, N. R. Champness and M. Schröder, *Chem. -Eur. J.*, 2011, **17**, 11162-11170.
24. Y. Yan, X. Lin, S. Yang, A. J. Blake, A. Dailly, N. R. Champness, P. Hubberstey and M. Schröder, *Chem. Commun.*, 2009, 1025-1027.
25. M. Dincã, W. S. Han, Y. Liu, A. Dailly, C. M. Brown and J. R. Long, *Angew. Chem. Int. Ed.*, 2007, **46**, 1419-1422.
26. M. Dincã, A. Dailly, Y. Liu, C. M. Brown, D. A. Neumann and J. R. Long, *J. Am. Chem. Soc.*, 2006, **128**, 16876-16883.
27. K. Sumida, S. Horike, S. S. Kaye, Z. R. Herm, W. L. Queen, C. M. Brown, F. Grandjean, G. J. Long, A. Dailly and J. R. Long, *Chem. Sci.*, 2010, **1**, 184-191.
28. E. D. Bloch, M. R. Hudson, J. A. Mason, S. Chavan, V. Crocellà, J. D. Howe, K. Lee, A. L. Dzubak, W. L. Queen, J. M. Zadrozny, S. J. Geier, L.-C. Lin, L. Gagliardi, B. Smit, J. B. Neaton, S. Bordiga, C. M. Brown and J. R. Long, *J. Am. Chem. Soc.*, 2014, **136**, 10752-10761.
29. H. Sato, W. Kosaka, R. Matsuda, A. Hori, Y. Hijikata, R. V. Belosludov, S. Sakaki, M. Takata and S. Kitagawa, *Science*, 2014, **343**, 167-170.
30. N. L. Rosi, J. Eckert, M. Eddaoudi, D. T. Vodak, J. Kim, M. O'Keeffe and O. M. Yaghi, *Science*, 2003, **300**, 1127-1129.
31. B. Chen, M. Eddaoudi, S. T. Hyde, M. O'Keeffe and O. M. Yaghi, *Science*, 2001, **291**, 1021-1023.
32. J. L. C. Rowsell, J. Eckert and O. M. Yaghi, *J. Am. Chem. Soc.*, 2005, **127**, 14904-14910.
33. A. R. Millward and O. M. Yaghi, *J. Am. Chem. Soc.*, 2005, **127**, 17998-17999.
34. N. L. Rosi, J. Kim, M. Eddaoudi, B. Chen, M. O'Keeffe and O. M. Yaghi, *J. Am. Chem. Soc.*, 2005, **127**, 1504-1518.
35. P. D. C. Dietzel, Y. Morita, R. Blom and H. Fjellvag, *Angew. Chem. Int. Ed.*, 2005, **44**, 6354-6358.
36. P. D. C. Dietzel, B. Panella, M. Hirscher, R. Blom and H. Fjellvåg, *Chem. Commun.*, 2006, 959-961.
37. L. Valenzano, J. G. Vitillo, S. Chavan, B. Civalleri, F. Bonino, S. Bordiga and C. Lamberti, *Catal. Today*, 2012, **182**, 67-79.

38. F. Bonino, S. Chavan, J. G. Vitillo, E. Groppo, G. Agostini, C. Lamberti, P. D. C. Dietzel, C. Prestipino and S. Bordiga, *Chem. Mater.*, 2008, **20**, 4957-4968.
39. S. P. Nandi and P. L. Walker, *Sep. Sci.*, 1976, **11**, 441-453.
40. E. D. Bloch, L. M. Murray, W. L. Queen, S. Chavan, S. N. Maximoff, J. P. Bigi, R. Krishna, V. K. Peterson, F. Grandjean, G. J. Long, B. Smit, S. Bordiga, C. M. Brown and J. R. Long, *J. Am. Chem. Soc.*, 2011, **133**, 14814-14822.
41. Y. Li and R. T. Yang, *Langmuir*, 2007, **23**, 12937-12944.
42. T. K. Maji, R. Matsuda and S. Kitagawa, *Nat. Mater.*, 2007, **6**, 142-148.
43. J. W. Yoon, S. H. Jhung, Y. K. Hwang, S. M. Humphrey, P. T. Wood and J. S. Chang, *Adv. Mater.*, 2007, **19**, 1830-1834.
44. B. Mu, P. M. Schoenecker and K. S. Walton, *J. Phys. Chem. C*, 2010, **114**, 6464-6471.
45. M. Xue, Z. J. Zhang, S. C. Xiang, Z. Jin, C. D. Liang, G. S. Zhu, S. L. Qiu and B. L. Chen, *J. Mater. Chem.*, 2010, **20**, 3984-3988.
46. Y. S. Bae, A. M. Spokoyny, O. K. Farha, R. Q. Snurr, J. T. Hupp and C. A. Mirkin, *Chem. Commun.*, 2010, **46**, 3478-3480.
47. P. D. Southon, D. J. Price, P. K. Nielsen, C. J. McKenzie and C. J. Kepert, *J. Am. Chem. Soc.*, 2011, **133**, 10885-10891.
48. D. J. Xiao, E. D. Bloch, J. A. Mason, W. L. Queen, M. R. Hudson, N. Planas, J. Borycz, A. L. Dzubak, P. Verma, K. Lee, F. Bonino, V. Crocellà, J. Yano, S. Bordiga, D. G. Truhlar, L. Gagliardi, C. M. Brown and J. R. Long, *Nat. Chem.*, 2014, **6**, 590-595.
49. X.-J. Hou, P. He, H. Li and X. Wang, *J. Phys. Chem. C*, 2013, **117**, 2824-2834.
50. Y. He, R. Krishna and B. Chen, *Energy Environ. Sci.*, 2012, **5**, 9107-9120.
51. H. Bux, C. Chmelik, R. Krishna and J. Caro, *J. Memb. Sci.*, 2011, **369**, 284-289.
52. Y. He, W. Zhou, R. Krishna and B. Chen, *Chem. Commun.*, 2012, **48**, 11813-11831.
53. S. Chavan, F. Bonino, J. G. Vitillo, E. Groppo, C. Lamberti, P. D. C. Dietzel, A. Zecchina and S. Bordiga, *Phys. Chem. Phys. Chem.*, 2009, **11**, 9811-9822.
54. S. M. Chavan, G. C. Shearer, E. Bloch and S. Bordiga, *ChemPhysChem*, 2012, **13**, 445-448.
55. Q. Yang, D. Liu, C. Zhong and J.-R. Li, *Chem. Rev.*, 2013, **113**, 8261-8323.
56. Z. Bao, S. Alnemrat, L. Yu, L. Vasiliev, Q. Ren, X. Lu and S. Deng, *Langmuir*, 2011, **27**, 13554-13562.
57. P. Verma, X. Xu and D. G. Truhlar, *J. Phys. Chem. C*, 2013, **117**, 12648-12660.
58. H. Kim, J. Park and Y. Jung, *Phys. Chem. Chem. Phys.*, 2013, **15**, 19644-19650.
59. E. D. Bloch, W. L. Queen, R. Krishna, J. M. Zadrozny, C. M. Brown and J. R. Long, *Science*, 2012, **335**, 1606-1610.
60. S. J. Geier, J. A. Mason, E. D. Bloch, W. L. Queen, M. R. Hudson, C. M. Brown and J. R. Long, *Chem. Sci.*, 2013, **4**, 2054-2061.
61. Y. S. Bae, K. L. Mulfort, H. Frost, P. Ryan, S. Punnathanam, L. J. Broadbelt, J. T. Hupp and R. Q. Snurr, *Langmuir*, 2008, **24**, 8592-8598.
62. S. A. FitzGerald, C. J. Pierce, J. L. C. Rowsell, E. D. Bloch and J. A. Mason, *J. Am. Chem. Soc.*, 2013, **135**, 9458-9464.
63. J. G. Vitillo, L. Regli, S. Chavan, G. Ricchiardi, G. Spoto, P. D. C. Dietzel, S. Bordiga and A. Zecchina, *J. Am. Chem. Soc.*, 2008, **130**, 8386-8396.
64. C. Otero Areán, S. Chavan, C. P. Cabello, E. Garrone and G. T. Palomino, *ChemPhysChem*, 2010, **11**, 3237-3242.
65. N. Nijem, J. F. Veyan, L. Z. Kong, H. H. Wu, Y. G. Zhao, J. Li, D. C. Langreth and Y. J. Chabal, *J. Am. Chem. Soc.*, 2010, **132**, 14834-14848.
66. S. A. FitzGerald, B. Burkholder, M. Friedman, J. B. Hopkins, C. J. Pierce, J. M. Schloss, B. Thompson and J. L. C. Rowsell, *J. Am. Chem. Soc.*, 2011, **133**, 20310-20318.
67. S. A. FitzGerald, J. Hopkins, B. Burkholder, M. Friedman and J. L. C. Rowsell, *Physical Review B*, 2010, **81**, 104305.
68. E. Garrone and C. Otero Arean, *Chem. Soc. Rev.*, 2005, **34**, 846-857.
69. S. Bordiga, L. Regli, F. Bonino, E. Groppo, C. Lamberti, B. Xiao, P. S. Wheatley, R. E. Morris and A. Zecchina, *Phys. Chem. Chem. Phys.,* 2007, **9**, 2676-2685.
70. N. Nijem, J. F. Veyan, L. Z. Kong, K. H. Li, S. Pramanik, Y. G. Zhao, J. Li, D. Langreth and Y. J. Chabal, *J. Am. Chem. Soc.*, 2010, **132**, 1654-1664.
71. Y. Liu, H. Kabbour, C. M. Brown, D. A. Neumann and C. C. Ahn, *Langmuir*, 2008, **24**, 4772-4777.
72. J. L. C. Rowsell and O. M. Yaghi, *J. Am. Chem. Soc.*, 2006, **128**, 1304-1315.
73. S. M. Chavan, O. Zavorotynska, C. Lamberti and S. Bordiga, *Dalton Trans.*, 2013, **42**, 12586-12595.
74. W. L. Queen, E. D. Bloch, C. M. Brown, M. R. Hudson, J. A. Mason, L. J. Murray, A. J. Ramirez-Cuesta, V. K. Peterson and J. R. Long, *Dalton Trans.*, 2012, **41**, 4180-4187.
75. K. Sumida, C. M. Brown, Z. R. Herm, S. Chavan, S. Bordiga and J. R. Long, *Chem. Commun.*, 2011, **47**, 1157-1159.
76. F. Salles, D. I. Kolokolov, H. Jobic, G. Maurin, P. L. Llewellyn, T. Devic, C. Serre and G. Férey, *J. Phys. Chem. C*, 2009, **113**, 7802-7812.

77. M. T. Kapelewski, S. J. Geier, M. R. Hudson, D. Stück, J. A. Mason, J. N. Nelson, D. J. Xiao, Z. Hulvey, E. Gilmour, S. A. FitzGerald, M. Head-Gordon, C. M. Brown and J. R. Long, *J. Am. Chem. Soc.*, 2014, **136**, 12119-12129.
78. S. R. Caskey, A. G. Wong-Foy and A. J. Matzger, *J. Am. Chem. Soc.*, 2008, **130**, 10870-10871.
79. S. Chavan, J. G. Vitillo, E. Groppo, F. Bonino, C. Lamberti, P. D. C. Dietzel and S. Bordiga, *J. Phys. Chem. C*, 2009, **113**, 3292-3299.
80. P. Canepa, N. Nijem, Y. J. Chabal and T. Thonhauser, *Phys. Rev. Lett.*, 2013, **110**, 026102.
81. L. Valenzano, B. Civalleri, S. Chavan, G. T. Palomino, C. O. Arean and S. Bordiga, *J. Phys. Chem. C*, 2010, **114**, 11185-11191.
82. H. Wu, J. M. Simmons, G. Srinivas, W. Zhou and T. Yildirim, *J. Phys. Chem. Lett.*, 2010, **1**, 1946-1951.
83. P. Canepa, C. A. Arter, E. M. Conwill, D. H. Johnson, B. A. Shoemaker, K. Z. Soliman and T. Thonhauser, *J. Mat. Chem. A*, 2013, **1**, 13597-13604.
84. L. Valenzano, B. Civalleri, K. Sillar and J. Sauer, *J. Phys. Chem. C*, 2011, **115**, 21777-21784.
85. K. Sillar and J. Sauer, *J. Am. Chem. Soc.*, 2012, **134**, 18354-18365.
86. D. Yu, A. O. Yazaydin, J. R. Lane, P. D. C. Dietzel and R. Q. Snurr, *Chem. Sci.*, 2013, **4**, 3544-3556.
87. W. L. Queen, C. M. Brown, D. K. Britt, P. Zajdel, M. R. Hudson and O. M. Yaghi, *J. Phys. Chem. C*, 2011, **115**, 24915-24919.
88. H. Wu, W. Zhou and T. Yildirim, *J. Am. Chem. Soc.*, 2009, **131**, 4995-5000.
89. M. G. Lopez, P. Canepa and T. Thonhauser, *J. Chem. Phys.*, 2013, **138**, 154704.
90. X. Kong, E. Scott, W. Ding, J. A. Mason, J. R. Long and J. A. Reimer, *J. Am. Chem. Soc.*, 2012, **134**, 14341-14344.
91. L.-C. Lin, J. Kim, X. Kong, E. Scott, T. M. McDonald, J. R. Long, J. A. Reimer and B. Smit, *Angew. Chem. Int. Ed.*, 2013, **52**, 4410-4413.
92. J. Xu, V. V. Terskikh and Y. N. Huang, *J. Phys. Chem. Letts.*, 2013, **4**, 7-11.
93. D. Britt, H. Furukawa, B. Wang, T. G. Glover and O. M. Yaghi, *Proc. Natl. Acad. Sci. U. S. A.*, 2009, **106**, 20637-20640.
94. J. Liu, Y. Wang, A. I. Benin, P. Jakubczak, R. R. Willis and M. D. LeVan, *Langmuir*, 2010, **26**, 14301.
95. J. A. Mason, K. Sumida, Z. R. Herm, R. Krishna and J. R. Long, *Energy Environ. Sci.*, 2011, **4**, 3030.
96. D.-A. Yang, H.-Y. Cho, J. Kim, S.-T. Yang and W.-S. Ahn, *Energy Environ. Sci.*, 2012, **5**, 6465-6473.
97. T. M. McDonald, W. R. Lee, J. A. Mason, B. M. Wiers, C. S. Hong and J. R. Long, *J. Am. Chem. Soc.*, 2012, **134**, 7056-7065.
98. H.-Y. Cho, D.-A. Yang, J. Kim, S.-Y. Jeong and W.-S. Ahn, *Catal. Today*, 2012, **185**, 35-40.
99. E. J. García, J. P. S. Mowat, P. A. Wright, J. Pérez-Pellitero, C. Jallut and G. D. Pirngruber, *The Journal of Physical Chemistry C*, 2012, **116**, 26636-26648.
100. Z. R. Herm, R. Krishna and J. R. Long, *Microporous Mesoporous Mater.*, 2012, **151**, 481.
101. T. Remy, S. A. Peter, S. Van der Perre, P. Valvekens, D. E. De Vos, G. V. Baron and J. F. M. Denayer, *J. Phys. Chem. C*, 2013, **117**, 9301-9310.
102. K. Sumida, D. L. Rogow, J. A. Mason, T. M. McDonald, E. D. Bloch, Z. R. Herm, T.-H. Bae and J. R. Long, *Chem. Rev.*, 2012, **112**, 724-781.
103. P. D. C. Dietzel, R. E. Johnsen, H. Fjellvåg, S. Bordiga, E. Groppo, S. Chavan and R. Blom, *Chem. Commun.*, 2008, 5125.
104. D. Frenkel and B. Smit, *Understanding Molecular Simulation*, 2002.
105. J. A. Mason, K. Sumida, Z. R. Herm, R. Krishna and J. Long, *Energy Environ. Sci.*, 2011, **4**, 3030.
106. K. B. Lee and S. Sircar, *AlChE J.*, 2008, **54**, 2293-2302.
107. E. J. Granite and H. W. Pennline, *Ind. Eng. Chem. Res.*, 2002, **41**, 5470-5476.
108. T. M. McDonald, D. M. D'Alessandro, R. Krishna and J. R. Long, *Chem. Sci.*, 2011, **2**, 2022.
109. T. M. McDonald, J. A. Mason, X. Kong, E. D. Bloch, D. Gygi, A. Dani, V. Crocella, F. Giordanino, S. O. Odoh, W. S. Drisdell, B. Vlaisavljevich, A. L. Dzubak, R. Poloni, S. K. Schnell, N. Planas, K. Lee, T. Pascal, L. F. Wan, D. Prendergast, J. B. Neaton, B. Smit, J. B. Kortright, L. Gagliardi, S. Bordiga, J. A. Reimer and J. R. Long, *Nature*, 2015, **519**, 303-308.
110. C. Serre, F. Millange, C. Thouvenot, M. Nogues, G. Marsolier, D. Louer and G. Férey, *J. Am. Chem. Soc.*, 2002, **124**, 13519-13526.
111. T. Loiseau, C. Serre, C. Huguenard, G. Fink, F. Taulelle, M. Henry, T. Bataille and G. Férey, *Chem. Eur. J.*, 2004, **10**, 1373-1382.
112. F. Millange, N. Guillou, R. I. Walton, J.-M. Greneche, I. Margiolaki and G. Férey, *Chem. Commun.*, 2008, 4732-4734.
113. L. Chen, J. P. S. Mowat, D. Fairen-Jimenez, C. A. Morrison, S. P. Thompson, P. A. Wright and T. Düren, *J. Am. Chem. Soc.*, 2013, **135**, 15763-15773.
114. K. Barthelet, J. Marrot, D. Riou and G. Férey, *Angew. Chem., Int. Ed.*, 2002, **41**, 281.
115. S. Bourrelly, P. L. Llewellyn, C. Serre, F. Millange, T. Loiseau and G. Férey, *J. Am. Chem. Soc.*, 2005, **127**, 13519-13521.
116. C. Serre, S. Bourrelly, A. Vimont, N. A. Ramsahye, G. Maurin, P. L. Llewellyn, M. Daturi, Y. Filinchuk, O. Leynaud, P. Barnes and G. Férey, *Adv. Mater.*, 2007, **19**, 2246-2251.

117. F. Salles, H. Jobic, A. Ghoufi, P. L. Llewellyn, C. Serre, S. Bourrelly, G. Férey and G. Maurin, *Angew. Chem. Int. Ed.*, 2009, **48**, 8335-8339.
118. F. Salles, H. Jobic, T. Devic, P. L. Llewellyn, C. Serre, G. Férey and G. Maurin, *ACS Nano*, 2010, **4**, 143.
119. N. Rosenbach, H. Jobic, A. Ghoufi, F. Salles, G. Maurin, S. Bourrelly, P. L. Llewellyn, T. Devic, C. Serre and G. Férey, *Angew. Chem., Int. Ed.*, 2008, **47**, 6611.
120. F. Salles, H. Jobic, T. Devic, V. Guillerm, C. Serre, M. M. Koza, G. Férey and G. Maurin, *J. Phys. Chem. C*, 2013, **117**, 11275-11284.
121. F. M. Mulder, B. Assfour, J. Huot, T. J. Dingemans, M. Wagemaker and A. J. Ramirez-Cuesta, *J. Phys. Chem. C*, 2010, **114**, 10648-10655.
122. H. Li, M. Eddaoudi, M. O'Keeffe and O. M. Yaghi, *Nature*, 1999, **402**, 276-279.
123. J. L. C. Rowsell, E. C. Spencer, J. Eckert, J. A. K. Howard and O. M. Yaghi, *Science*, 2005, **309**, 1350-1354.
124. E. C. Spencer, J. A. K. Howard, G. J. McIntyre, J. L. C. Rowsell and O. M. Yaghi, *Chem. Commun.*, 2006, 278-280.
125. R. Banerjee, A. Phan, B. Wang, C. Knobler, H. Furukawa, M. O'Keeffe and O. M. Yaghi, *Science*, 2008, **319**, 939-943.
126. A. Phan, C. J. Doonan, F. J. Uribe-Romo, C. B. Knobler, M. O'Keeffe and O. M. Yaghi, *Acc. Chem. Res.*, 2010, **43**, 58.
127. D. Peralta, G. Chaplais, A. Simon-Masseron, K. Barthelet, C. Chizallet, A.-A. Quoineaud and G. D. Pirngruber, *J. Am. Chem. Soc.*, 2012, **134**, 8115-8126.
128. C.-H. Kuo, Y. Tang, L.-Y. Chou, B. T. Sneed, C. N. Brodsky, Z. Zhao and C.-K. Tsung, *J. Am. Chem. Soc.*, 2012, **134**, 14345-14348.
129. K. S. Park, Z. Ni, A. P. Côté, J. Y. Choi, R. D. Huang, F. J. Uribe-Romo, H. K. Chae, M. O'Keeffe and O. M. Yaghi, *Proc. Natl. Acad. Sci. U. S. A.*, 2006, **103**, 10186-10191.
130. H. Wu, W. Zhou and T. Yildirim, *J. Am. Chem. Soc.*, 2007, **129**, 5314-5315.
131. R. Vaidhyanathan, S. S. Iremonger, G. K. H. Shimizu, P. G. Boyd, S. Alavi and T. K. Woo, *Science*, 2010, **330**, 650-653.
132. R. Vaidhyanathan, S. S. Iremonger, K. W. Dawson and G. K. H. Shimizu, *Chem. Commun.*, 2009, 5230-5232.
133. R. Vaidhyanathan, S. S. Iremonger, G. K. H. Shimizu, P. G. Boyd, S. Alavi and T. K. Woo, *Angew. Chem., Int. Ed.*, 2012, **51**, 1826.
134. C. Villiers, J. P. Dognon, R. Pollet, P. Thuery and M. Ephritikhine, *Angew. Chem. Int. Ed.*, **49**, 3465-3468.
135. G. T. Rochelle, *Science*, 2009, **325**, 1652-1654.
136. S. Yang, J. Sun, A. J. Ramirez-Cuesta, S. K. Callear, W. I. F. David, D. P. Anderson, R. Newby, A. J. Blake, J. E. Parker, C. C. Tang and M. Schröder, *Nat. Chem.*, 2012, **4**, 887-894. See also: M. Savage, Y. Cheng, T.L. Easun, J.E. Eyley, S.P. Argent, M.R. Warren, W. Lewis, C. Murray, C.C. Tang, M.D. Frogley, G. Cinque, J. Sun, S. Rudić, R.T. Murden, M.J. Benham, A.N. Fitch, A.J. Blake, A.J. Ramirez-Cuesta, S.Yang and M. Schröder, *Adv. Materials*, 2016, in press.
137. J. R. Long and O. M. Yaghi, *Chem. Soc. Rev.*, 2009, **38**, 1213.
138. S. Yang, A. J. Ramirez-Cuesta and M. Schröder, *Chem. Phys.*, 2014, **428**, 111-116.
139. S. Yang, A. J. Ramirez-Cuesta, R. Newby, V. Garcia-Sakai, P. Manuel, S. K. Callear, S. I. Campbell, C. C. Tang and M. Schröder, *Nat Chem*, 2015, **7**, 121-129.
140. A. L. Myers and J. M. Prausnitz, *AlChE J.*, 1965, **11**, 121-127.
141. S.-C. Xiang, Z. Zhang, C.-G. Zhao, K. Hong, X. Zhao, D.-R. Ding, M.-H. Xie, C.-D. Wu, M. C. Das, R. Gill, K. M. Thomas and B. Chen, *Nat. Comm.*, 2011, **2**.
142. S. J. Geier, J. A. Mason, E. D. Bloch, W. L. Queen, M. R. Hudson, C. M. Brown and J. R. Long, *Chem. Sci.*, 2013, **4**, 2054-2061.
143. B. Li, Y. Zhang, R. Krishna, K. Yao, Y. Han, Z. Wu, D. Ma, Z. Shi, T. Pham, B. Space, J. Liu, P. K. Thallapally, J. Liu, M. Chrzanowski and S. Ma, *J. Am. Chem. Soc.*, 2014, **136**, 8654-8660.
144. Y.-S. Bae, C. Y. Lee, K. C. Kim, O. K. Farha, P. Nickias, J. T. Hupp, S. T. Nguyen and R. Q. Snurr, *Angew. Chem. Int. Ed.*, 2012, **51**, 1857-1860.
145. C. P. Krap, R. Newby, A. Dhakshinamoorthy, H. García, I. Cebula, T. L. Easun, M. Savage, J. E. Eyley, S. Gao, A. J. Blake, W. Lewis, P. H. Beton, M. R. Warren, D. R. Allan, M. D. Frogley, C. C. Tang, G. Cinque, S. Yang and M. Schröder, *Inorg. Chem.*, 2016, **55**, 1076-1088.
146. M. Savage, I. da Silva, M. Johnson, J. H. Carter, R. Newby, M. Suyetin, E. Besley, P. Manuel, S. Rudić, A. N. Fitch, C. Murray, W. I. F. David, S. Yang and M. Schröder, *J. Am. Chem. Soc.*, 2016, **138**, 9119-9127;
147. M. T. Kirchner, R. Boese, W. E. Billups and L. R. Norman, *J. Am. Chem. Soc.*, 2004, **126**, 9407-9412.
148. O. K. Farha, A. O. Yazaydin, I. Eryazici, C. D. Malliakas, B. G. Hauser, M. G. Kanatzidis, S. T. Nguyen, R. Q. Snurr and J. T. Hupp, *Nat. Chem.*, 2010, **2**, 944-948.
149. H. Furukawa, N. Ko, Y. B. Go, N. Aratani, S. B. Choi, E. Choi, A. ö. Yazaydin, R. Q. Snurr, M. O'Keeffe, J. Kim and O. M. Yaghi, *Science*, 2010, **329**, 424-428.
150. A. Blomqvist, C. M. Araujo, P. Srepusharawoot and R. Ahuja, *Proc. Natl. Acad. Sci. U. S. A.*, 2007, **104**, 20173-20176.
151. S. S. Han and W. A. Goddard, *J. Phys. Chem. C*, 2008, **112**, 13431-13436.
152. E. Klontzas, A. Mavrandonakis, E. Tylianakis and G. E. Froudakis, *Nano Lett.*, 2008, **8**, 1572-1576.

153. A. Mavrandonakis, E. Tylianakis, A. K. Stubos and G. E. Froudakis, *J. Phys. Chem. C*, 2008, **112**, 7290-7294.
154. P. Dalach, H. Frost, R. Q. Snurr and D. E. Ellis, *J. Phys. Chem. C*, 2008, **112**, 9278-9284.
155. Y.-S. Bae and R. Q. Snurr, *Microporous Mesoporous Mater.*, 2010, **135**, 178-186.
156. D. Cao, J. Lan, W. Wang and B. Smit, *Angew. Chem. Int. Ed.*, 2009, **48**, 4730-4733.
157. F. Nouar, J. Eckert, J. F. Eubank, P. Forster and M. Eddaoudi, *J. Am. Chem. Soc.*, 2009, **131**, 2864-2870.
158. R. C. Lochan and M. Head-Gordon, *PCCP*, 2006, **8**, 1357-1370.
159. S. Yang, S. K. Callear, A. J. Ramirez-Cuesta, W. I. F. David, J. Sun, A. J. Blake, N. R. Champness and M. Schröder, *Faraday Discuss.*, 2011, **151**, 19-36.
160. S. Yang, X. Lin, A. J. Blake, K. M. Thomas, P. Hubberstey, N. R. Champness and M. Schröder, *Chem. Commun.*, 2008, 6108-6110.
161. S. Yang, X. Lin, A. J. Blake, G. S. Walker, P. Hubberstey, N. R. Champness and M. Schröder, *Nat. Chem.*, 2009, **1**, 487-493.
162. S. Yang, G. S. B. Martin, J. J. Titman, A. J. Blake, D. R. Allan, N. R. Champness and M. Schröder, *Inorg. Chem.*, 2011, **50**, 9374-9384.
163. K. Biradha and M. Fujita, *Angew. Chem. Int. Ed.*, 2002, **41**, 3392-3395.
164. O. Ohmori, M. Kawano and M. Fujita, *J. Am. Chem. Soc.*, 2004, **126**, 16292-16293.
165. M. Kawano, T. Kawamichi, T. Haneda, T. Kojima and M. Fujita, *J. Am. Chem. Soc.*, 2007, **129**, 15418-15419.
166. T. Kawamichi, T. Haneda, M. Kawano and M. Fujita, *Nature*, 2009, **461**, 633.
167. Y. Inokuma, S. Yoshioka, J. Ariyoshi, T. Arai, Y. Hitora, K. Takada, S. Matsunaga, K. Rissanen and M. Fujita, *Nature*, 2013, **495**, 461-466.
168. Y. Inokuma, S. Yoshioka, J. Ariyoshi, T. Arai, Y. Hitora, K. Takada, S. Matsunaga, K. Rissanen and M. Fujita, *Nature*, 2013, **501**, 262-262.
169. Y. Inokuma, S. Yoshioka, J. Ariyoshi, T. Arai and M. Fujita, *Nat. Protocols*, 2014, **9**, 246-252.
170. S. Yoshioka, Y. Inokuma, M. Hoshino, T. Sato and M. Fujita, *Chem. Sci.*, 2015, **6**, 3765-3768.
171. K. Ikemoto, Y. Inokuma, K. Rissanen and M. Fujita, *J. Am. Chem. Soc.*, 2014, **136**, 6892-6895.
172. E. V. Vinogradova, P. Müller and S. L. Buchwald, *Angew. Chem. Int. Ed.*, 2014, **53**, 3125-3128.
173. H. S. Cho, H. Deng, K. Miyasaka, Z. Dong, M. Cho, A. V. Neimark, J. Ku Kang, O. M. Yaghi and O. Terasaki, *Nature*, 2015, **527**, 503-507.